MAGNETIZED BINARY STAR FORMATION

Bo Zhao
Shanxi, China

B.S., Zhejiang University, 2008

M.S., University of Virginia, 2010

A Dissertation Presented to the Graduate
Faculty of the University of Virginia
in Candidacy for the Degree of
Doctor of Philosophy

Department of Astronomy

University of Virginia

August 2014

Zhi-Yun Li

Roger A. Chevalier

Phil Arras

Stefan Baessler

Abstract

The majority of stars reside in multiple systems, especially binaries. The formation and early evolution of binaries is a longstanding problem in star formation that is not yet fully understood. In particular, how the magnetic field observed in the star-forming cores of molecular clouds shapes the binary characteristics remains relatively unexplored. In this thesis, we present a systematic study of magnetized binary formation using the Enzo magnetohydrodynamics code. We investigate separately the initial core fragmentation leading to the formation of two binary seeds, and the binary orbital evolution during the subsequent protostellar mass accretion phase. The famous "magnetic flux problem" in star formation is also studied numerically in detail.

Star-forming dense cores are observed to be significantly magnetized. If the magnetic flux threading the cores is dragged into the stars, the stellar field would be orders of magnitude stronger than observed; most of the core magnetic flux must be decoupled from the matter that enters the star. In our simulations, we find that the accumulation of the decoupled flux near the accreting protostar leads to a magnetic pressure buildup. The high pressure is released anisotropically along the path of least resistance. It drives a low-density expanding region in which the decoupled magnetic flux is expelled. In the presence of an initial core rotation, the structure presents an obstacle to the formation of a rotationally supported disk, in addition to magnetic braking, by acting as a rigid magnetic wall that prevents the rotating gas from completing a full orbit around the central object.

In the study of the magnetized binary formation during the protostellar mass accretion phase, we demonstrate numerically that a magnetic field of the observed strength can drastically change two of the basic quantities that characterize a binary system: the orbital separation and mass ratio of the two components. We find that

in dense cores magnetized to a realistic level, the angular momentum of the material accreted by the protobinary is greatly reduced by magnetic braking. Accretion of strongly braked material shrinks the protobinary separation by a large factor compared to the non-magnetic case. The magnetic braking also changes the evolution of the mass ratio of unequal-mass protobinaries by producing material of low specific angular momentum that accretes preferentially onto the more massive primary star rather than the secondary. In addition, the magnetic field greatly modifies the morphology and dynamics of the protobinary accretion flow.

We also investigate the effects of the misalignment between the magnetic field and rotation axis on the properties of the protobinaries; such a misalignment was recently revealed by millimeter interferometric observations of protostellar systems. Somewhat surprisingly, we find that the misaligned magnetic field is more efficient at tightening the binary orbit compared to the aligned field. The main reason is that the misalignment weakens the magnetically-driven outflow, which allows more material to accrete onto the binary. The additional mass being accreted onto the binary carries insufficient specific angular momentum, which leads to an even tighter binary. A large field-rotation misalignment also helps produce rotationally-supported circumbinary disks even for relatively strong magnetic fields, by weakening the magnetically-dominated structure close to the binary that is responsible for strong magnetic braking in the aligned case.

Finally, we present preliminary results on simulations that follow both the (magnetized) core fragmentation into binary seeds and the subsequent protobinary evolution during the mass accretion phase. We find that fragmentation can occur in a strongly magnetized core as long as the initial density perturbation is large. The resulting binary seeds generally have a large separation and eccentricity. After the first close

approach, the binary can either merge or dynamically relax to a stable orbit depending on the magnetic field strength and orientation. Additional simulations and more detailed analysis are needed to obtain a complete picture of how binary systems form and evolve in magnetized clouds.

Acknowledgments

Foremost, I would like to express my sincere gratitude to my advisor Zhi-Yun Li for his support and supervision over the past six years. He guides me through the hall of science with extraordinary insight, enthusiasm and patience. He tolerates my wild ideas yet presents me a path paved with logic and fairness. He not only taught me how to be a good scientist, but also a good man. In my most difficult times, it is always Li who gives me encouragement, motivation, and hope. Without him, the research presented in this thesis would not be possible.

I would also thank other members of my thesis committee, Roger Chevalier, Phil Arras, and Stefan Baessler, for their inspiring discussion and invaluable advice, especially Roger who has supported me throughout our project on Gamma-Ray-Bursts. Though the work is not included in this thesis, the guidance and training on research I received from Roger are immeasurable. Again, I thank Phil for his generous help on the analysis of my simulations; his intuition and insight in theory has set an example for my future career.

My special thank goes to Peng Wang, who introduced the Enzo code to me and helped me to run the first simulation in my life. His continuous assistance on code compiling and debugging have made the calculations in this theis possible. Besides, I would like to thank my collaborator Kaitlin Kratter for sharing her insight with me. I have benefited enormously from the discussion with Kaitlin, as well as other astronomers including Fumitaka Nakamura, Ruben Krasnopolsky, Hsien Shang, Anaelle Maury, Stella Offner, and Christopher Matzner. I greatly appreciate all their help and advice.

I also want to thank other professors who have taught me astronomy courses in my first two years, they are Mark Whittle, Craig Sarazin, Steve Majewski, Jim Condon, Scott Ransom, Aaron Evans, and Remy Indebetouw. It is them who lead me step by step into the fields of astronomy. In addition, I owe my gratitude to all my colleagues

in the Astronomy department, especially Bin Chen and Guillermo Damke, who have helped me through my way from a physics student to a qualified astronomy graduate.

Finally, I bow my sincere thanks to my parents who have given their full support to my scientific career. It is indeed a hard thing for many Chinese parents who are likely to turn their children to more practical matters. I would not have gone this far in astronomy without the liberal view of my parents. I wish them happy and healthy.

Contents

List of Figures

List of Tables

Chapter 1

Introduction

The last two decades have seen giant leaps in our understanding of star formation owing to the advances in both instrumentation and computing technology. With increasing resolution, recent observations of the earliest phase of star formation have revealed a large fraction of binary and multiple systems among young protostars. With the full ALMA coming online in the near future, the pace of discovery will accelerate. The available results indicate that most stars are born in binary and multiple systems. Multiplicity may well be the dominant outcome of the star formation process.

Given its undisputed importance, how binary and multiple systems form and evolve has long been a topic of theoretical study in star formation. The general accepted mechanism for binary and multiple formation is through collapse and fragmentation of molecular cloud cores (Boss & Bodenheimer 1979). It has been studied extensively through numerical simulations, using both SPH (Smoothed-Particle-Hydrodynamics) and grid-based code. Such studies are starting to include radiative transfer and magnetic fields, leading to increasingly realistic three-dimensional (3D) models of the formation of binary and multiple systems. In this thesis, I will mainly focus on the effects of magnetic field on the formation and subsequent evolution of the simplest stellar systems - binary stars, with an emphasis on the orbital properties of the youngest binaries.

1.1 Observations of Multiplicity

The existence of binary and multiple systems was revealed soon after the birth of modern astronomy in the seventeenth century. Two centuries later, Kuiper (1953) first recognized the importance of multiplicity measurements for main-sequence (MS) stars. After the discovery of young binary companions in some T Tauri stars (Joy & van Biesbroeck 1944; Herbig 1962; Dyck et al. 1982), attention was drawn to the multiple stellar systems in pre-main sequence (PMS) objects (Zinnecker 1984), as a new

probe of the physical processes in the early phase of star formation. In recent years, more advanced technologies such as long-baseline interferometer, adaptive optics and chronograph have brought stellar companions into better focus. The capability of large surveys further refined the statistical properties of binary and multiple systems in both the Galactic field and nearby star forming regions.

Before discussing the observational results, we first clarify the definitions and terminologies in the existing literature. According to Batten (1973), the fractions of systems containing exactly n stars are denoted as f_n . The multiplicity frequency or multiplicity fraction $MF = 1 - f_1 = f_2 + f_3 + f_4 + ...$, gives the fraction of non-single systems in a given sample. This is more commonly written as

$$MF = \frac{B + T + Q}{S + B + T + Q} \tag{1.1}$$

where S,B,T,Q are the number of single, binary, triple, and quadruple, etc systems(Reipurth & Zinnecker 1993). Another common characteristic of multiplicity, the companion star fraction $CSF = f_2 + 2f_3 + 3f_4 + ...$ quantifies the average number of stellar companions per system; it is commonly written as,

$$CSF = \frac{B + 2T + 3Q}{S + B + T + Q} \tag{1.2}$$

which in principle can be greater than 1 (e.g. Ghez et al. 1997). Finally, the fraction of higher-order multiples is simply $HF = 1 - f_1 - f_2 = f_3 + f_4 + ...$

The pioneering multiplicity survey of solar-type stars conducted by Duquennoy & Mayor (1991) (hereafter DM91) is a key reference for the binary and multiple statistics in Galactic field for two decades. DM91 studied 164 objects out to 22 pc by collating results from many separate studies and obtaining their own new radial velocity measurements. However, significant incompleteness potentially affected the conclusions of DM91, which motivates Raghavan et al. (2010) to improve the study with sample of 454 F6-K3 stars out to 25 pc, using many improved observational

methods. Their observed fractions of single, binary, triple and quadruple stars are $56\pm 2\% : 33\pm 2\% : 8\pm 2\% : 3\pm 1\%$, yielding a completion-corrected multiplicity frequency of 46%, and implying that among solar type stars, the majority are single. However, the multiplicity does have a dependence on stellar mass. Specifically, super-solar dwarfs have a marginally higher multiplicity rate than sub-solar dwarfs: $MF^{MS}_{1-1.3\,\mathrm{M}_\odot} = 50 \pm 4\%$ versus $MF^{MS}_{0.7-1\,\mathrm{M}_\odot} = 41 \pm 3\%$. Similarly, $CSF^{MS}_{1-1.3\,\mathrm{M}_\odot} = 75 \pm 5\%$ and $CSF^{MS}_{0.7-1\,\mathrm{M}_\odot} = 56 \pm 4\%$. Nonetheless, almost half of the sun-like low-mass stars reside in multiple systems in the nearby Galactic field, which raises the interesting question of how the multiple systems form, and whether today's single stars, including our Sun, are born alone or as the product of dynamical evolution of multiple systems.

Over the past decades, increasing efforts have been devoted to the study of binaries and multiples during the early protostellar phase of star formation, in an attempt to answer the above questions. However, most protostars are still deeply embedded in their nascent cloud cores, which pose serious challenges to companion searches. With extinctions that can exceed $A_V \sim 100$ mag, infrared, submillimeter or radio continuum techniques are required. Traditionally, protostars are categorized on the basis of their spectral energy distribution and relative amount of circumstellar envelope material. Class 0 sources are the least evolved objects, with more mass in the circumstellar material than in the central object, which makes them detectable only at longer wavelengths (submillimeter or radio). In contrast, the envelope mass of Class I sources is lower than that of the central object; they are often detectable at near-infrared wavelengths.

To date, about 350 Class I sources have been observed with seeing-limited imaging and about 100 of them with high-resolution imaging techniques. The direct imaging survey of Connelley et al. (2008) yielded 27 companions in the $200-2000$ AU range out of 136 targets, whereas the adaptive optics surveys of Duchêne et al. (2007) and Connelley et al. (2009) found 15 companions in the $50-200$ AU range out of 88 targets. Hence, the combined total frequency of companions to Class I sources in the

$50-2000$ AU separation range is $CSF^{ClassI} = 36.9 \pm 5.2\%$.

The rarity of Class 0 sources limits their observations to very small samples, which can yield uncertain statistics. The optimal observational probe of Class 0 multiplicity is millimeter ($850\mu m - 7mm$) interferometer mapping, with a typical linear resolution of only $50-100$ AU. Pioneering work was done by Looney et al. (2000), who observed 7 Class 0 and I sources; further samples of embedded sources were observed by, e.g. Chen et al. (2008; 2009), Maury et al. (2010), Enoch et al. (2011), and Tobin et al. (2013). However, no consensus on the Class 0 multiplicity is reached due to the limited sample size in each study. The combined 14 Class 0 sources of Looney et al. (2000) (BIMA) and Maury et al. (2010) (PdBI) appear to hint that the multiplicity of the most embedded protostars is likely lower than that of Class I sources over the $50-1500$ AU separation range (see also Enoch et al. 2011). On the other hand, Chen et al. (2013) presented 1.3mm and 850μm dust continuum data from the Submillimeter Array (SMA) for 33 Class 0 sources and found that no less than 21 of the sources show evidence for companions in the projected separation range from 50 to 5000 AU. They obtained a multiplicity frequency $MF^{Class0} = 64 \pm 8\%$ and a companion star fraction $CSF^{Class0} = 91 \pm 5\%$. This result is consistent with the possibility that most stars are born as binaries or multiples, although insufficient resolution and lack of kinematics data may reduce the credibility of their conclusion.

In summary, binary and multiple systems are common during all stages of stellar formation and evolution. There is a strong tendency of increasing binary frequency in the early phase of star formation. Thus, most stars may not be born single. It is of great importance to understand the theoretical mechanisms of the formation and subsequent dynamical evolution of binary and multiple systems, in order to explain the stellar population throughout our Galaxy. Because binaries are the majority of multiple systems, we focus on this type of simplest multiples in the thesis.

1.2 Theory of Binary Formation

The first mechanism of binary star formation was proposed by Laplace in 1796, in which he suggested a binary was formed from separate stellar nuclei that somehow came to orbit each other. Since then, five general mechanisms for binary star formation have been proposed. The first, capture, was suggested by Stoney in 1867, in which two independently-formed, unbound stars form a binary pair due to certain dissipative process. The second, fission, was proposed by Kelvin and Tait in 1883, and was strongly advocated by Jeans (1929). In the fission process, a single rapidly-rotating star near break-up splits into two objects due to dynamic instability. The final three mechanisms are core fragmentation, disk fragmentation and turbulent fragmentation, which all share similar physics of thermal and rotational instability.

Fragmentation in star formation was originally proposed by Hoyle (1953) for a dynamically-unstable isothermal cloud which fragments into several stellar cores as it collapses. This first process, called core or prompt fragmentation, provides a way of forming not only binaries, but higher-order multiple systems as well. The second mechanism of this type is the disk fragmentation, which requires a massive protostellar disk to become gravitationally unstable due to the growth of an $m = 1$ mode (accretion flow; e.g. Adams et al. 1989; Bonnell 1994; Kratter et al. 2010). Finally, recent studies have explored the turbulence induced fragmentation (Bate 2009a; Offner et al. 2010), where non-linear perturbations in a turbulent cloud can create sub-regions with high overdensities (low Jeans-mass) to condense into multiple protostellar seeds.

1.2.1 Capture

Two independently formed, unbound stars can become bound in a binary system if there is dissipation of their kinetic energy, which we name capture. The dissipation can occur in one of three ways, including 1) three-body encounter; 2) tidal interaction between two stars during close encounter (Press & Teukolsky 1977); and 3) two-body

interaction in a dissipative medium. Such a medium can either be residual gas left in a cluster after its formation, or gaseous disks surrounding one or both of the stars.

Capture through three-body interactions or tidal dissipation are most likely in very dense environments such as globular clusters (Portegies Zwart et al. 1997), in order to produce a high capture rate for forming bound binary systems. However, most star-forming regions are much more sparse than required for capture to be effective within ages of $< 10^6$ yr (e.g. Hill & Day 1976; Clarke 1992). This leaves the possibility of capture due to two-body interactions in a dissipative medium. The extended disks surrounding young stars have been shown to significantly affect capture rates, as the cross-section for disk interaction is increased dramatically over the three-body capture mechanism. Although low-velocity encounters between stars with disks can produce binaries, numerical simulations have shown that the relative stellar velocities in this scenario are too large for disks to absorb the corresponding kinetic energy (Clarke & Pringle 1993; Ostriker 1994). The calculation by Heller (1991) showed that the capture rate of two-body interactions could be as low as $0.05 - 0.1$ per star per 10^6 year in Orion. Hence, capture may play an important role in forming binary systems only in very dense star clusters.

1.2.2 Fission

The mechanism of binary formation via fission of a young protostar is expected to occur after a central core has condensed and started non-isothermal evolution. Upon forming the protostellar core by gas accretion, the protostar tends to spin-up because of angular momentum conservation. It is well-known that if the ratio of the rotational energy to the gravitational energy β exceeds a critical value, the object becomes unstable to non-axisymmetric perturbations (Lyttleton 1953; Ostriker & Bodenheimer 1973). The growth of these perturbations could lead to the breakup of the protostar into several orbiting components and to form binary systems. However, only close binaries may form by this method, due to the limited amount of angular momentum

contained in the protostar.

Hydrodynamical calculations have demonstrated that fission of a rapidly-rotating protostar usually does not occur (Durisen & Tohline 1985; Williams & Tohline 1988; Boss 1989b), because the fission mechanism depends crucially on the equation of state of the fluid. If the fluid is incompressible, fission may occur when the object flattens into an oblate spheroid shape in equilibrium. However, the fluid in protostars is highly-compressible; it is much denser towards the center. Such a configuration makes the fission mechanism difficult to operate. Instead, the rapidly spinning protostar deforms into a bar-shaped object with spiral arms at the ends of the bar. The spiral arms transport angular momentum outward from the core through gravitational torques, which will reduce β below the critical value for fission. This process takes place on the time scale of several rotation periods. Therefore, it appears that fission does not contribute significantly to the formation of binary systems.

1.2.3 Fragmentation

Core Fragmentation

A viable mechanism for the formation of binary systems is through core or prompt fragmentation, which happens either before or shortly after a free-fall collapse phase. First, during the isothermal collapse, the cloud quickly becomes Jeans unstable for fragmentation where the Jeans mass decreases with increasing density (e.g. Larson 1969; Boss & Bodenheimer 1979; Tohline 1982). A second such event could occur after the dissociation of molecular hydrogen, namely the near-isothermal second-collapse phase (Bonnell & Bate 1994b; Machida et al. 2008). In some situations, core fragmentation is still possible during the adiabatic phase (Machida et al. 2008).

Core fragmentation during the first collapse phase depends heavily on the initial density perturbations (e.g. Boss & Bodenheimer 1979), as well as anisotropic forces caused by the cloud rotation, magnetic field, and turbulence. For a non-magnetized

cloud in solid-body rotation, of spherical or spheroidal shape, the fragmentation is dependent on α_0 and β_0, the ratios of the initial thermal and rotational energies to the magnitude of the gravitational energy of the cloud, respectively. According to Miyama et al. (1984) and Tsuribe & Inutsuka (1999), fragmentation occurs if $\alpha_0\beta_0 < 0.12$, as long as the cloud remains isothermal. The resulting binary fragments are likely to have a separation of $10^2 - 10^4$ AU, which corresponds to the Jeans length in this phase. Thus in the non-magnetic regime, wide binary systems could form in a relatively fast rotating cloud with a large β_0 in this fashion.

During the adiabatic collapse phase, fragmentation is usually difficult because the thermal pressure tends to suppress the growth of any density perturbations in the core. However, fragmentation can still occur for cores with large rotation. For a molecular hydrogen ($\gamma = 1.4$) cloud, the fragmentation criterion roughly obeys $\alpha_0 < 0.09\beta_i^{0.2}$ (Boss 1986). In such conditions, the adiabatic core can fragment via a bar-like structure when the density perturbation is large, or via a ring-like structure when perturbation is small (Machida et al. 2008). Nevertheless, this still opens the questions of how to form very close binaries with separations < 1 AU. Bonnell & Bate (1994b) showed that close binary systems could form through fragmentation in the second collapse phase, while molecular hydrogen is dissociating and the gas polytropic index drops to around $\gamma = 1.1$. The binaries formed in this stage can have separations as close as a few stellar radii to ~ 1 AU.

Therefore, core fragmentation depends critically on the density and angular momentum distribution of a cloud in different phases. As we will also show in this thesis, the magnetic field can significantly alter the property of the resulting binary systems by affecting the angular momentum distributions in the cloud.

Disk Fragmentation

Fragmentation in rotationally-supported protostellar disks can occur either via rapid accretion onto massive disks, or through star-disk interactions in a dense cluster envi-

ronment. To achieve fragmentation, the disk has to become gravitationally unstable, which can be characterized by the Toomre parameter $Q \approx \Omega c_s/(\pi G\sigma)$ (where Ω is the angular velocity in the disk, c_s is the sound speed, and σ is the surface density). If $Q > 1$, the disk is locally stable against axisymmetric gravitational disturbances. However, it can be unstable to non-axisymmetric gravitational disturbances if $1 < Q \leq 3$. The two mechanisms for disk fragmentation mainly operate through these non-axisymmetric disturbances.

In the first mechanism, massive disks around protostars can become susceptible to gravitational instabilities if there is ongoing accretion onto the outer edge of the disk (Kratter et al. 2010). The observed T-Tauri disks typically contain only $\sim 1\% - 5\%$ of the primary stellar mass (Andrews & Williams 2005), but recent observations are beginning to reveal more massive disks at even earlier protostellar stages (Class 0 and I; Jørgensen et al. 2009; Tobin et al. 2012). Enoch et al. (2009) discovered a large embedded disk with $M_{disk} \sim 1.0\,\mathrm{M}_\odot$ and $R_{disk} \sim 300$ AU surrounding a Class 0 protostar in Serpens FIRS 1. Such embedded disks can continue to accrete from the outer collapsing envelope. When the rate of accretion onto the disk exceeds the rate onto the central star, mass starts to pile up in the disk, causing the massive disk to become gravitationally unstable and fragment. The secondary object born in the disk can accrete quickly to catch up with the primary in mass (Bonnell & Bate 1994a; Krumholz et al. 2009; Kratter et al. 2010).

The second mechanism occurs only in a very dense cluster environment where close encounters between young stars can disturb their circumstellar disks and excite a two-armed spiral mode (Watkins et al. 1998c; Thies et al. 2010) into the disks. The non-axisymmetric $m = 2$ mode can trigger gravitational instability that further fragments the circumstellar disks. However, this mechanism mostly leads to the formation of brown dwarfs and even planetary companions; it is not a significant contributor to the majority of binary systems. Variations of this mechanism include star-disk interactions and disk-disk interactions. The star-disk scenario usually in-

volves a nearly diskless perturber star interacting with a massive ($\sim 0.5\,M_\odot$) and extended ($\gtrsim$ 100 AU) disk (Boffin et al. 1998; Thies et al. 2010). In the case of disk-disk interaction, the gravitational instability is more likely to operate for non-coplanar disks (Watkins et al. 1998c). Furthermore, if the two circumstellar disks collide at the closest approach, the compressed disk material can sweep up into a shock layer that produces new protostellar condensations (Watkins et al. 1998b; Shen et al. 2010).

Turbulent Fragmentation

In contrast to the moderate perturbations typically envisioned in the core fragmentation mechanism, turbulent fragmentation is caused by strongly non-linear instabilities. The turbulent motion often drives sub-regions to become overdense and collapse more rapidly than the free-fall timescale of the background core, leading to the production of a secondary or multiple clumps.

Many observations show that cloud cores have significant non-thermal motions, which can be attributed to turbulence. The turbulence is thought to dissipate as a cloud collapses (e.g. Larson 1981). In the early phase of cloud collapse, the cloud can acquire angular momentum from turbulence, in addition to the large-scale ordered rotation of the cloud. Numerical simulations show that more fragments appear in a cloud with a larger turbulent energy in the initial state (Goodwin et al. 2007). Binary systems frequently form through turbulent fragmentation when the initial cloud has a turbulent energy exceeding $\sim 5\%$ of the gravitational energy (Goodwin et al. 2004a; 2004b). It is tempting to conclude that all stars are born as binary or multiple systems, even if a cloud core has a low level of turbulence. However, the binary frequency found in these turbulence calculations is higher than that observed, which is likely due to the neglect of the magnetic field and radiative feedback.

Numerical simulations with radiative feedback (Bate 2009b; Offner et al. 2009) have shown that fragmentation is dramatically suppressed for massive circumstellar

disks and dense filaments around existing protostars. The radiative heating from the central star stabilizes the circumstellar disk against small-scale fragmentation that would otherwise result in brown dwarfs. However, including radiation does not prohibit the formation of binary and multiple systems; fragmentation can still occur on scales of ~ 1000 AU during the early collapse of the turbulent core. On the other hand, the magnetic field is shown to be more catastrophic for fragmentation (e.g. Hennebelle & Teyssier 2008), as we discuss next.

1.3 Magnetic Field and Binary Star Formation

The importance of the magnetic field in binary formation has long been recognized (Bodenheimer 1995; Tohline 2002; Boss 2002). Observations of molecular clouds using polarimetry (e.g. Ward-Thompson 2000) have shown ample evidence for ordered magnetic fields on a wide range of scales (from tens of parsecs to 10^2 AU) and in different stages of star formation. For example, Fig. 1-1 shows a 10^3 AU-scale, pinched magnetic configuration in the dense core surrounding the protobinary system NGC 1333 IRAS 4A (Girart et al. 2006). This type of polarization observations only provide magnetic field directions on the plane of sky.

The strength of magnetic fields in star forming clouds can be measured through Zeeman effects (e.g. Troland & Crutcher 2008). The fields are observed to be strong enough to affect the dynamical evolution of protostellar systems. The relative importance of magnetic fields to self-gravity in a cloud is usually measured by the so-called "mass-to-flux ratio" λ in units of the critical value $(2\pi G^{1/2})^{-1}$ (Nakano & Nakamura 1978). If the cloud core has $\lambda < 1$, it can be supported by magnetic forces alone. Only in dense cores with $\lambda > 1$ can the self-gravity overwhelm the magnetic support and lead to core collapse and star formation. Troland & Crutcher (2008) carried out an extensive Zeeman survey of dense cores in nearby clouds, and determined a mean mass-to-flux ratio $\lambda \sim 4.8$; correcting for uncertain projection effects may bring this

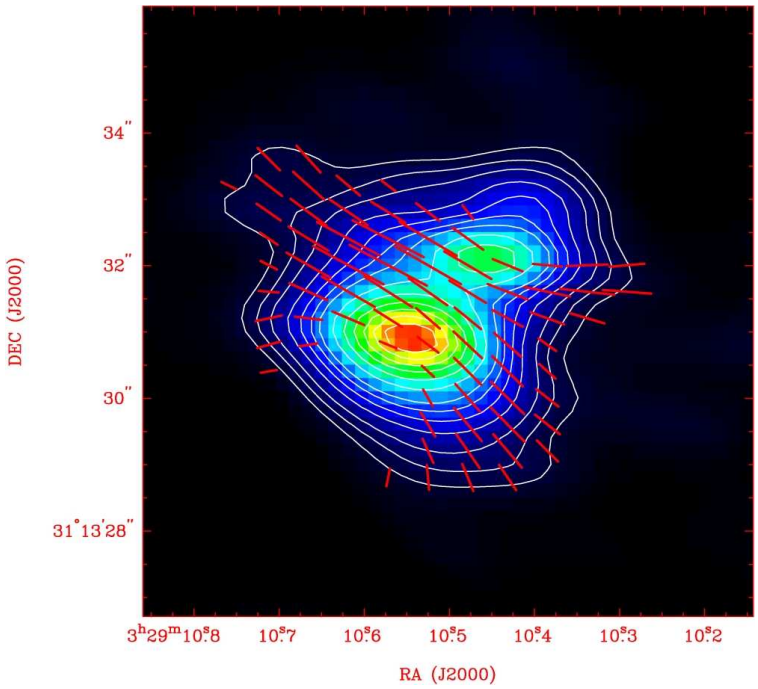

Fig. 1-1.— Ordered magnetic field (red line segments) as traced by polarized submillimeter emission from magnetically aligned dust grains in the envelope of the deeply embedded, accreting protobinary system IRAS 4A in NGC 1333 (Girart et al. 2006).

value to ~ 2. Therefore, dense cores are moderately magnetized, with λ typically of a few to several. Such magnetic fields are not able to prevent the cores from collapsing into stars, but are strong enough to fundamentally change the process of binary formation by redistributing the angular momentum.

Theoretically, both particle-based and grid-based magnetohydrodynamics (MHD) calculations suggest that a magnetic field of the observed strength tends to reduce the degree of fragmentation on the initial core and any circumstellar disk that is formed later. Such simulations typically start with a $\sim 1\,\mathrm{M}_\odot$ dense core that has an $m = 2$ mode perturbation on the initial density distribution (similar to the set-up of Boss & Bodenheimer (1979)). Thus the core has the propensity to become Jeans unstable on two well-separated density peaks early in the isothermal collapse; this belongs to the category of 'core fragmentation' introduced above. Machida et al. (2008) found that fragmentation into wide binaries could occur if the initial magnetized core rotates

fast enough; while close binaries could form if the initial magnetic energy was larger than the rotational energy. Hennebelle & Fromang (2008) and Hennebelle & Teyssier (2008) found that the magnetized core could only fragment when the initial density perturbation was large enough (with an amplitude relative to the background $> 50\%$). Price & Bate (2007) and Bürzle et al. (2011) showed that cores could collapse to form single, binary, or multiple protostar systems, depending on the initial magnetic field strength and its orientation relative to the rotation axis. When fragmentation does occur, binary star systems are the typical outcome, along with a few higher-order multiple systems.

Although the existing MHD studies have successfully captured the initial fragmentation leading to the formation of binary protostellar seeds, there has not been any systematic study of the effect of the magnetic field on the subsequent orbital evolution as the protobinary accretes mass from the gas envelope. The main goal of this thesis is to bridge the gap between the initial fragmentation phase and the protostellar accretion phase, and to obtain a more complete picture of magnetized binary star formation.

1.4 Thesis Overview

In this thesis, the role of magnetic fields on binary star formation and orbital evolution is examined in the ideal-MHD limit. We separate the stage of protobinary evolution from the initial fragmentation phase through modeling a pair of actively accreting protostellar seeds. After detailed investigations of the magnetic effect on protobinary orbital properties including separation and mass ratio, we revisit the classical problem of binary formation by Boss & Bodenheimer (1979) with much higher resolution and longer time into the binary evolution. The numerical simulations are carried out using the ENZO Adaptive-Mesh-Refinement (AMR) code, with a well-tested magnetohydrodynamics implementation and sink particle treatment that are

needed to tackle the magnetized binary formation problem. The thesis also compares the numerical results to existing observations.

In Chapter 2, an introduction to the AMR MHD code ENZO is given. Details of the Enzo algorithms including the magnetohydrodynamics solver and the sink particle treatment are described. The chapter concludes with a pure hydrodynamical test problem of the collapse of singular isothermal sphere, whose result is compared against the well-established analytical solution (Shu 1977).

Chapter 3 extends the numerical test to the collapse of a $1\,M_\odot$ dense core with an initially uniform density and magnetic field. The goal is to revisit the so-called magnetic flux problem in star formation through a detailed 3D ideal-MHD calculation. Because we do not assume any axisymmetry like in most previous studies (mainly in 2D), the decoupled magnetic flux from the matter that enters the star can freely expand to large distances along directions of least resistance. The expanding region is named as the "decoupling-enabled magnetic structure" (DEMS), whose role in stellar accretion and disk formation is investigated for both a non-rotating core and a rotating core. This work is the first exploration of what happens to the decoupled magnetic flux in 3D and has since been confirmed by several other groups (e.g. Seifried et al. 2011).

In Chapter 4, we focus on the second stage of binary formation and study the orbital evolution of a protobinary system under the influence of magnetic field. We initialize a magnetized singular isothermal sphere (SIS) with two protostellar seeds in the center. The self-similar solutions of the major binary properties are derived for the non-magnetic hydrodynamic case. These analytical solutions are directly compared with the simulation results from the magnetic cases. The work covers a large parameter space for the initial magnetic field strength. We first investigate the evolution of a equal-mass binary pair in the magnetized envelope, with a particular emphasis on the binary separation and orbital angular momentum. The effect of magnetic field on the morphology of circumstellar and circumbinary disks is also

discussed. In the end of chapter 4, we replace the initial equal-mass seeds with an unequal-mass binary pair, and follow the evolution of their mass ratio. The result from the magnetized cases can in principle explain the observed population of low mass-ratio binaries.

The study in Chapter 5 is motivated by recent CARMA observations (Hull et al. 2013), which show that the magnetic field in dense cores appears to be oriented at a random angle with respect to the rotation axis. Around single protostars, it has been shown that the field misalignment helps the protostellar accretion flow retain enough angular momentum to form large rotationally supported disks which are suppressed when the field and rotation are aligned (Joos et al. 2012; Li et al. 2013). We thus apply a similar idea to our models of protobinary evolution. The initial conditions are similar to the ones in Chapter 4, except for allowing the initial magnetic field direction to be misaligned with the cloud rotation. With the field misalignment, the more angular momentum retained in the circumbinary gas does not lead to a wider binary separation; instead, the binary is even tighter. To understand this somewhat unexpected result, the interdependence of the mass, separation and orbital angular momentum of the binary is examined with great care.

Having demonstrated the importance of the magnetic field for binary evolution during the protostellar accretion phase, Chapter 6 deals with the full problem of binary formation including both the prestellar and protostellar phases. We have carried out simulations for different initial core magnetization and field orientations. The early pre-stellar phase of isothermal collapse and fragmentation shows a good agreement with existing literature. We are able to follow the binary orbits self-consistently into the protostellar accretion phase. Finally, a new gravity solver for the sink particles is developed to fix the occasional star ejection caused by local numerical oscillations in the original solver. Currently, the simulations are not completed yet, but we are able to show preliminary results. We will leave the more detailed analysis to future studies.

Chapter 2

Numerical Tool: ENZO Adaptive-Mesh-Refinement Magnetohydrodynamic Code

2.1 Introduction

High performance computing has become a powerful tool for modern astrophysical research in recent years. Along with observations and analytical theory, it pushes forward our understanding of the cosmos. The complex and non-linear nature of many astrophysical problems, including star formation, makes analytical solutions difficult. The development of robust algorithms makes it possible to set up "numerical laboratories" for investigating the astrophysical processes, especially (magneto-)hydrodynamics.

The (magneto-)hydrodynamic algorithms generally divide into two classes: particle-based Lagrangian methods and grid-based Eulerian schemes. In order to follow the high spatial and temporal dynamical ranges involved in many astrophysical problems, the ability to adaptively refine a region when necessary is highly crucial. The particle method (the most commonly used is Smoothed Particle Hydrodynamics) has this adaptivity for free owing to its Lagrangian nature. Although the Eulerian solvers in their original form do not provide such adaptivity, the Structured Adaptive Mesh Refinement (S-AMR) introduced by Berger & Colella (1989) has since been successfully implemented in many grid-based codes including Enzo. The key principle of S-AMR is to adaptively add and modify finer meshes ("grids") over regions that require higher resolution. In the S-AMR framework, individual pieces of physics can be implemented, such as self-gravity, magnetohydrodynamics, radiative transfer, and sink particles; these features are included the ENZO code (Bryan & Norman 1997) that is used in this thesis.

Enzo is a fully parallelized, grid-based MHD code that has been extensively used over the past two decades on a wide variety of astronomical problems, including the large-scale structures, the interstellar and intergalactic medium, turbulent flows, and the formation of galaxies and the first stars. However, no application of Enzo has been made to the core collapse leading to the formation of individual stellar systems. The

physical module and numerical features of Enzo, especially the MHD solver and the sink particle treatment, make it well-suited for tackling the problem of star formation on the core scale (0.1 parsec) as shown in the following sections.

2.2 Enzo Algorithms

2.2.1 Adaptive Mesh Refinement

As a primary feature of Enzo, the AMR allows one to reach extremely large spatial and temporal dynamical ranges with limited computational resources. Often, the refinement occurs around small gravitational condensations or shocks. The S-AMR algorithm evolves the grid structures as follows. While solving the set of equations (e.g. MHD) on a coarse grid, the AMR solver monitors the quality of the solution and add finer (child) meshes to the regions that require higher resolution. These finer (child) meshes are then evolved as a separate initial boundary value (IBV) problem, whose boundary conditions are interpolated from the coarser (parent) grid or from other neighboring (sibling) grids with the same level of refinement. After evolving the finer grid, the updated physical quantities are used to improve the solution on its parent grid.

The hierarchy of grids is organized as a tree structure, which evolves recursively. The root of the tree is the uniform top-level Cartesian grid, which has no parent. Any other node in the tree represents a rectangular grid patch that is contained inside its corresponding parent grid one level coarser. This data structure is shown in Fig. 2-1. In addition, all grids on the same level are stored in an array of linked lists, which enables fast locating of sibling grids and facilitates communication between computation nodes.

Given the hierarchical structure of the grids, the time integration is also adaptive, i.e. each level l has its own time step dt_l. The evolution of grid hierarchy uses the so-called Breadth-first Search (BFS) strategy, as to traverse the tree from the top

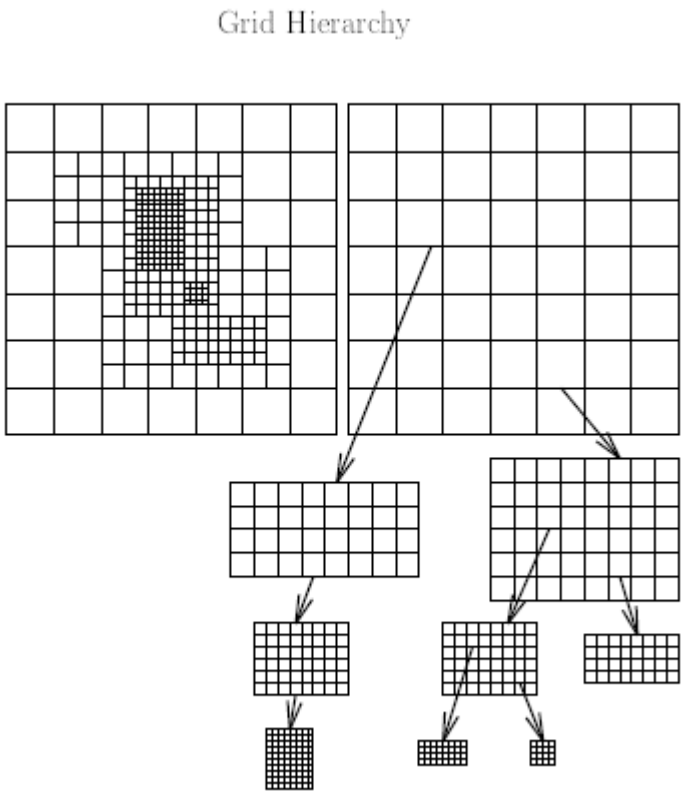

Fig. 2-1.— Illustration of an AMR grid hierarchy.

level to the bottom level. At a given time t, all the grids on the same level l will first evolve to $t + dt_l$. It then moves down to the next level $l + 1$ and advances all the grids on that level with timestep dt_{l+1} ($dt_{l+1} < dt_l$) continuously, until they "catch up" with the coarser parent grids at time $t + dt_l$. Then there will be an update step to modify the results of level l according to their underlying finer grids of level $l + 1$, or adjacent finer grids sharing common interfaces (the so-called "projection"). Afterward, all the grids at level l will advance by another dt_l. This procedure repeats itself until all grids have been advanced by the desired time (see Fig. 2-2).

The adaptive creation or removal of finer grids happens when a level $l + 1$ has caught up to its parent level l, at which the entire hierarchy at level $\geq l$ will be reconstructed. The hierarchy rebuilding is achieved by applying certain refinement

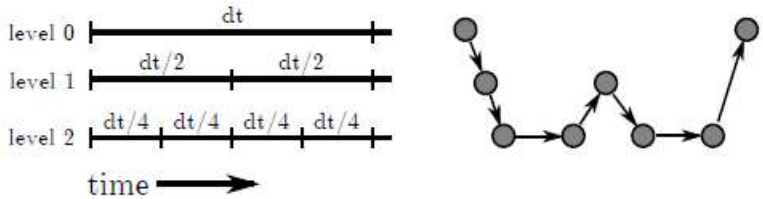

Fig. 2-2.— Left: Example of the timesteps on a 2-level AMR hierarchy. Enzo does not restrict the timesteps on the finer levels to be a factor of $1/2^n$ smaller. Right: The order in which the AMR grids are evaluated on each level.

criteria to the grids, and flagging zones that require extra grids. Such criteria depend on the physical problem being simulated, e.g. the slope of density to capture shocks. Once the new subgrids have been identified, the solutions from their parent grids are interpolated in order to initialize the values on these new grids. Finally, any overlap between the new subgrids and the old ones is identified, and the previous solutions in overlapping regions is copied to the new subgrids. In this way, the entire hierarchy can be rebuilt.

In summary, the AMR algorithm for any given level can be written as the following pseudo-code:

```
EvolveLevel(level, ParentTime)
   SetBoundaryValues
   while (Time < ParentTime):
      dt = ComputeTimeStep(level)
      PrepareDensityField(dt)
      SolveHydroEquations(dt)
      SolveOtherEquations(dt)
      SetBoundaryValues
      EvolveLevel(level+1, Time)
      Time = Time + dt
      FluxCorrection
```

```
    Projection
    RebuildHierarchy(level+1)
```

The pseudo-code for grid hierarchy reconstruction at every time step reads as follows,

```
RebuildHierarchy(level)
  for i_level = level to MaximumLevel - 1
      for every grid on i_level
          FlagCellsForRefinement
          CreateSubgrids
          AddLevel(i_level+1)
      for every new subgrid
          InterpolateFieldValuesFromParent
          CopyFromOldSubgrids
```

2.2.2 Finite Volume Method

There are four classes of popular computational fluid dynamics (CFD) algorithms: finite difference method, finite volume method, finite element method and spectral method. Because of the advantage on shock-capturing, finite volume method has become the most popular method for astrophysical Eulerian fluid solver in recent years. It is best used to solve a system of conservation laws of the form

$$\frac{\partial \mathbf{u}}{\partial t} + \nabla \cdot \mathbf{f}(\mathbf{u}) = 0. \tag{2.1}$$

where $\mathbf{u}$ represents a vector of states and $\mathbf{f}$ represents the corresponding flux tensor or flow of $\mathbf{u}$.

The conservative nature of finite volume method can be derived easily. After subdividing the spatial domain into finite volumes or cells, the volume integral of Eq. 2.1

over a particular cell i gives,

$$\int_{V_i} \frac{\partial \mathbf{u}}{\partial t} \, \mathrm{d}V + \int_{V_i} \nabla \cdot \mathbf{f}(\mathbf{u}) \, \mathrm{d}V = 0. \tag{2.2}$$

By approximating the first term using the volume averaged values and applying the divergence theorem to the second term, we can get,

$$\frac{d\bar{\mathbf{u}}_i}{dt} + \frac{1}{V_i} \oint_{S_i} \mathbf{f}(\mathbf{u}) \cdot \mathbf{n} \, \mathrm{d}S = 0. \tag{2.3}$$

Because the change of cell averages is the negative flux through the cell edges, the flux is conserved from cell to cell.

Following this classical finite volume framework, Enzo employs the Godunov (Godunov 1959) MUSCL (*Monotonic Upstream-Centered Scheme for Conservation Laws*) scheme for solving the MHD equations; the method also provides a second-order accurate solution to the Riemann problems across the cell boundary. The basic algorithm of Godunov's scheme can be implemented through the method of lines (LeVeque 2002). After discretization of Eq. 2.1 in both space and time, the conservation law can be written in the integral form as,

$$\int_C \mathbf{u}(\mathbf{x}, \mathbf{t}_{n+1}) \, \mathrm{d}x - \int_C \mathbf{u}(\mathbf{x}, \mathbf{t}_n) \, \mathrm{d}x = \int_{t_n}^{t_{n+1}} \mathbf{f}(\mathbf{u}(\mathbf{x}_0, t)) \, \mathrm{d}t - \int_{t_n}^{t_{n+1}} \mathbf{f}(\mathbf{u}(\mathbf{x}_1, t)) \, \mathrm{d}t \tag{2.4}$$

where $\mathbf{C} = [\mathbf{x}_0, \mathbf{x}_1]$ is the domain of interest. In 1-dimension for example, the domain can be discretized into N intervals as $C_i = [x_{i-1/2}, x_{i+1/2}]$, with x_i being the center of the i-th cell. At time t_n, the average value over the i-th interval can be approximated by the discrete value u_i^n. Hence, for each interval C_i, Eq. 2.4 is evaluated as,

$$u_i^{n+1} - u_i^n = \frac{\Delta t}{\Delta x} (\mathbf{f}(u_{i-1/2}) - \mathbf{f}(u_{i+1/2})) \tag{2.5}$$

In order to minimize the oscillation of the solution near discontinuities or shocks, it is

necessary to extrapolate the flux in Eq. 2.5 at the slope limited left and right states, e.g. $u^L_{i+1/2}$ and $u^R_{i+1/2}$ for $u_{i+1/2}$; this is the basic idea of the MUSCL scheme. This type of conservative method is able to capture the correct shock speed even at low resolutions (LeVeque 2002), which is crucial for many astrophysical problems.

The Godnov's scheme solves the equation of conservation (Eq. 2.1) in three basic steps. Suppose the volume-centered solution in each cell is known at time $t = n\Delta t$. The first step is to reconstruct the face-centered left and right states from the volume-centered quantities. Step 2 is the only physical step; it obtains the solution for the Riemann problem at the cell interfaces using the left and right values calculated in step 1. The final step is to update the conserved quantities after time interval Δt using the fluxes obtained in step 2. Note that the time interval Δt should be limited such that the waves emanating from an interface do not interact with waves created at the adjacent interfaces. This leads to the CFL (Courant-Friedrichs-Lewy) condition $|v_{max}| < \frac{\Delta x}{2\Delta t}$ where $|v_{max}|$ is the maximum wave speed obtained from the cell eigenvalues of the local Jacobian matrix (Courant, Friedrichs, & Lewy 1928).

Because of the purely numerical nature of the first and third step, one can modify them without affecting the physical step. For example, several distinct reconstruction methods are implemented in Enzo, including the piecewise linear method (PLM, van-Leer 1979), and the piecewise parabolic method (PPM, Colella & Woodward 1984), etc. There are also different Riemann solvers implemented in Enzo, such as the HLL (Harten-Lax-van Leer) solver (Harten et al. 1983), the HLLC (Harten-Lax-van Leer with Contact) solver (Toro 1999), the LLF (Local Lax-Friedrichs) solver (Kurganov & Tadmor 2000), and the Roe solver (Roe 1981).

2.2.3 Magnetohydrodynamics

The above finite volume method can be used to solve the set of ideal magnetohydrodynamics equations. The main challenge is to maintain the divergence-free condition for the magnetic field, as magnetic monopoles tend to be generated numerically. Var-

ious schemes have been proposed for this purpose. The two most popular approaches are Dedner's hyperbolic cleaning method (Dedner et al. 2002) and constrained transport method (Evans & Hawley 1988); both have been implemented in the Enzo code. However, the latter has not been well-tested at this stage. In this thesis, we will mainly adopt the Dedner's cleaning scheme, whose algorithm is described below.

The set of ideal MHD equations in the conservative form can be written as,

$$\frac{\partial \rho}{\partial t} + \nabla\cdot(\rho\mathbf{v}) = 0, \tag{2.6}$$

$$\frac{\partial \rho\mathbf{v}}{\partial t} + \nabla\cdot(\rho\mathbf{v}\mathbf{v} + \mathbf{I}(p + \frac{\mathbf{B}\cdot\mathbf{B}}{2}) - \mathbf{B}\mathbf{B}) = -\rho\nabla\phi, \tag{2.7}$$

$$\frac{\partial E}{\partial t} + \nabla\cdot[(E + p + \frac{\mathbf{B}\cdot\mathbf{B}}{2})\mathbf{v} - \mathbf{B}(\mathbf{v}\cdot\mathbf{B})] = -\rho\mathbf{v}\cdot\nabla\phi, \tag{2.8}$$

$$\frac{\partial \mathbf{B}}{\partial t} + \nabla\cdot(\mathbf{v}\mathbf{B} - \mathbf{B}\mathbf{v}) = 0, \tag{2.9}$$

where $\mathbf{v} = (v_x, v_y, v_z)$ denotes the fluid velocity, $\mathbf{B} = \frac{1}{\sqrt{4\pi}}(B_x, B_y, B_z)$ the magnetic field, ρ the density, p the pressure, $\mathbf{I}$ the second order identity tensor, and E the energy given by,

$$E = \frac{p}{\Gamma - 1} + \rho\frac{\mathbf{v}\cdot\mathbf{v}}{2} + \frac{\mathbf{B}\cdot\mathbf{B}}{2}, \tag{2.10}$$

with $\Gamma > 1$ denotes the adiabatic index. The equations are closed by Poisson's equation for the gravitational potential ϕ:

$$\nabla^2\phi = 4\pi G(\rho_{total} - \rho_0). \tag{2.11}$$

Note that in Enzo the source term on the right-hand-side is the total mass density contrast, i.e. $\rho_{total} = \rho_{gas} + \rho_{stars}$ and ρ_0 is the mean density. For the magnetic field we have the divergence constraint $\nabla\cdot\mathbf{B} = 0$, which always holds physically. However, numerical simulations often introduce errors that will propagate in space and over time, leading to violation of the divergence free condition. Whenever $\nabla\cdot\mathbf{B} \neq 0$, the

solution becomes unphysical.

The Dedner's divergence cleaning method solves the Generalized Lagrangian Multiplier (GLM) formulation of MHD equations with an additional scalar field ψ that satisfies a hyperbolic equation, as shown below.

$$\frac{\partial \rho}{\partial t} + \nabla\cdot(\rho\mathbf{v}) = 0, \tag{2.12}$$

$$\frac{\partial \rho\mathbf{v}}{\partial t} + \nabla\cdot(\rho\mathbf{v}\mathbf{v} + \mathbf{I}(p + \frac{\mathbf{B}\cdot\mathbf{B}}{2}) - \mathbf{B}\mathbf{B}) = -\rho\nabla\phi - \mathbf{B}(\nabla\cdot\mathbf{B}), \tag{2.13}$$

$$\frac{\partial E}{\partial t} + \nabla\cdot[(E + p + \frac{\mathbf{B}\cdot\mathbf{B}}{2})\mathbf{v} - \mathbf{B}(\mathbf{v}\cdot\mathbf{B})] = -\rho\mathbf{v}\cdot\nabla\phi - \mathbf{B}\cdot(\nabla\psi), \tag{2.14}$$

$$\frac{\partial \mathbf{B}}{\partial t} + \nabla\cdot(\mathbf{v}\mathbf{B} - \mathbf{B}\mathbf{v} + \psi\mathbf{I}) = 0, \tag{2.15}$$

$$\frac{\partial \psi}{\partial t} + c_h^2\nabla\cdot\mathbf{B} = -\frac{c_h^2}{c_p^2}\psi, \tag{2.16}$$

where c_h and c_p are constants controlling the propagation speed and damping rate of $\nabla\cdot\mathbf{B}$. Eq. 2.16 takes this particular form so that $\nabla\cdot\mathbf{B}$ and ψ satisfy the same differential equation, and that local divergence errors only propagate with finite speed and dissipate quickly (see Dedner et al. (2002) for detailed derivations).

Note that in the GLM-MHD equations, all quantities are stored as volume-centered, it is thus straightforward to solve this GLM-MHD system using the Godunov scheme described in § 2.2.2. Besides, the method is dimensionally un-split in that the fluxes are computed for all dimensions (x, y, and z) together, which is a rather stable and self-consistent implementation in the current Enzo framework.

2.2.4 Sink Particle Treatment

The binary star formation problem we are investigating involves a vast dynamical range, which makes its full solution computationally infeasible even with the AMR capability. Spatially, the problem spans an order of $\sim 10^7$ in length from the initial

molecular cloud core ($\sim 0.1 - 1.0$ pc) to the final stellar size object (10^{11} cm). It is impossible to carry out a single simulation to resolve both the largest and the smallest structures, as the number of cells needed grows exponentially with increasing resolution. Temporally, the CFL condition requires that the timestep of a certain refinement level be less than the signal-crossing time of any grid cell on that level. The hydrodynamics timestep can become smaller either by increasing spatial resolution or through local density enhancement, as the time scale set by self-gravity varies $\propto \rho^{-1/2}$. Often, the smallest timestep occurs in cells near the center of a collapsing core, where the density can exceed 10^6 times that of the background. Therefore, it is desirable to stop following the collapse at a certain scale, so as to prevent the timestep from approaching a prohibitively small value and the number of finer cells from increasing out of control.

In light of the above limitations, researchers have introduced the sink particle: a Lagrangian point that accretes incoming material but has no internal structure; therefore, no higher resolution is required for either time or space. It enables us to focus the majority of computational effort on length scales (from 10^{17} cm to 10^{13} cm) that matter most to the problem of star and disk formation.

Another advantage of sink particle is to prevent artificial fragmentation caused by insufficient resolution near high density regions. According to Truelove et al. (1997), at least four cells are required to resolve one Jeans length ($\lambda_J \propto \rho^{-1/2}$), known as the Truelove's criterion. Since it is computationally difficult to resolve the Jeans length all the way to the stellar density, sink particles can be created to handle the gravitational collapse at high densities beyond what the maximum refinement level could resolve.

The basic treatment of a sink particle includes: creation, accretion, merging with other sinks, and gravitationally interacting with gas and other sinks. The implementation of sink particles is as follows. When a cell violates the Truelove's criterion on the highest refinement level, a new sink particle is inserted at the center of that cell.

The initial mass of the sink particle is calculated such that after subtracting the sink mass, the cell no longer violates the Truelove's criterion. The initial velocity of the sink particle is calculated using momentum conservation.

After creation, the sink particle accretes gas from its host cell according to the formula of modified Bondi-Hoyle (BH) accretion (Ruffert 1994),

$$\dot{M}_{BH} = 4\pi\rho_{\infty} r_{BH}^2 \sqrt{1.2544 c_{\infty}^2 + v_{\infty}^2}, \tag{2.17}$$

where r_{BH} is the Bondi radius, ρ_{∞}, v_{∞} and c_{∞} are the gas density, velocity and sound speed of the (uniform) medium far from the point mass. In the code, the c_{∞} is set to the sound speed c_s, and $v_{\infty} = v_{cell} - v_{sink}$. The r_{BH} is calculated as $r_{BH} = GM_{sink}/(c_{\infty}^2 + v_{\infty}^2)$. If the r_{BH} is smaller than the cell size Δx, the cell density ρ_{cell} is used for ρ_{∞}; otherwise an extrapolation assuming an $r^{-1.5}$ density profile is used.

A merging algorithm for sink particle is necessary to ensure the correctness of the mass accretion prescription, and to save computation time when many sink particles are created within a small volume. The sink particle merging is controlled by two parameters: a merging mass M_{merg} and a merging distance l_{merg}. In every timestep, the merging is done in two steps. First, each small particle is merged to the nearest big particle within the merging distance. Second, all remaining small particles after the first step are grouped together using a Friend-of-Friend algorithm, in which the merging distance l_{merg} is chosen as the linking length (Davis et al. 1985).

Finally, the gravity of sink particles is calculated using the particle-mesh method. First, the masses of sink particles are deposited onto the grids using the cloud-in-cell (CIC) interpolation technique to form a spatially discretized density field. Then the total density field ($\rho_{total} = \rho_{gas} + \rho_{sink}$) is used to calculate the gravitational potential on the periodic root grid (level = 0) through fast Fourier transformation. The potential fields on finer grids are calculated by a multigrid relaxation technique,

whose boundary conditions are interpolated from the potential values on their parent grid. Gravitational accelerations are computed by finite-differencing potential values and are then interpolated to the particle locations, where they are used to update the particle's position and velocity within one hydrodynamic timestep. This procedure runs recursively on all child grids. Note that sink particles are stored in the highest refinement level, and particles that move out of a subgrid patch are sent to adjacent grid patches with the finest spatial resolution.

2.3 Collapse Test Problem

To ensure that the Enzo code is suitable for our study of star formation on the core scale, we run a simple collapse test of a singular-isothermal-sphere (SIS) whose analytical solution has been given by Shu (1977). The initial conditions of the cloud core are as follows,

$$\rho(r) = \frac{Ac_s^2}{4\pi G r^2}, \tag{2.18}$$

$$v_\phi = 0, B_0 = 0, \tag{2.19}$$

$$R_0 = 10^{17}\ \mathrm{cm}, M_{total} \approx 1.2\,\mathrm{M}_\odot, \tag{2.20}$$

$$M_{seed} = 0.025\,\mathrm{M}_\odot, \tag{2.21}$$

where the density is distributed as r^{-2}, R_0 and M_{total} are the initial size and mass of the core, respectively; G is the gravitational constant, $c_s = 2\times10^4$ cm/s the isothermal sound speed, and A is an overdense factor whose value must be greater than 2 for the collapse to occur. We choose $A = 4$ in this test simulation; the core is out of hydrostatic equilibrium initially and will start to collapse towards the cloud center immediately. Note that the name "singular" comes from the unphysical density at zero radius where it becomes infinity. To avoid this singular point computationally, we flatten the density profile inside the innermost $\sim$ 130 AU initially and replace

the mass deficit there ($0.025\,\mathrm{M}_\odot$) with a tiny sink particle M_{seed} in the center of the cloud.

As shown by Shu (1977), the collapse of a singular isothermal sphere proceeds in a self-similar fashion, meaning that any state of the system is a rescaled copy of the initial state, or that the cloud looks the same at all times except for scale. The self-similar solution also predicts analytically the mass accretion rate into the singularity point - the stellar object - as,

$$\dot{M} = 5.58 c_s^2/G = 1.06 \times 10^{-5}\,\mathrm{M}_\odot/\mathrm{yr} \tag{2.22}$$

for $A = 4$ in our test. Encouragingly, our simulation result presents a nearly perfect match with this analytical expectation, see Fig 2-3. This is a robust test of the reliability and performance of Enzo code, which allows us to move forward to the more complicated problem of binary star formation.

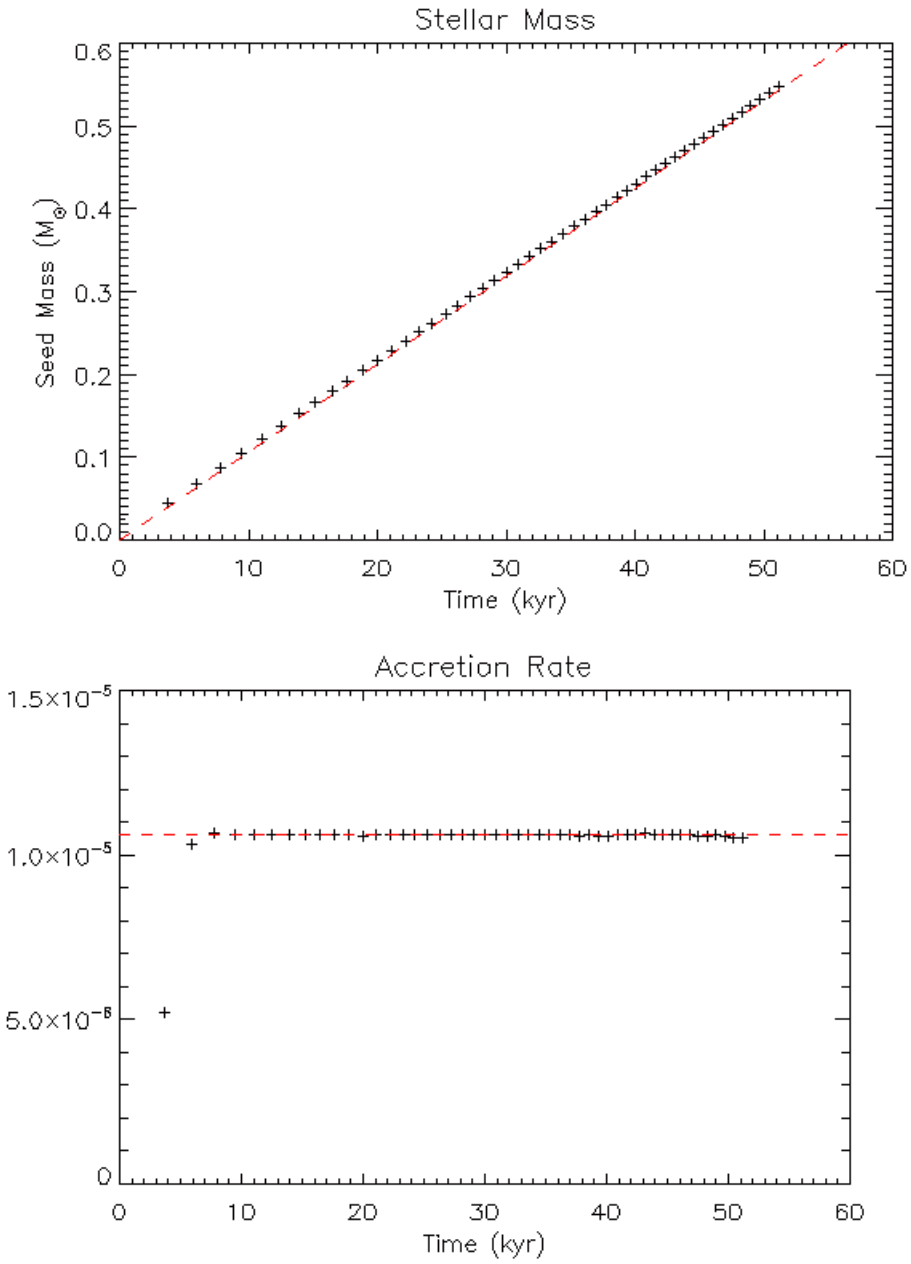

Fig. 2-3.— Top: Mass growth of the sink particle over time; bottom: Mass accretion rate of the sink particle. Red dashed line denotes the analytical solution, and black cross denotes results from the test simulation.

Chapter 3

Magnetic Flux Expulsion in Star Formation

This chapter is based on the published paper of Zhao et al. (2011, ApJ, 742, 10).

3.1 Introduction

A longstanding problem in star formation is the so-called "magnetic flux problem" (e.g., Nakano 1984, see his § 4). If the magnetic flux observed to thread a typical star-forming dense core (Troland & Crutcher 2008) were to be dragged into a young stellar object, the stellar field strength would be tens of millions of Gauss, more than three orders of magnitude higher than the observed values (which are typically in the kilo-Gauss range, e.g., Johns-Krull 2009). The vast majority of the original magnetic flux of the dense core must be decoupled from the matter that enters the star. When and how the decoupling occurs is a fundamental problem of star formation that has yet to be completely resolved.

The magnetic flux problem lies at the heart of another fundamental problem in star formation: disk formation. If the magnetic flux of a dense core is dragged by the collapsing material into a forming star, as would be in the ideal MHD limit, it would form a central split magnetic monopole that prevents the formation of a rotationally supported disk through catastrophic magnetic braking (Allen et al. 2003; Galli et al. 2006; Mellon & Li 2008; Hennebelle & Fromang 2008; Seifried et al. 2011). The magnetic flux problem must be resolved in order for rotationally supported disks to form.

The most widely discussed resolution of the magnetic flux problem is through non-ideal MHD effects, including ambipolar diffusion, Ohmic dissipation and potentially Hall effect (e.g., Nakano 1984; Li & McKee 1996; Ciolek & Königl 1998; Tassis & Mouschovias 2007; Kunz & Mouschovias 2010; Krasnopolsky et al. 2011). For example, Li & McKee (1996) showed that ambipolar diffusion can enable the protostellar envelope to collapse into the central stellar object without dragging along the magnetic flux. The left-behind magnetic flux builds up in a small circumstellar region, confined by the ram pressure of the protostellar collapse. It tends to dominate the gas dynamics close to the protostar, particularly in the region of disk formation.

Indeed, the magnetic field accumulated at small radii can be strong enough to suppress disk formation completely through efficient magnetic braking (Krasnopolsky & Königl 2002; Mellon & Li 2009; Li et al. 2011). In this case, the resolution of the magnetic flux problem for the central star does not lead to a resolution of the magnetic braking problem for disk formation.

There is, however, a significant limitation in the (non-ideal MHD) studies of the magnetic flux problem and its consequences to date: the assumption of axisymmetry. Although the axisymmetry greatly reduces the computational demand of the calculations, it limits how fast the magnetic flux released from the central object can expand to large distances. In particular, it suppresses a likely mode for the flux expulsion: dynamic expansion along the direction(s) of least resistance. In this Chapter, we describe the first detailed 3D study of what happens to the released flux using the Enzo MHD code. We find that a magnetically dominated region is inflated by the released flux. The region expands asymmetrically away from the central object, changing the dynamics of the protostellar accretion and disk formation.

The rest of the chapter is organized as follows. In § 3.2, we describe the problem setup, including the equations to be solved, numerical method, and initial and boundary conditions. The numerical results are presented and interpreted in § 3.3. The last section, § 3.4, includes a discussion of the main results and a short summary.

3.2 Problem Setup

3.2.1 Basic Equations and Numerical Method

We study the formation of stars from the collapse of magnetized dense cores of molecular clouds using the ENZO MHD code that includes a sink particle treatment. The usual MHD equations are the magnetic induction equation,

$$\frac{\partial \mathbf{B}}{\partial t} = \nabla \times (\mathbf{v} \times \mathbf{B}), \tag{3.1}$$

and the equations for mass continuity, momentum and self-gravity,

$$\frac{\partial \rho}{\partial t} + \nabla \cdot (\rho \mathbf{v}) = 0, \tag{3.2}$$

$$\rho \frac{\partial \mathbf{v}}{\partial t} + \rho(\mathbf{v} \cdot \nabla)\mathbf{v} = -\nabla P - \frac{1}{4\pi}\mathbf{B} \times (\nabla \times \mathbf{B}) - \rho \nabla \phi, \tag{3.3}$$

$$\nabla^2 \phi = 4\pi G(\rho_{total} - \rho_0), \tag{3.4}$$

where ϕ is the gravitational potential, $\rho_{total} = \rho_{gas} + \rho_{stars}$, and ρ_0 is the mean density.

The above equations are solved in three dimensions using a MHD version (Wang & Abel 2009) of the ENZO adaptive mesh refinement code (Bryan & Norman 1997; O'Shea et al. 2004). It incorporates a sink particle treatment (Wang et al. 2010). The magnetic field is evolved with a conservative MHD solver that includes the hyperbolic divergence cleaning of Dedner et al. (2002), as described in Chapter 2. The MHD version of the code is publicly available from the ENZO website at *http://code.google.com/p/enzo/*. It has been used to follow successfully the formation and evolution of magnetized galaxies (Wang & Abel 2009) and star clusters (Wang et al. 2010).

Our goal is to follow both the prestellar core evolution as well as the protostellar mass accretion phase of star formation (after a central stellar object has formed). For the latter, it is crucial to use a sink particle to approximate the stellar object, because including the object in the computation without any special treatment would reduce the time step to such a small value that the simulation would grind to a halt (e.g., Krumholz et al. 2004). In our simulations, we resolve the so-called "Jeans length" defined as $L_J = c_s \left(\frac{\pi}{G\rho}\right)^{1/2}$ (where c_s is the isothermal sound speed), everywhere by at least 8 cells, so that the Truelove's criterion (Truelove et al. 1997) is satisfied. When the density in a cell at the highest refinement level exceeds a threshold density ρ_{th} (to be defined below), a sink particle is created at the cell center (see Federrath et al.

2010 for a more elaborate treatment of sink particle). The particle is evolved using an algorithm that is described in detail in Wang et al. (2010).

Briefly, the mass accretion rate onto a sink particle is done in two steps. First, the particle accretes from its host cell using a formula inspired by that of Bondi-Hoyle accretion (Ruffert 1994). The momentum of the accreted material is added to that of the sink particle. The second step involves the merging of small sink particles. This step is controlled by two parameters: the merging mass M_{merg} and merging distance l_{merg}. They are chosen to eliminate artificial particles and to maximize computation efficiency. The simulations presented in this Chapter use $M_{merg} = 0.01\,\mathrm{M}_{\odot}$ and $l_{merg} = 10^{15} cm \approx 8\Delta x \approx 70 AU$. Our main results are insensitive to these parameters as long as they are reasonably small.

When a mass is extracted from a cell, due to either sink particle formation or accretion onto an existing sink, the magnetic field in that cell is not altered. That is, the field strength remains the same. This is a crude way to represent the decoupling of the magnetic field from matter at high densities that is expected physically (Nakano et al. 2002) and demanded by the relatively weak magnetic fields observed on young stars (see discussion in § 3.1). Determining what happens to the decoupled magnetic flux in 3D is the main goal of our investigation in this Chapter.

3.2.2 Initial and Boundary Conditions

We model star formation in a magnetized dense core embedded in a more diffuse ambient medium. We choose a spherical core of radius $R = 5 \times 10^{16}$ cm and an initially uniform density $\rho_0 = 5 \times 10^{-18}$ g cm^{-3}. These parameters yield a core mass $M = 1.32\ \mathrm{M}_{\odot}$ and a free-fall time $t_{ff} = 9.4 \times 10^{11}$ sec $= 29.8$ kyrs. We embed the core in an ambient medium that is 100 times less dense than the core and that fills the entire computational box, which is much larger than the core, with $L = 5 \times 10^{17}$ cm on each side. We set the temperature for both the core and the ambient gas to be $T \sim 10K$ initially. The large box size is chosen to minimize the effects of the periodic

boundary conditions on the core dynamics; the conditions are adopted to facilitate the computation of self-gravity (through fast Fourier transform on the base grid). Our initial conditions are similar to those adopted by Price & Bate (2007), Hennebelle & Fromang (2008) and Bürzle et al. (2011).

As usual, we adopt a barotropic equation of state (EOS) that mimics the isothermal EOS at low densities and the adiabatic EOS at high densities:

$$P = \rho c_s^2 \left[1 + \left(\frac{\rho}{\rho_{crit}} \right)^{2/3} \right], \tag{3.5}$$

with a critical density $\rho_{crit} = 10^{-13}$ g cm^{-3} for the transition between the two regimes. An isothermal sound speed $c_s = 0.2$ km/s is chosen, corresponding to a temperature $T \sim 10$ K. The sound speed yields a ratio of thermal to gravitational energy $\alpha = 2.5Rc_s^2/(GM) = 0.29$ for the core (Truelove et al. 1998). For simplicity, we impose an initially uniform magnetic field everywhere along the $z-$axis, with a strength $B_0 = 2.7 \times 10^{-4}$ G. It corresponds to a dimensionless mass-to-flux ratio $\lambda_{core} = 2$ for the core as a whole, in units of the critical value $(2\pi G^{1/2})^{-1}$; such a value is consistent with those predicted in dense cores formed in strongly magnetized clouds through ambipolar diffusion (e.g., Lizano & Shu 1989; Basu & Mouschovias 1994; Nakamura & Li 2005), and with the median value inferred by Troland & Crutcher (2008) for a sample of dark cloud cores (after correcting statistically for projection effects). We have also carried simulations for both weaker and stronger field cases, with $\lambda_{core} = 4$ and 1 respectively, and found qualitatively similar results. We should note that the local mass-to-flux ratio on the central magnetic flux tube is somewhat larger than the value for the core as a whole, by a factor of 1.5.

Besides the magnetic field, we impose, in some cases, a rigid body rotation on the core. We adopt an angular velocity of $\Omega = 4.0 \times 10^{-13}$ s^{-1}, corresponding to a ratio of rotational and gravitational energy $\beta = 0.036$. This value is within the range inferred by Goodman et al. (1993) from NH_3 observations of dense cores.

We choose a relatively coarse base grid of 64^3, although the grid is automatically refined, at the beginning of the simulation, by one level in the central part of the computational domain that includes the dense core. We set the maximum refinement level to 6 for our reference runs, which yields a smallest cell size of $\Delta x \sim 8$ AU. When the Truelove criterion (with a Jeans number $\Delta x/L_j = 1/8$, Truelove et al. 1997) is violated on the finest grid at a threshold density of $\rho_{th} = \frac{\pi c_s^2}{G(8\Delta x)^2} = 2.0 \times 10^{-14}$g cm^{-3}, a sink particle is created. Effectively, ρ_{th} sets the density above which the gas and magnetic field are decoupled. It corresponds to a hydrogen number density of about 10^{10} cm^{-3} for the reference runs, which is somewhat below the decoupling density (of a few times 10^{11} cm^{-3}) advocated by Nakano et al. 2002. We have experimented with maximum refinement levels up to 8 (which has a threshold number density of about 2×10^{11} cm^{-3}), and obtained qualitatively similar results (see below).

3.3 Results

We carry out two sets of simulations: collapse with or without rotation. The former is to illustrate how the magnetic flux decoupled from the stellar material escapes to large distances and the latter the effects of the escaping flux on disk formation.

3.3.1 Non-Rotating Collapse

Sink Particle Evolution

At the heart of our star formation calculation lies the sink particle treatment. As mentioned in § 3.2.1, the treatment is needed to allow the simulation to go beyond the initial prestellar core evolution phase of star formation, into the protostellar mass accretion phase. Just as importantly, it provides a simple way to decouple the magnetic flux from the material that enters the protostellar object, as demanded by observations (see discussion in § 3.1).

In the left panel of Fig. 3-1, we plot the mass of the star, as represented by the sink particle, as a function of time. The object first appears around $t \approx 36$ kyrs (or $\sim 1.2\ t_{ff}$). It grows quickly, with a relatively large initial mass accretion rate of $10^{-4}\,\mathrm{M}_\odot\ \mathrm{yr}^{-1}$. The high initial accretion rate is expected for the uniform density distribution that we adopted for the dense core. It could plausibly be identified with the Class 0 phase of low-mass star formation (André et al. 1993). The accretion rate decreases below $10^{-5}\,\mathrm{M}_\odot\ \mathrm{yr}^{-1}$ after $t = 48$ kyrs (or $\sim 1.6\ t_{ff}$), when $\sim 0.75\,\mathrm{M}_\odot$ (or 57% of the initial core mass) has landed on the central star.

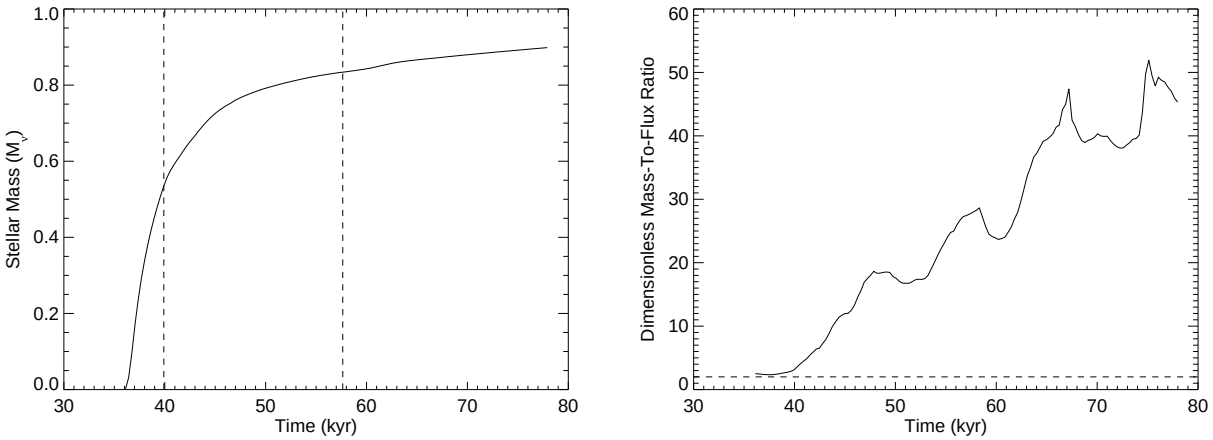

Fig. 3-1.— Left panel: Mass of the protostar (as represented by a sink particle) as a function of time. The dotted vertical lines denote the range of time plotted in Fig. 3-4. Right panel: Dimensionless mass-to-flux ratio within 200 AU of the star, indicating that most of the magnetic flux associated with the stellar mass is left outside of the small region (see text). The initial core mass-to-flux ratio $\lambda_{core} = 2$ is plotted (dashed line) for comparison.

To make sure that the sink particle treatment has indeed decoupled the magnetic flux from the material that enters the stellar object, we plot in the right panel of Fig. 3-1 the dimensionless ratio λ of all mass (including sink) and all magnetic flux within a small radius (200 AU) around the sink particle. The flux is computed on the x-y plane that passes through the star (i.e., the constant $z = z_\star$ plane where $z_\star$ is the stellar position in the $z-$direction); this plane will be referred to as the equatorial

plane of the star or equatorial plane for short hereafter. There is a general trend for λ to increase with time, reaching values as high as 50, which is much higher than the dimensionless mass-to-flux ratio for the core as a whole ($\lambda_{core} = 2$). Clearly, the magnetic flux near the protostar did not increase as fast as the stellar mass, and the vast majority of the flux originally associated with the stellar mass must reside outside the small region. It is natural to ask: where did this flux go?

Decoupling-Enabled Magnetic Structure

It turns out that the decoupled flux is trapped in a strongly magnetized, low-density structure that expands with time. The left panel of Fig. 3-2 shows the structure in a map of column density (along $z-$direction) at a representative time $t = 43$ kyrs (or $\sim 1.45\ t_{ff}$). At this time, the evacuated region has a size of $\sim 1.2 \times 10^{16}$ cm (or about 800 AU). It grows in time, as indicated by the velocity vectors inside the region. The right panel of Fig. 3-2 plots the $z-$component of the magnetic field, B_z, on the equatorial plane of the star. It shows that the hollow region coincides with a region of intense magnetic field, leaving little doubt that the structure has a magnetic origin.

One may be tempted to call the low-density structure a "magnetic bubble". However, as shown in Fig. 3-3, "bubble" does not provide an adequate description of the structure in 3D; the dense feature surrounding the evacuated region in the column density map (Fig. 3-2) turns out to be a ring rather than a shell. The reason is that, in the absence of the decoupled magnetic flux, the collapsing core material would settle preferentially along field lines into a dense, flatten, structure—a "pseudodisk" (Galli & Shu 1993). The left-behind magnetic flux evacuates part of the pseudodisk, creating the structure showing in Fig. 3-3, where a bundle of magnetic field lines is pinched near the equator by a dense ring. We will refer to the structure as the "decoupling-enabled magnetic structure" (DEMS for short hereafter).

The strongest evidence for the DEMS being really driven by the magnetic flux

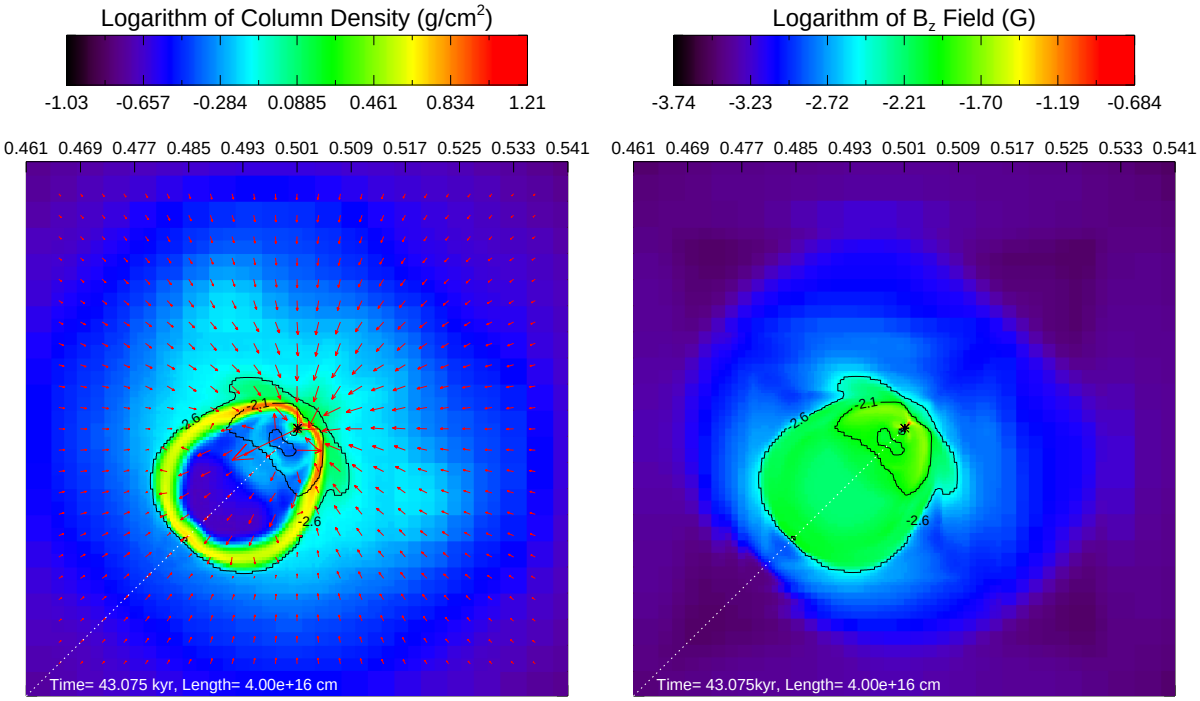

Fig. 3-2.— Left panel: Column density (along $z-$direction) and velocity field (on the equatorial plane) of the inner region of the collapsing core at a representative time $t = 43$ kyrs (or $\sim 1.45\ t_{ff}$), showing an expanding, evacuated region to the lower-left of the star (marked by an asterisk on the map). Superposed on the map are contours of constant B_z (the z-component of the magnetic field) on the equatorial plane. Right panel: Color map of B_z on the equatorial plane, showing that the evacuated region coincides with a region of intense magnetic field. The tick marks above each panel are in units of 5×10^{17} cm (size of the simulation box).

decoupled from the material accreted onto the stellar object comes from Fig. 3-4, where we plot the ratio of the stellar mass $M_\star$ to the magnetic flux in the structure Φ_d. The quantity Φ_d is computed on the equatorial plane of the star. It includes all cells inside a boundary beyond which B_z falls off steeply (see Fig. 3-2). Not surprisingly, the cells are mostly located inside the dense ring. We are able to determine the ratio over only a limited range in time, because the DEMS becomes apparent only after $t \sim 40$ kyrs, and it starts to merge into the background (making an accurate identification of the DEMS difficult) after $t \sim 60$ kyrs. As the stellar mass nearly doubles during the early part of this period (see Fig. 3-1), the mass-to-flux ratio

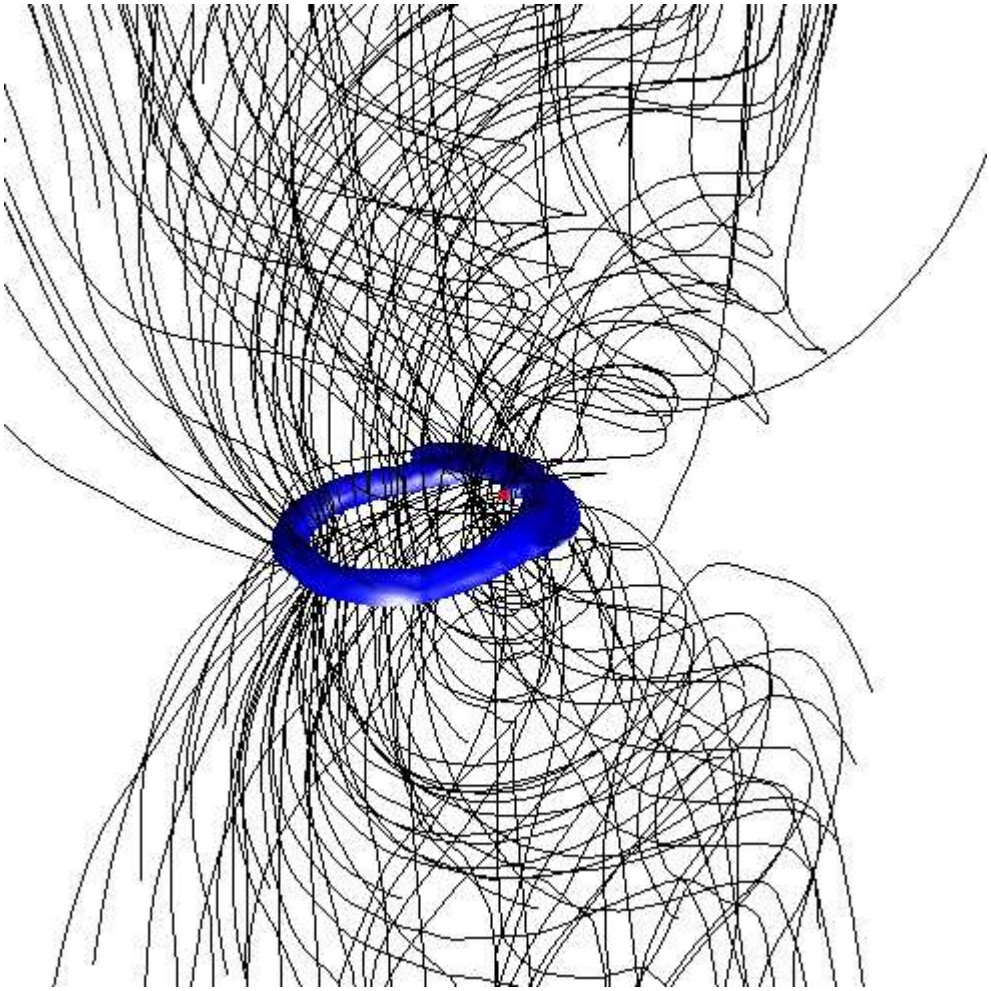

Fig. 3-3.— 3D view of the inner part of the collapsing core, showing the decoupling-enabled magnetic structure (DEMS), where a bundle of twisted magnetic field lines is surrounded at the "waist" by a dense ring. The star is shown as a red dot located near the inner edge of the ring.

remains relatively constant, indicating that Φ_d increases together with $M_\star$. This behavior is consistent with Φ_d being released by $M_\star$. Furthermore, the dimensionless mass-to-flux ratio $\lambda_{\star,d} = 2\pi G^{1/2} M_\star/\Phi_d$ is close to the global value for the initial core, as one would expect if the initial core matter releases its flux on the way to the center. The small deviation from the global value $\lambda_{core} = 2.0$ can come from the fact that local λ in the initial core is not exactly 2, and that the DEMS is identified by eye and is not very precise. Nevertheless, the different pieces of evidence presented in this

subsection leave little doubt that the DEMS is formed by the magnetic flux decoupled from the accreted stellar mass.

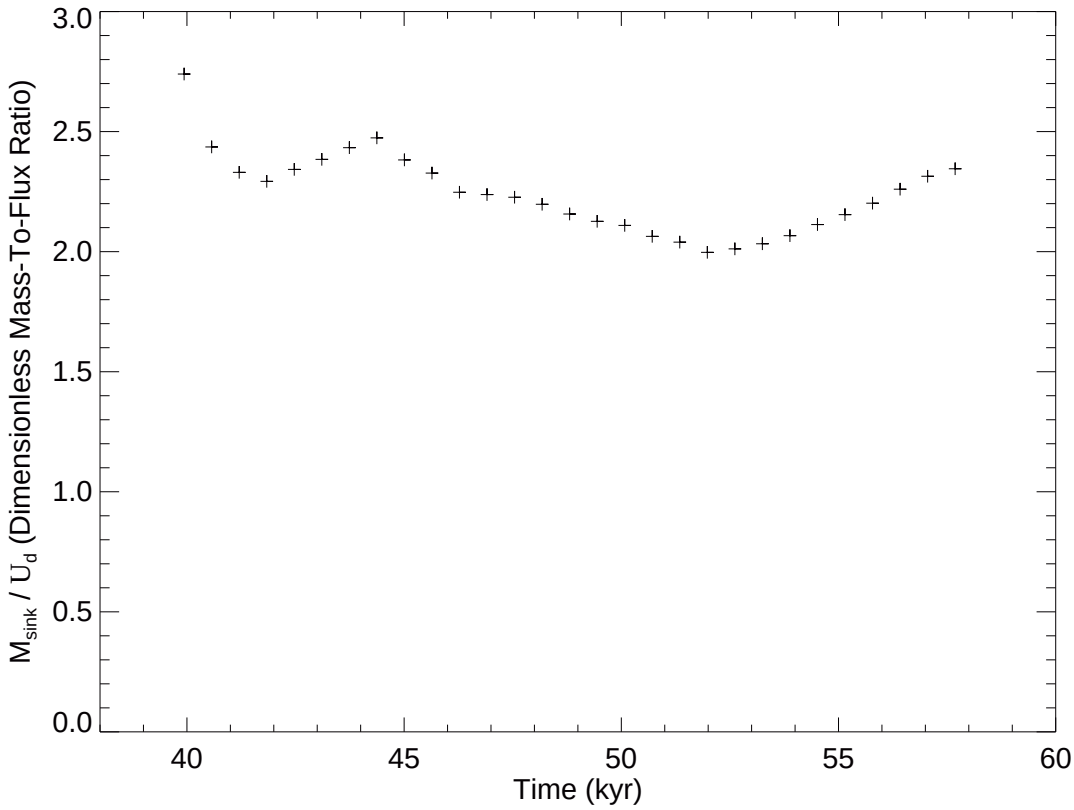

Fig. 3-4.— The dimensionless ratio $\lambda_{\star,d}$ of the stellar mass $M_\star$ to the magnetic flux in the decoupling-enabled magnetic structure (DEMS) Φ_d as a function of time. The closeness of $\lambda_{\star,d}$ to the value $\lambda_{core} = 2$ for the core as a whole indicates that the flux in the DEMS is released by the stellar material.

We have checked that the creation and evolution of the DEMS is insensitive to the details of the sink particle treatment. For example, we have allowed more levels of refinement (7 and 8 instead of 6) before the sink particle creation, with higher values for the effective matter-field decoupling density ρ_{th}. The results are qualitatively similar, although the shape and orientation of the DEMS are somewhat different. We have also varied the critical density ρ_{crit} in the equation of state, and obtained a broadly similar result. These tests support the conclusion that the DEMS is robust.

Its existence also makes physical sense because, as the decoupled flux accumulates near the protostar, the magnetic pressure builds up, which can only be released through expansion. In hindsight, it is hard to imagine any other outcome.

DEMS and Collapse Dynamics

The DEMS modifies the dynamics of core collapse and star formation in several ways. The most obvious is the change to the density distribution and velocity field in the equatorial region where most of the mass accretion occurs. The DEMS produces an evacuated region that expands against the dense, collapsing pseudodisk, as shown in the left panel of Fig. 3-2. There are initially several small, irregular, low-density regions. Only one develops into a full-blown DEMS through runaway expansion. It starts to grow quickly after enough magnetic flux has accumulated in the region that a high magnetic pressure is built up to overwhelm the ram pressure of the collapsing flow. The expansion occurs presumably along the path of least resistance, which happens to lie in the direction towards the lower-left corner in Fig. 3-2; this direction is probably related to the cubic simulation box and Cartesian grid, which break the symmetry in the collapsing flow[1]. As mentioned earlier, by the time $t = 60$ kyrs (or about 2 t_{ff}), the structure grows to a size comparable to the initial core radius, and starts to merge into the background.

To examine the expansion dynamics more quantitatively, we plot in Fig. 3-5 the distributions of the magnetic pressure, the thermal pressure $P_{th} = \rho c_s^2$, and the ram pressure associated with the radial component of the velocity $P_{r,ram} = \rho v_r^2$, in the equatorial plane, along the dotted line shown in the left panel of Fig. 3-2. Note the sharp increase (by a factor of $\sim 10^3$) in the magnetic pressure around $r \sim 10^{16}$ cm, which marks the boundary of the DEMS. Inside the boundary, the magnetic pressure is more or less uniform. It is much higher than the thermal pressure, by a factor

[1]We have experimented with runs where subsonic turbulent velocity fields are imposed on the dense core at the beginning of the simulation. The symmetry-breaking turbulence does not change the DEMS qualitatively.

of $\sim 10^2$, corresponding to a low plasma $\beta \sim 0.01$ (defined as the ratio of plasma pressure to magnetic pressure). The high magnetic pressure is what drives the region to expand. The expansion is slowed down by the ram pressure of the collapsing material outside the strongly magnetized region, which is somewhat smaller than, but comparable to, the magnetic pressure. The spike just outside $r = 10^{16}$ cm on the curve of ram pressure is due to the dense, expanding ring that is prominent in Fig. 3-2. The ring is the collapsing pseudodisk material that has been swept up by the expanding, magnetically dominated region. It has a peak density nearly two orders of magnitude higher than the surrounding medium. The ring is not yet massive enough in our current simulation to become self-gravitating, but we speculate that this might happen under other circumstances; in such cases, the ring may fragment into secondary objects. We will postpone an exploration of this possibility to a future investigation.

A direct consequence of the one-sided expansion of the magnetically dominated region is that accretion onto the central object must proceed in a highly asymmetric fashion. The asymmetric accretion is shown vividly in the left panel of Fig. 3-2, where velocity vectors are plotted in the equatorial plane of the star. While the collapsing flow in the upper-right half of the plane can fall into the star directly, that on the lower-left half is mostly obstructed by the DEMS. Based on the highly asymmetric accretion pattern, one may expect the stellar object to pick up some velocity. We find that the star particle in our simulation does move, but only at a small speed of order 0.1 km/s, too small to be of any dynamical significance. The reason for the slow stellar motion is probably the following: in the absence of any external force, the total linear momentum of the system, which is initially zero, must be conserved. In particular, the collapsing flow on the lower-left side of the star is diverted by the DEMS to flow towards the star along the dense ring. Its momentum may cancel out that of the unobstructed collapsing flow from the other side to a large extent, at least in this particular simulation. Whether the slow stellar motion is true in general

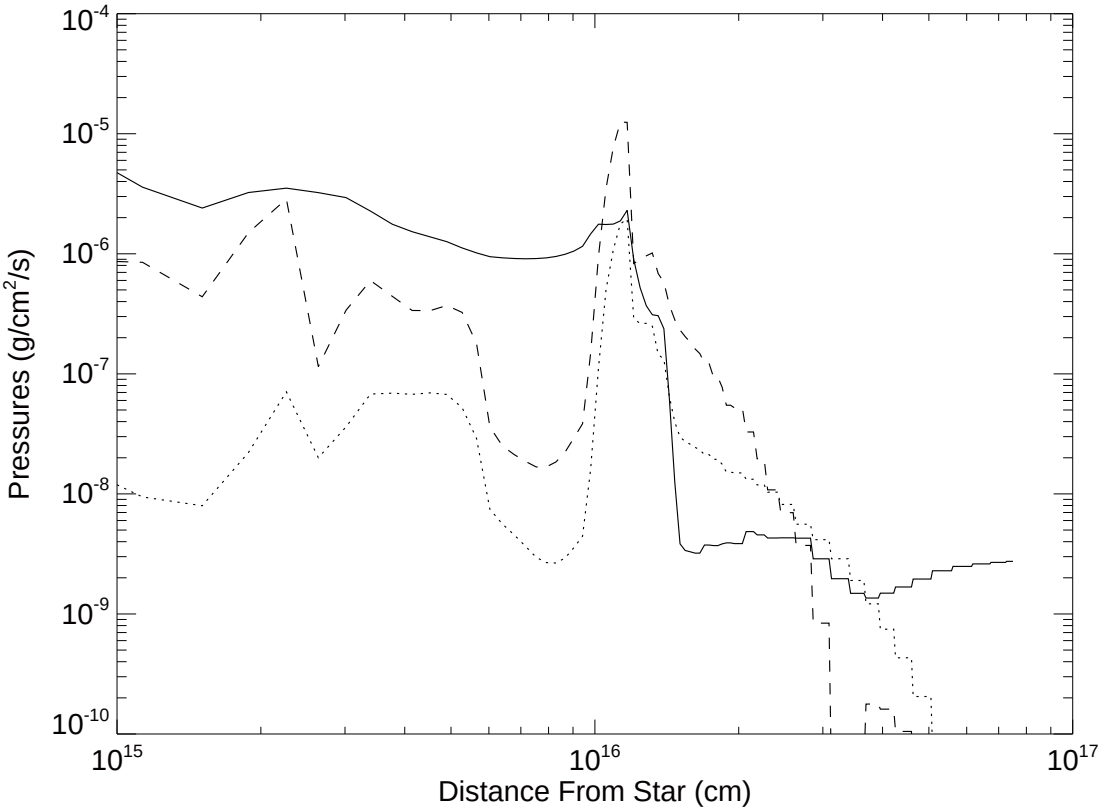

Fig. 3-5.— Comparison of the magnetic (solid line), thermal (dotted) and ram pressure due to radial motion (dashed), in the equatorial plane, along a representative direction (shown as dotted line in the left panel of Fig. 3-2).

remains to be determined.

The diversion of the magnetized collapsing flow around the DEMS creates an interesting feature: the twisting of magnetic field lines, which is clearly visible in Fig. 3-3. The twisting is normally not expected in a non-rotating collapse. However, when the direct path to the star is blocked by the DEMS, a parcel of collapsing flow moves around the structure, twisting the field lines tied to the parcel in the process. Indeed, the magnetic tension associated with the twisted field lines produces an bipolar outflow moving away from the equatorial plane (most visible from the velocity field in the x-z or y-z plane, not shown), similar to the cases where an initial core rotation is present (e.g., Tomisaka 1998). Such an outflow has not been seen in

previous non-rotating collapse calculations.

3.3.2 Rotating Collapse

We have shown that the decoupling-enabled magnetic structure strongly affects the dynamics of non-rotating collapse. Here, we wish to examine its influence on the dynamics of rotating collapse in general and disk formation in particular. For this purpose, we impose on the core an initial solid-body rotation with $\Omega = 4.0 \times 10^{-13}$ s^{-1}, keeping other parameters the same as in the non-rotating collapse discussed in § 3.3.1.

Fig. 3-6 (left panel) shows a snapshot of the rotating collapse at a representative time $t = 47.5$ kyrs (or $\sim 1.6\ t_{ff}$), when the stellar object has accreted $\sim 0.67\,\mathrm{M}_{\odot}$. The overall morphology is broadly similar to that of the non-rotating case shown in Fig. 3-2, with an evacuated DEMS expanding against a collapsing flow. An obvious difference is, of course, rotation. The rotation is not fast enough, however, to stop the collapse centrifugally, even along directions not directly affected by the DEMS. The lack of complete centrifugal support is illustrated in the right panel of Fig. 3-6, where we plot the infall and rotation speeds along a DEMS-free direction (marked in the right panel as a dotted line). The rotation speed remains well below the Keplerian value, except in the region inside a radius of $\sim 8 \times 10^{14}$ cm, where the two become comparable. In this small region, the collapse is slowed down, but not stopped. Its infall speed is $\sim 1.5 - 2$ km/s, much higher than the sound speed (0.2 km/s). The supersonic infall leaves little doubt that a large-scale rotationally supported structure is not formed in this direction, presumably because of strong magnetic braking, which has been shown to be capable of suppressing disk formation in previous ideal MHD simulations (Allen et al. 2003; Mellon & Li 2008; Hennebelle & Fromang 2008; Seifried et al. 2011).

The DEMS makes disk formation even more difficult. The reason is that the DEMS is a rather rigid structure that prevents the rotating material from completing a full orbit around the central star. To be more quantitative, we compare the magnetic

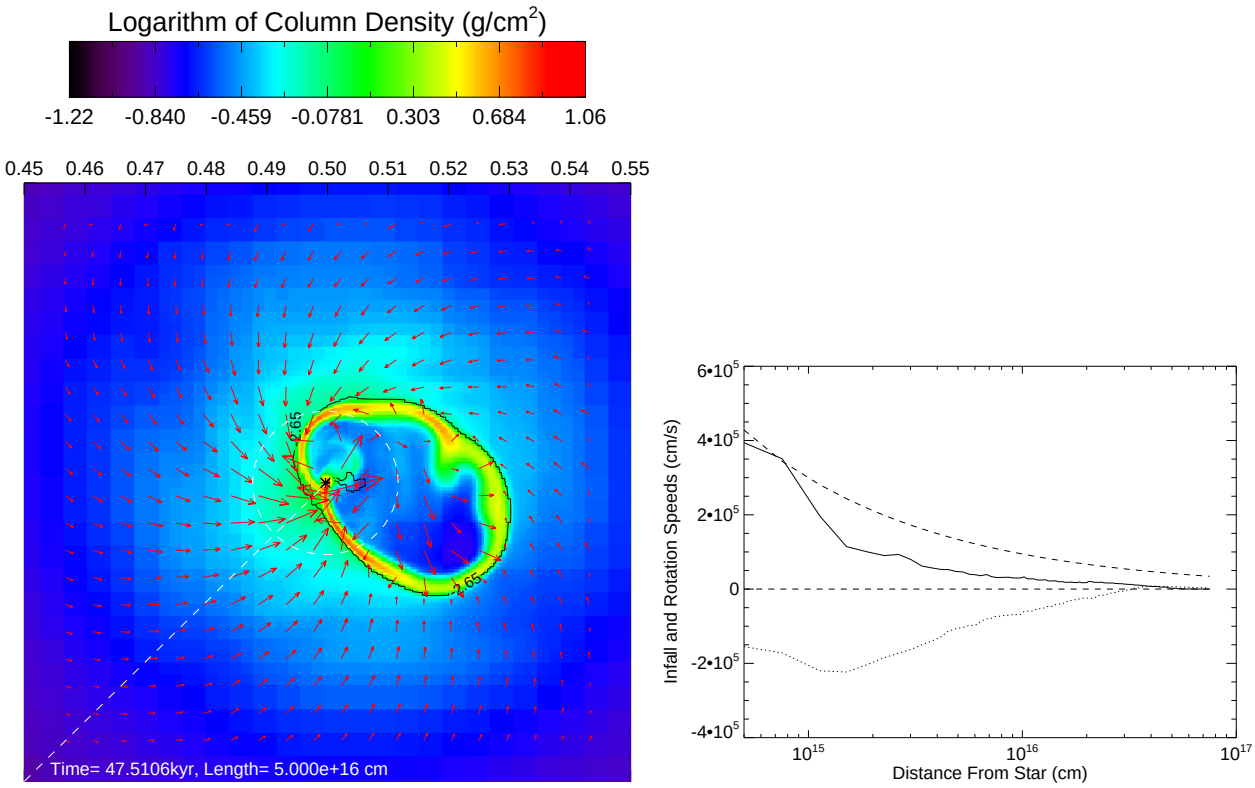

Fig. 3-6.— Left panel: Same as the left panel of Fig. 3-2 but for rotating collapse. Again, an expanding low-density region is clearly visible. Right panel: Infall (dotted line) and rotation (solid) speed on the equatorial plane along the dotted line shown in the left panel. A Keplerian profile is also plotted (dashed) for comparison.

pressure to the ram pressure due to rotation $P_{\phi,ram} = \rho v_\phi^2$ along a circle of 400 AU in radius in the equatorial plane in Fig. 3-7. Clearly, the magnetic pressure inside the DEMS ($\sim 0^\circ - 100^\circ$ and $\sim 290^\circ - 360^\circ$) is higher than the rotational ram pressure outside the DEMS (the two peaks of ram pressure correspond to locations on the dense ring). The DEMS is effectively a magnetic wall that stops the rotating motion of the material that runs into it. This is a new form of magnetic braking that has never been discussed before in core collapse and disk formation.

The rotation has an effect on the shape of the dense ring. Whereas the ring is more or less (mirror) symmetric with respect to a plane in the non-rotating collapse (see the dotted line in Fig. 3-2), it is much less so in the rotating collapse. The reason

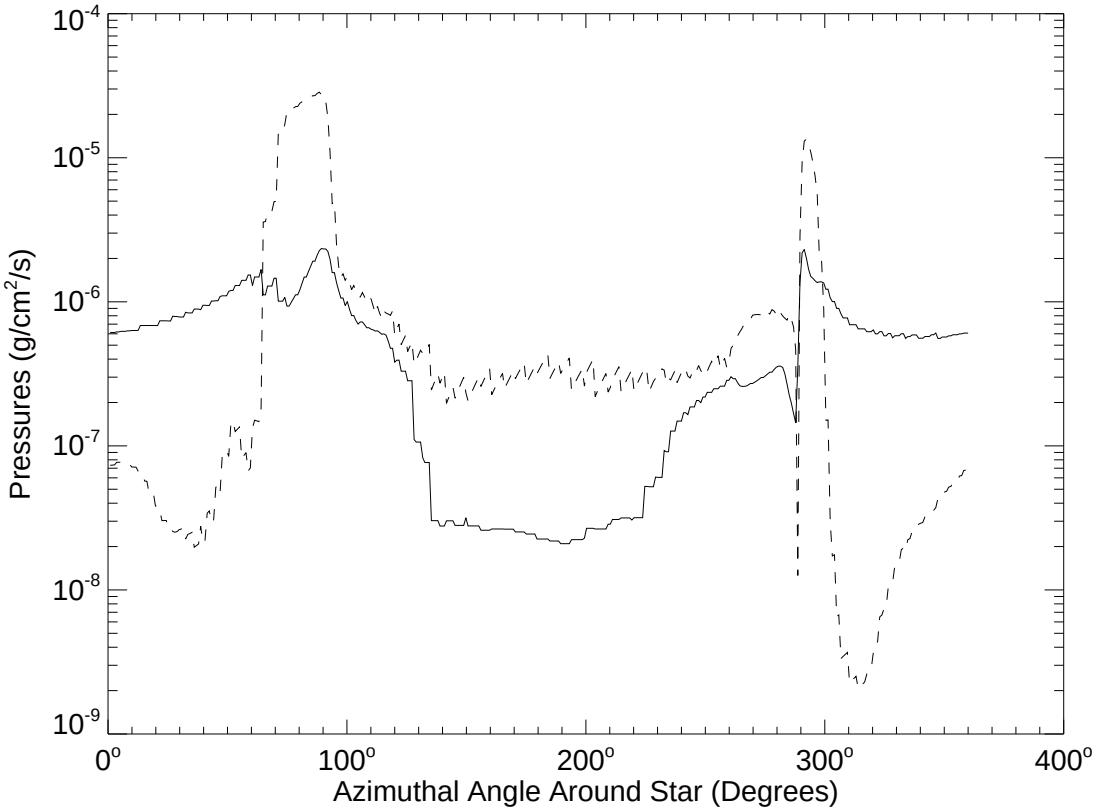

Fig. 3-7.— Comparison of the magnetic pressure (solid line) and the ram pressure due to rotation in the equatorial plane, on a circle of ~ 400 AU in radius (shown in the left panel of Fig. 3-6). The azimuthal angle is measured counterclockwise from the x-axis. The magnetic pressure inside the DEMS ($\sim 0^\circ - 100^\circ$ and $\sim 290^\circ - 360^\circ$) is much higher than the rotational ram pressure outside ($\sim 100^\circ - 290^\circ$), making disk formation difficult.

is that one side of the DEMS expands against the rotating flow, and its expansion is slowed down by rotation (see the lower side of the DEMS in the left panel of Fig. 3-6). The other side expands into a medium that is already rotating away from it to begin with, and its expansion is sped up by rotation. The net result is that the lateral expansion of the DEMS becomes asymmetric in the presence of rotation. The effect is particularly strong at early times, when the rotation speed has yet to be greatly reduced by magnetic braking and the DEMS.

3.4 Discussion and Summary

We find a new feature in the protostellar collapse of magnetized dense cores: an expanding low-density region driven by the magnetic flux decoupled from the material that has accreted onto the star. This decoupling-enabled magnetic structure (DEMS) has implications for both high resolution star formation simulations and for collapse dynamics including disk (and possibly binary) formation.

The DEMS formation is a natural consequence of simulating magnetized star formation using the sink particle formalism. Sink particles are needed to represent the formed stellar objects because such objects are much smaller and much denser than their parental dense cores (e.g., Krumholz et al. 2004). When the matter from a cell is added to a sink particle, the magnetic flux from the cell cannot be added to the sink as well, on both physical and numerical grounds. Physically, the addition of the magnetic flux to the sink particle would make the stellar field strength much higher than observed (which is, of course, the well known "magnetic flux problem"). Numerically, the sink particle cannot hold a large magnetic flux, which would produce a large, unbalanced magnetic force in the host cell of the sink particle. The needed decoupling of the magnetic field from matter during sink particle mass accretion makes the creation of the DEMS unavoidable in an ideal MHD simulation of the protostellar phase of star formation.

The DEMS that we found is conceptually related to the highly magnetized inner region of protostellar collapse in the presence of non-ideal MHD effects, found previously either semi-analytically (in 1D) or through 2D (axisymmetric) simulations. It has been shown that, in the presence of ambipolar diffusion, most of the magnetic flux left behind by the stellar mass is trapped in a strongly magnetized region inside a C-shock (Li & McKee 1996, Ciolek & Königl 1998). The situation is similar in the presence of Ohmic dissipation (Li et al. 2011). In both cases, because of the axisymmetry assumed, the collapsing flow has to cross the strongly magnetized inner

region where the left-over magnetic flux is parked in order to reach the center. As a result, the highly magnetized region is loaded with high-density material (at least near the equatorial plane, see, e.g., Fig. 4 of Li et al. 2011). Strictly speaking, the region is not a (low-density) DEMS, although it does share the same origin as the DEMS: both are driven by the decoupled magnetic flux. Indeed, one may view the case considered in this Chapter as the high-ionization limit of the general non-ideal case in which the ideal MHD approximation breaks down only at the highest densities (and the breakdown is mimicked here by the sub-grid physics associated with sink particle treatment). In this limiting case, a very small region of intense magnetic field is expected to form close to the protostar and be trapped by the ram pressure of the infalling material in 2D. In 3D, we find a completely different behavior: an asymmetrically expanding DEMS. The reason is that, in 3D, the collapsing core material does not have to go *through* the strongly magnetized region to reach the central object; it can simply go around the region. The DEMS in 3D is able to choose a path of least resistance (which may be influenced by grid geometry), breaking the restrictions imposed in strictly axisymmtric simulations.

The DEMS is a new feature never reported before in 3D numerical simulations of star formation (see, however, Seifried et al. 2011, who recently found a similar feature independently). Hennebelle & Fromang (2008) followed the collapse of magnetized cores using an AMR MHD code, but did not mention any structure similar to our DEMS. The reason for the absence of DEMS in their simulations is probably that they did not use any sink particle in their simulations and thus did not address the issue of magnetic decoupling that is needed to resolve the magnetic flux problem. Machida et al. (2010) did use sink particles in their nested grid MHD simulations. They did not find any DEMS-like structure either, because they removed the magnetic flux associated with the mass accreted onto the sink particle by hand, on the assumption that the magnetic flux is destroyed by Ohmic dissipation (see Shu et al. 2006 for the reason why the flux cannot be not destroyed). The flux removal is probably also the

reason why the DEMS was not present in SPH MHD simulations (e.g., Price & Bate 2007; Bürzle et al. 2011). Padoan & Nordlund (2011) carried out global simulations of star formation in turbulent, magnetized clouds using sink particles. They did not find any DEMS around individual stars either, probably because the ordered magnetic field in their simulations is much weaker than in ours. If a dense core has a larger initial mass-to-flux ratio than adopted here, there would be less magnetic flux to decouple from a given stellar mass, and the smaller decoupled flux would drive a less prominent DEMS.

Although we believe that the DEMS is robust in the limit considered in this Chapter where the matter and magnetic field are well coupled except at the highest densities, it remains unclear how it will be affected by non-ideal MHD effects, including ambipolar diffusion, Ohmic dissipation and Hall effect, all of which can play a role in the magnetic field evolution during core collapse and disk formation, at least in 2D. The logic next step is to carry out 3D AMR MHD simulations that include both sink particles and non-ideal MHD effects. It would be interesting to determine the extent to which the collapsing flow reaches the star either by crossing field lines in a strongly magnetized region through non-ideal MHD effects (as in the current 2D simulations, such as Li et al. (2011)) or by going around the strongly magnetized region, as we find in this Chapter. Another effect is the turbulence-enhanced reconnections (e.g., Kowal et al. 2009), which may reduce the amount of the magnetic flux dragged close to the central object and weaken the DEMS.

To summarize, we have carried out simulations of magnetized core collapse and star formation using a MHD version of the ENZO AMR code. A sink particle treatment is used to decouple the magnetic flux from the material that enters the star, which must happen to resolve the well-known "magnetic flux problem" in star formation. We find that the decoupled flux creates a low-density high magnetic pressure region that expands anisotropically away from the protostar. This decoupling-enabled magnetic structure has profound effects on the dynamics of core collapse, making

the protostellar accretion flow highly asymmetric and the formation of a rotationally supported disk more difficult. It is a generic feature of star formation in strongly magnetized cloud cores that should be included in future simulations, especially those using sink particle treatment.

Chapter 4

Orbital and Mass Ratio Evolution of Protobinaries Driven by Magnetic Braking

This chapter is based on the published paper of Zhao & Li (2013, ApJ, 763, 7).

4.1 Introduction

The majority of the Galactic field stars reside in multiple systems (Duquennoy & Mayor 1991; Fischer & Marcy 1992; Mason et al. 1998; Shatsky & Tokovinin 2002; Goodwin & Kroupa 2005; Raghavan et al. 2010; Janson et al. 2012); most of those systems ($\sim$ 75%) are binaries (Duquennoy & Mayor 1991; Tokovinin & Smekhov 2002). The multiplicity of young stellar objects is even higher (Reipurth & Zinnecker 1993; Mathieu et al. 2000; Duchêne et al. 2004; Duchêne et al. 2007), indicating that the formation of multiple systems, especially binaries, is a major, perhaps the dominant, mode of star formation.

How binaries form and evolve remains uncertain. This is particularly true for the earliest, Class 0, phase, when the stellar seeds are still deeply embedded inside a massive envelope. Although millimeter interferometric observations such as Looney et al. (2000) have uncovered some Class 0 binaries, their number is still small, and the distribution of orbital separation of such protobinaries is not well constrained. Maury et al. (2010) surveyed 5 Class 0 sources with PdBI at sub-arcsecond resolution, and found a surprising result: only one of the sources has a potential protostellar companion, and the companion is $\sim 1,900$ AU away from the primary. Combining their sample with that of Looney et al. (2000), Maury et al. (2010) found that none of the 14 Class 0 sources in the combined sample has a companion with separation between $\sim 150 - 550$ AU, which is inconsistent with the binary fraction of $\sim$ 18% for Class I sources in the same separation range (Connelley et al. 2008). A similar difference was found in the CARMA survey of 6 Class 0 and 3 Class I sources in the Serpens molecular cloud (Enoch et al. 2011). None of the Class 0 objects has any detectable protostellar companion closer than 2,000 AU (down to the resolution limit $\sim$ 250 AU), whereas one Class I object has a companion at a projected distance of $\sim$ 870 AU. Although the statistical significance of the difference is still relatively low, it brings into sharp focus the possibility that the distribution of orbital separation of

protobinaries may differ significantly from that of their more mature counterparts. In other words, binaries may migrate substantially from their birth locations, a situation somewhat analogous to that inferred for hot Jupiters, although it is unclear whether protobinaries would migrate inward or outward to fill the apparent gap between $\sim 150 - 550$ AU. The direction (inward vs outward) of protobinary orbital migration should be better constrained observationally with large surveys of deeply embedded sources using ALMA and JVLA.

In this Chapter, we will focus on one possible mechanism for moving the protobinaries away from their birth locations: magnetic braking. It may seem counter-intuitive that magnetic fields can change the binary orbit, because the magnetic forces do not act on the stars directly. However, the orbits of protobinaries are determined mainly by the angular momentum of the material to be accreted, which can be strongly affected, perhaps even controlled, by the magnetic field, through magnetic braking. The main goal of this investigation is to quantify the extent to which the protobinary orbit is modified by a magnetic field of the observed strength.

The strength of magnetic fields in star formation is usually measured by the dimensionless mass-to-flux ratio λ. It is the mass of a region divided by the magnetic flux threading the region in units of the critical value $(2\pi G^{1/2})^{-1}$ (Nakano & Nakamura 1978). For a sample of dense cores in the nearby dark clouds, Troland & Crutcher (2008) inferred a mean value for $\lambda_{los} \sim 4.8$, based on the field strength and column density along the line-of-sight. Geometric corrections for projection effects should reduce this value by a factor of 2-3, yielding an intrinsic value of λ of a few typically. Such a magnetic field is generally not strong enough to prevent the dense core from gravitational collapse and star formation. It is, however, strong enough to affect the angular momentum evolution of the collapsing core in general and binary formation in particular.

There have been several studies of the magnetic effects on binary formation (e.g., Price & Bate 2007; Hennebelle & Teyssier 2008; Machida et al. 2010). These studies

focused primarily on the classical mode of binary formation inside an isolated rotating core, through core fragmentation induced by an $m = 2$ density perturbation (e.g., Boss & Bodenheimer 1979, see Kratter 2011 for a recent review and Chapter 1 for an overview of different mechanisms of binary formation). A general conclusion is that the fragmentation can be suppressed by a rather weak magnetic field if the core is only weakly perturbed. For example, Hennebelle & Teyssier 2008 found that, for a density perturbation of 10%, the fragmentation is suppressed by a magnetic field corresponding to $\lambda = 20$ (see their Fig. 3), much weaker than the observationally inferred field. In dense cores that are magnetized to a more realistic level (with $\lambda \sim$ a few), fragmentation can still occur, although a large amplitude perturbation is needed (Price & Bate 2007; Hennebelle & Teyssier 2008). A limitation of the existing MHD calculations is that they are confined mostly to the pre-stellar phase of core collapse and fragmentation leading up to the formation of two binary seeds. How the binary seeds evolve during the subsequent protostellar mass accretion phase in the presence of a dynamically important magnetic field remains little explored. It is the focus of our investigation.

Our investigation of the magnetic effects on protobinary evolution was carried out using the MHD version of the ENZO AMR hydro code described in Chapter 2 that includes a sink particle treatment (Bryan & Norman 1997; O'Shea et al. 2004; Wang & Abel 2009; Wang et al. 2010). In § 4.2, we discuss the setup for the initial binary seeds and the rotating magnetized protobinary envelope to be accreted by the seeds, as well as the numerical code used. In § 4.3, we present numerical results for the evolution of initially equal-mass binary seeds. We find that a magnetic field of the observed strength can shrink the protostellar orbit by more than an order of magnitude compared to the non-magnetic case. It also greatly changes the dynamics and morphology of the protostellar accretion flow near the binary. For initially unequal mass binary seeds, the issue of mass ratio evolution becomes important. In § 4.4, we follow the the evolution of unequal-mass protobinaries accreting from envelopes

magnetized to different levels. We find that the well-known tendency towards equal mass in the non-magnetic case due to preferential mass accretion onto the secondary is weakened or even suppressed by magnetic braking. We summarize the main results and put them in context in § 4.5.

4.2 Problem Setup

As mentioned in the introduction, the focus of our investigation is on the protostellar accretion phase of binary formation, where the magnetic effects are least explored. We will therefore skip the pre-stellar phase of core evolution leading up to the production of a pair of binary seeds, and assume that, at the beginning of our calculations, the seeds are already formed and are ready to accrete from a rotating, magnetized envelope. The setup is similar in spirit to the influential work of Bate & Bonnell (1997) and Bate (2000), who studied the effects on binary properties of mass accretion from an unmagnetized envelope (see also Artymowicz 1983). We postpone a treatment of both the pre-stellar and protostellar phases of binary formation to a later chapter (see Chapter 6). In what follows, we describe the initial conditions for the envelope and binary seeds as well as the numerical code used for following the envelope collapse and protobinary accretion.

Although protostellar envelopes are often observed to be irregular and filamentary (e.g., Tobin et al. 2010), it is instructive to model them simply, so that the basic effects can be illustrated as cleanly as possible. Since the formation and evolution of binaries involve complex dynamics that are challenging to simulate and interpret, it is useful to set up the calculations in such a way that the numerical results can be checked against analytic expectations. One way to achieve this is to start with a self-similar initial configuration for the envelope, with an r^{-2} density distribution given by (Shu 1977)

$$\rho(r) = \frac{Ac_s^2}{4\pi G r^2}, \tag{4.1}$$

where c_s is the isothermal sound speed, and A is an over-density parameter. The collapse of such an initial configuration is expected to remain self-similar (Shu 1977), and the self-similarity has proven to provide a powerful check on the numerically obtained solutions (see, e.g., Allen et al. 2003; Mellon & Li 2008; 2009; Kratter et al. 2010; and discussion in § 4.3).

We choose an over-density parameter $A = 4$ (corresponding to a ratio of thermal to gravitational energy of $\alpha = 3/(2A) = 0.375$), so that the initial configuration is denser than the famous equilibrium singular isothermal sphere by a factor of 2. The mass enclosed within any radius r can be integrated as,

$$M(r) = \frac{Ac_s^2}{G} r. \tag{4.2}$$

For an adopted core radius $R = 10^{17}$ cm and isothermal sound speed $c_s = 0.2$ km/s (corresponding to a temperature of ~ 10 K), the above equation yields a total core mass $M_{tot} = 1.2\,\mathrm{M}_\odot$ and an average free-fall time $t_{ff} \approx 88$ kyr.

We generalize the isothermal configuration to include both rotation and magnetic fields. To preserve the self-similarity, the rotation speed cannot depend on radius but can have an angular dependence (Allen et al. 2003). A convenient choice is $v_\phi = v_0 \sin\theta$ (where θ is the polar angle measured from the rotation axis), which ensures that the angular speed is finite on the axis. We pick $v_0 = c_s$, in order to have as large a rotation speed as possible, so that the binary can be well resolved, especially for strongly magnetized cases where the binary separation is reduced by a large factor compared to the non-magnetic case; even faster, supersonic, rotation may produce undesirable shocks. The adopted rotation profile corresponds to a ratio of rotational to gravitational energy $\beta = (v_0/c_s)^2/(3A) \approx 0.083$, somewhat higher than used in other works (e.g., Machida et al. 2010). Nonetheless, it is still within the range inferred by Goodman et al. (1993) from NH_3 observations of dense cores.

We choose an initially uni-directional magnetic field along the rotation axis (or

the z-axis in the simulations), with the field strength decreasing away from the axis as $1/\varpi$ (where ϖ is the cylindrical radius), such that the mass-to-flux ratio is constant spatially. To avoid singularity at the origin, we soften the profile to $1/(\varpi + r_h)$, so that

$$B_z(\varpi) = \frac{Ac_s^2}{\sqrt{G}\lambda}\frac{1}{\varpi + r_h}, \tag{4.3}$$

where λ in the denominator is the dimensionless mass-to-flux ratio of the envelope in units of the critical value $(2\pi G^{1/2})^{-1}$, and the parameter r_h is defined below. Even though dense cores typically have λ of a few (see discussion in § 4.1), we will consider a much wider range of λ =2, 4, 8, 16 and 32, as well as the non-magnetic case ($\lambda = \infty$), so as to capture any trend that may exist in the protobinary properties as the field strength increases gradually.

To study the protobinary evolution, we follow Bate & Bonnell (1997) and Bate (2000) and insert two equal-mass "seeds" near the center of the protostellar envelope at the beginning of the calculation; non-equal mass binaries will be treated separately in § 4.4. We assume that each of the binary seeds has a small initial mass of $0.05\,\mathrm{M}_\odot$. To determine the initial binary separation, we assume that the binary seeds get both their masses and orbital angular momentum from a sphere of radius $r_h = 8.30 \times 10^{15}$ cm in the initial envelope that contains $0.1\,\mathrm{M}_\odot$. In other words, we assign both the mass and angular momentum inside r_h to the binary seeds. The initial orbital angular momentum is thus

$$L_b = L(r_h) = \int_0^{r_h}\int_0^{\pi}\int_0^{2\pi} \rho v_0 \sin\theta \varpi r^2 \sin\theta \, dr d\theta d\phi = \frac{Ac_s^2 v_0}{3G} r_h^2, \tag{4.4}$$

which, for circular orbits, yields an initial binary separation of

$$a = \frac{16A^2 c_s^4 v_0^2 r_h^4}{9(GM_b)^3} = 3.687 \times 10^{15}\ \mathrm{cm} \approx 246\ \mathrm{AU}, \tag{4.5}$$

where $M_b = 0.1\ \mathrm{M}_\odot$ is the total mass of the binary.

We carry out simulations with periodic boundary conditions inside a box of length 5×10^{17} cm on each side, which is significantly larger than the protobinary envelope (of radius 10^{17} cm). The region outside the envelope is filled with a uniform isothermal medium of the same density (and temperature) as that at the outer boundary of the envelope ($\rho_a \approx 1.91\times10^{-19}$ g cm^{-3}), so that the pressures are initially balanced across the boundary. To speed up computation, we adopt a relatively coarse base grid of 64^3, but allow for 8 levels of refinement, with a smallest cell size of about 2.0 AU.

As usual, we adopt a barotropic equation of state (EOS) that mimics the isothermal EOS at low densities and adiabatic EOS at high densities:

$$P(\rho) = \rho c_s^2 \left[1 + \left(\frac{\rho}{\rho_{crit}}\right)^{2/3}\right], \tag{4.6}$$

with a critical density $\rho_{crit} = 10^{-13}$ g cm^{-3} for the transition between the two regimes.

We treat the binary stars as sink particles. The sink particle treatment is described in detail in Wang et al. 2010. Briefly, each particle accretes according to a modified Bondi-Hoyle formula (see Ruffert 1994). New sink particles are created at the center of those over-dense cells that violate the Jeans criterion at the highest refinement level, i.e. when $\rho_{cell} > \rho_J = \frac{\pi}{G}(\frac{c_s}{N\Delta x})^2 = 7.90 \times 10^{-14} g \cdot cm^{-3}$, where we have used a Truelove's (Truelove et al. 1997) safety number $N = 16$ and a finest cell size $\Delta x = 3.05 \times 10^{13}$ cm. Newly created sink particles are subject to merging, which is controlled by two parameters: the merging mass $M_{merg} = 0.01\,\mathrm{M}_\odot$ and merging distance $l_{merg} = 5 \times 10^{14}$ cm (for details, see Wang et al. 2010). These values are chosen to eliminate artificial particles and to maximize computation efficiency. Our main results are insensitive to these parameters as long as they are reasonably small.

We have tested the sink particle accretion algorithm against known semi-analytic solutions of the collapse of (non-magnetic) singular isothermal sphere (Shu 1977) and found good agreement. For example, the collapse of our chosen initial configuration (Eq. [5.1] with $A = 4$) yields, after some initial adjustment, a constant mass accretion

rate of 1.06×10^{-5} $M_\odot$ yr^{-1}, which matches Shu's result almost exactly (see Chapter 2 for details).

In a magnetized medium, we let the sink particle accrete only the mass but not the magnetic field; the field is left behind. This treatment is a crude representation of the decoupling of the magnetic field from the matter expected at high densities (Nakano et al. 2002; see discussion in Zhao et al. 2011).

4.3 Magnetic Braking and Protobinary Orbital Evolution

Before discussing detailed quantitative results, we first describe the qualitative effects of the magnetic field on the (initially equal-mass) protobinary orbit by contrasting the two extreme cases: the case without a magnetic field (the HD or hydro case hereafter), and the strongest field case ($\lambda = 2$, which is consistent with available Zeeman measurements, see Troland & Crutcher 2008). Both simulations reached a rather late time (t greater than about 80 kyr, comparable to the free-fall time at the average density), when the binary seeds have finished many orbits around each other. In Fig. 4-1, we show the snapshots of the two cases near the middle point of the simulation, at $t \approx 39$ kyr. They look strikingly different. In the HD case, there are two well separated stars, each surrounded by a circumstellar disk. The disks are surrounded by a well-defined circumbinary structure, with two prominent spiral arms embedded in it. The circumstellar disks and circumbinary structure are similar to those found in previous non-magnetic calculations, such as Bate (2000) and Hanawa et al. (2010). They are the result of the conservation of angular momentum in the rapid collapsing region of the envelope, and redistribution of angular momentum close to the binary through gravitational torques.

These well-known features are completely absent in the strongly magnetized $\lambda = 2$ case. They are replaced by two irregular lobes, which were studied in detail in Zhao et

al. (2011) (see also Chapter 3); they are the so-called "magnetic decoupling-enabled structures" (or DEMS for short) produced by the magnetic flux decoupled from the matter that enters the stars (sink particles). The DEMS are magnetically dominated, low-density, expanding regions. They surround the protobinary, whose separation is much smaller than that of the HD case (see Fig. 4-1). Clearly, the magnetic field has greatly modified not only the circumstellar and circumbinary structures, but also the binary orbit. In the following subsections, we will discuss these modifications more quantitatively.

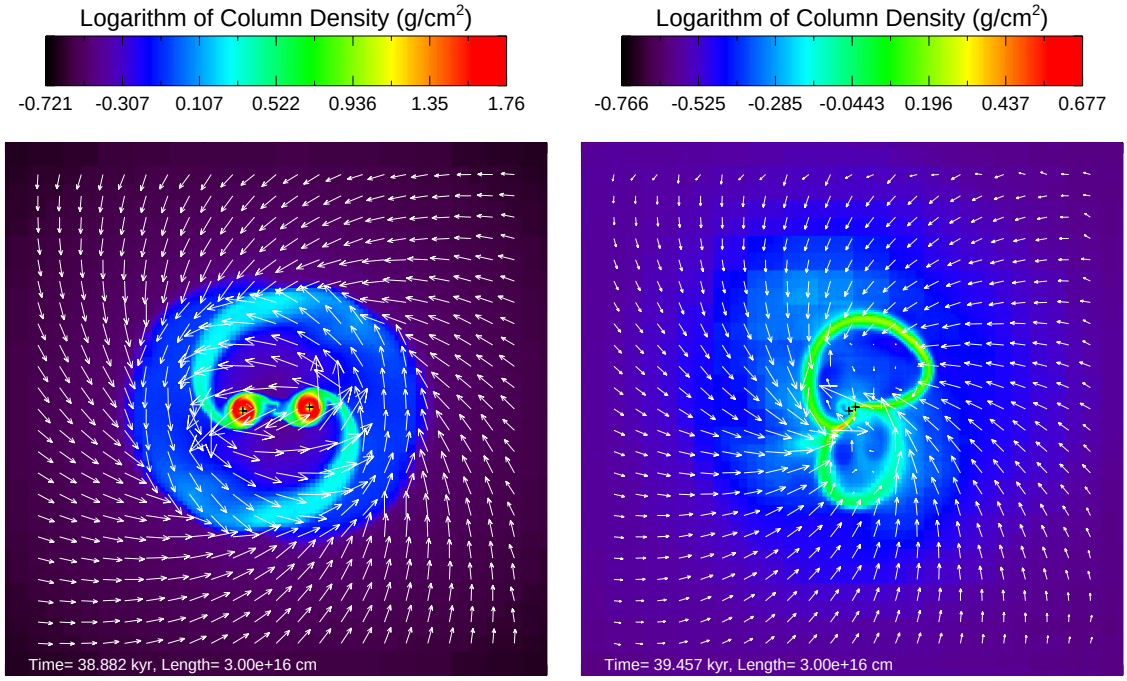

Fig. 4-1.— Distribution of the logarithm of the column density Σ (in $g \cdot cm^{-2}$) along z-direction and velocity field on the equatorial plane. Both the HD (left panel) and $\lambda = 2$ (right panel) case are at $t \approx 39$ kyr. The well-defined circumstellar and circumbinary disks in the former are replaced by two magnetically dominated lobes in the latter. The binary stars are marked by crosses.

4.3.1 Binary Separation and Angular Momentum-Mass Relation

Hydro Case: Checking against Expectations

We begin our quantitative discussion with binary separation. It is shown as a function of time in Fig. 4-2 for all initially equal-mass simulations. The evolution of the binary separation is particularly interesting in the HD case. It decreases initially for about 20 kyr, before increasing almost linearly with time[1]. The linear increase is a natural consequence of the initial protostellar envelope configuration chosen, which is self-similar over a range of radii (excluding the regions close to the center and the outer edge). The configuration is expected to collapse self-similarly, with the binary separation increasing linearly with time (for the same reason that the size of the expansion wave in the well-known inside out collapse of a singular isothermal sphere increases linear with time; Shu 1977), after some initial adjustment. The decrease in binary separation during the initial adjustment comes about because we have put all of the angular momentum of the material inside a small sphere into the orbit of the initial binary seeds. This leads to an overestimate of the initial binary orbital angular momentum (and thus the separation) because a fraction of the angular momentum should be left behind in the circumstellar disks and circumbinary structure. We have experimented with binary seeds formed out of a smaller sphere that have smaller initial masses and separation. They exhibits a similar linear growth of separation with time after a shorter adjustment period. In other words, the protobinary reaches the expected self-similar state more quickly. The agreement of the numerical result with expectations gives us confidence that the ENZO-based AMR code can treat the protobinary evolution problem properly.

Another check on the numerical solution comes from the expected scaling between

[1]The wiggles on the curve is due to small orbital eccentricity (of order 10% or less) excited during the protobinary evolution. We will postpone a detailed study of the magnetic effect on eccentricity to a future investigation.

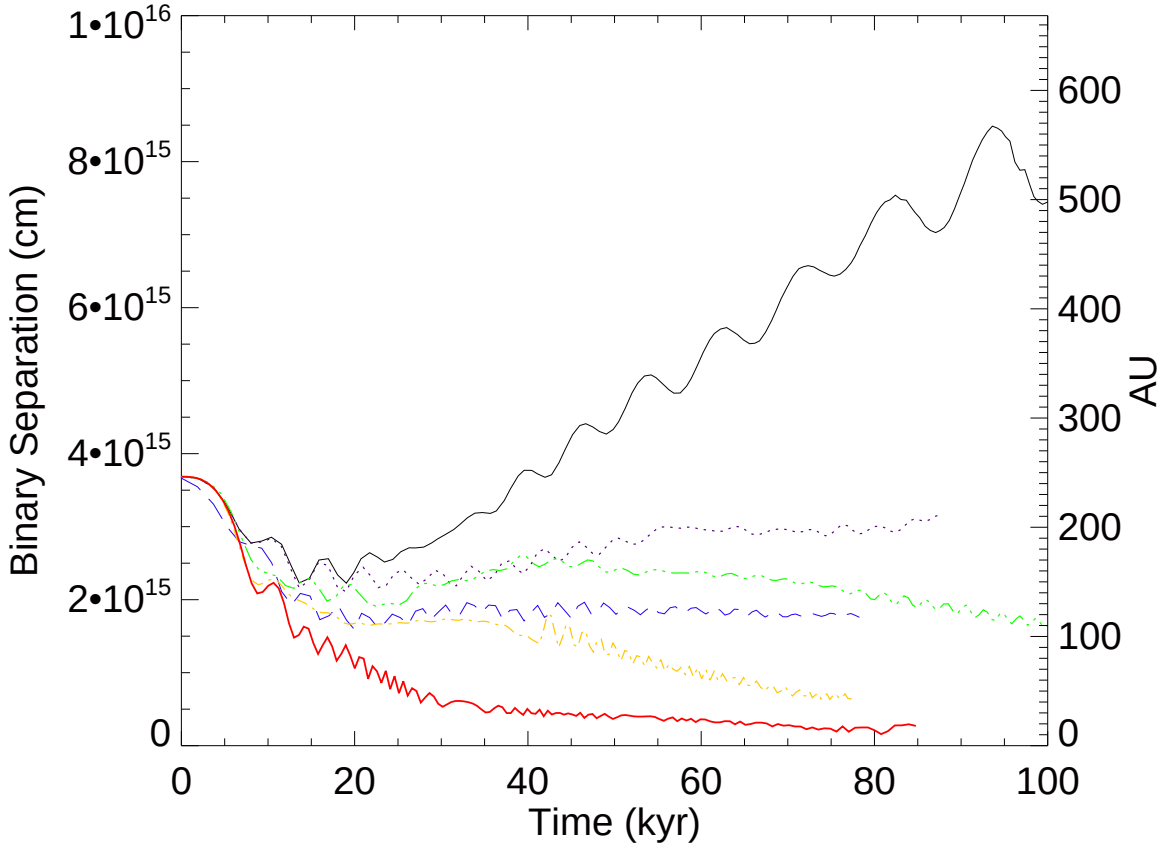

Fig. 4-2.— Evolution of binary separation with time for HD (black solid), $\lambda = 32$ (purple dotted), $\lambda = 16$ (blue long-dashed), $\lambda = 8$ (green dash-dot-dot-dotted), $\lambda = 4$ (yellow dash-dotted), and $\lambda = 2$ (red thick solid) cases. Note the large difference between the HD and the realistically magnetized ($\lambda = 2$ and perhaps 4) cases.

the orbital angular momentum and total mass of the protobinary. The scaling can be obtained as follows. We assume that the gas in our singular isothermal envelope accretes shell by shell onto the binary. The total mass $M(r)$ and total angular momentum $L(r)$ for a sphere of radius r are given, respectively, by Eq. (4.2) and

$$L(r) = \frac{Ac_s^2 v_0}{3G} r^2. \tag{4.7}$$

If all of the mass and angular momentum of the material within the sphere are accreted

onto the binary, then the orbital angular momentum L_b and binary mass M_b must be related through

$$L_b(M_b) = \frac{2Gv_0}{3Ac_s^2} M_b^2. \tag{4.8}$$

This relation is shown as the dashed line (scaled down by a factor of ~ 1.5) in Fig. 4-3, together with the angular momentum-mass (or L_b-M_b) relations obtained in all of our simulations. Again, the HD case is particularly noteworthy. Its $L_b - M_b$ relation closely matches the analytical prediction from eq. (4.8), except for a correction factor of ~ 1.5. The correction is to be expected because the mass and orbital angular momentum of the protobinary at any given time does not come from a region of perfectly spherical shape (assumed in deriving the above equation). More slowly rotating material near the rotation axis can collapse more quickly onto the binary than that near the equator, lowering the actual angular momentum of the binary relative to its mass. In any case, the broad agreement between the numerical result on the L_b-M_b relation and the analytical expectation lends further credence to the correctness of the hydro simulation.

Magnetic Effect on Protobinary Orbit

Fig. 4-2 shows a general trend that the binary separation decreases with increasing magnetic field strength. The difference is especially striking at late times, when the separation increases with time for the HD case but stays roughly constant or decreases for the magnetized cases. By the time $t \approx 80$ kyr, the protobinary separation in the HD case reaches ~ 500 AU, which is much larger than that in the $\lambda = 4$ (~ 50 AU) and $\lambda = 2$ (~ 10 AU) case. There is little doubt that a realistic magnetic field (corresponding to a dimensionless mass-to-flux ratio of a few, see Troland & Crutcher 2008 and discussion in § 4.1) can shrink the protobinary orbit by a large factor.

The reduction in binary separation is related to a decrease in the orbital angular momentum of the system. This is shown explicitly in Fig. 4-3. There is a general trend

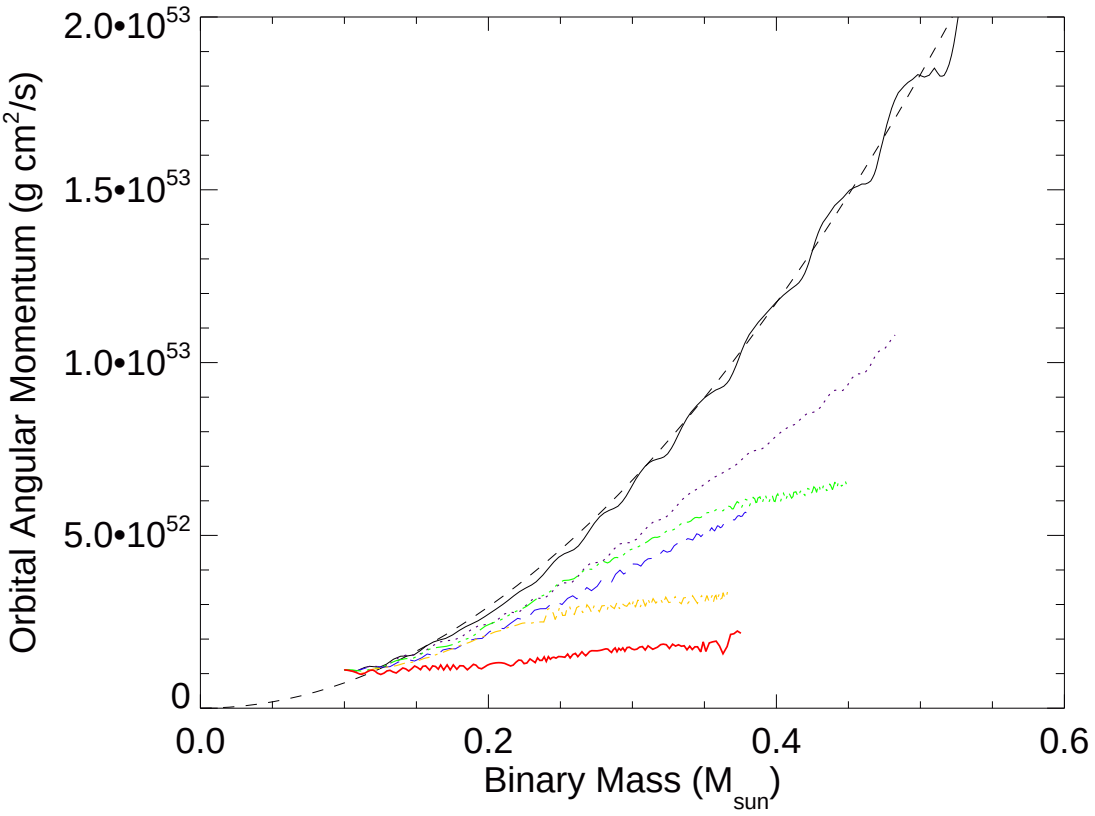

Fig. 4-3.— The relation between the orbital angular momentum and total mass of the protobinary. The dash line is the the analytical prediction from Eq. 4.8 (reduced by a correction factor of ~ 1.5). The different curves are: HD (black solid), $\lambda = 32$ (purple dotted), $\lambda = 16$ (blue long-dashed), $\lambda = 8$ (green dash-dot-dot-dotted), $\lambda = 4$ (yellow dash-dotted), and $\lambda = 2$ (red thick solid).

for the orbital angular momentum to decrease with increasing magnetic field strength. When the mass of the stellar seeds quadruples from 0.1 to $\sim$0.4 $M_\odot$, the orbit angular momentum in the HD case increases by more than an order of magnitude, whereas that in the strongly magnetized $\lambda = 2$ case increases by merely a factor of 2. In the latter case, there is a large amount of mass added to the protobinary but relatively little angular momentum. Since the binary separation a is sensitive to the orbital angular momentum L_b (i.e., $a \propto L_b^2$ for a fixed binary mass M_b), even a relatively modest change in the angular momentum would lead to a significant change in the

separation.

We conclude from Figs. 4-3 and 4-2 that the main magnetic effect on the protobinary evolution is to reduce its orbital angular momentum compared to the non-magnetic case, which in turn leads to a tighter orbit. This result may appear puzzling at the first sight, because the magnetic forces do not act directly on the binary seeds. However, they do act on the material to be accreted by the seeds. By changing the angular momentum of such material, the magnetic field can greatly affect, perhaps even control, the orbital evolution of the protobinary. In the next subsection, we explore in some detail the mechanism through which the magnetic field shrinks the protobinary orbit.

4.3.2 Magnetic Braking and Angular Momentum Removal from Protobinary Accretion Flow

It is well-known that magnetic fields interact strongly with fluid rotation, through magnetic braking. If the infalling material has a large fraction of its angular momentum removed prior to its arrival at the binary seeds, it would add mass but relatively little angular momentum to the protobinary system. As a result, the binary separation would increase less rapidly with time compared to the hydro case; it may even decrease with time if the magnetic braking is strong enough.

The presence of magnetic braking can be seen directly from Fig. 4-4, where we plot the field lines at the representative time $t \approx 39$ kyr for the $\lambda = 2$ case. The initially straight field lines are twisted by the fluid rotation into a helical shape, especially in the polar regions. The magnetic tension force associated with the twist acts back on the fluid, braking its rotation.

To quantify the strength of the magnetic braking, let us consider a finite volume V with surface S. Inside this volume, the total magnetic torque relative to the origin

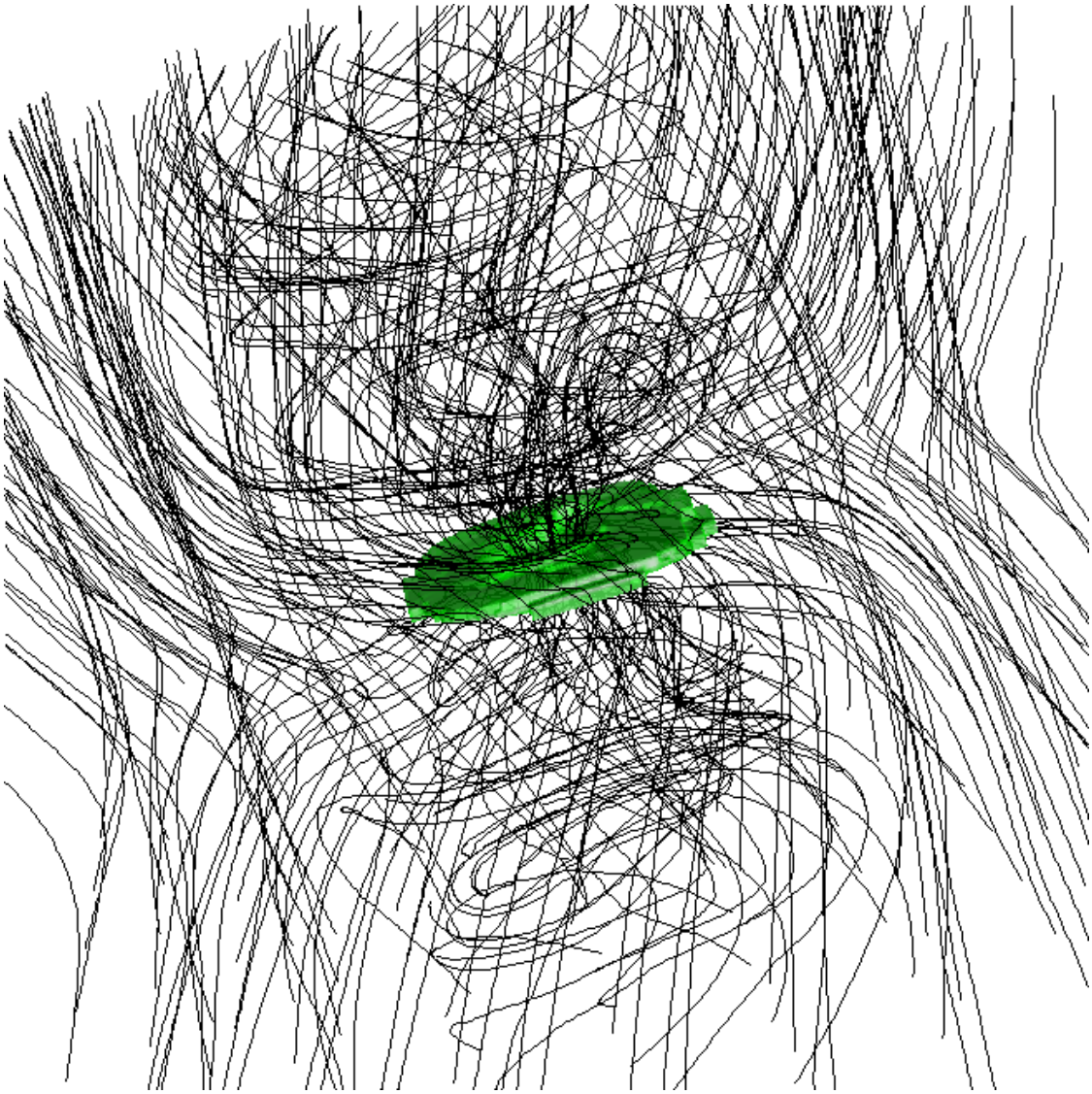

Fig. 4-4.— 3D view of the magnetic field lines and an iso-density surface in the inner part of the protobinary accretion flow at the representative time $t \approx 39$ kyr, showing the field twisting that is the smoking gun of magnetic braking. The plotted region has a dimension of 5×10^{15} cm.

(from which a radius vector $\mathbf{r}$ is defined) is

$$\mathbf{N}_m = \frac{1}{4\pi} \int [\mathbf{r} \times ((\nabla \times \mathbf{B}) \times \mathbf{B})] \, dV, \tag{4.9}$$

where the integration is over the volume V. Typically, the magnetic torque comes

mainly from the magnetic tension rather than pressure force. The dominant magnetic tension term can be simplified to a surface integral (Matsumoto & Tomisaka 2004)

$$\mathbf{N}_t = \frac{1}{4\pi}\int(\mathbf{r}\times\mathbf{B})(\mathbf{B}\cdot d\mathbf{S}), \tag{4.10}$$

over the surface S of the volume. This volume-integrated magnetic torque is to be compared with the rate of angular momentum advected into the volume through fluid motion,

$$\mathbf{N}_a = -\int\rho(\mathbf{r}\times\mathbf{v})(\mathbf{v}\cdot d\mathbf{S}), \tag{4.11}$$

which will be referred to as the advective torque below.

Since the initial angular momentum of the protobinary envelope is along the z-axis, we will be mainly concerned with the $z-$component of the magnetic and advective torque,

$$N_{t,z} = \frac{1}{4\pi}\int(xB_y - yB_x)(\mathbf{B}\cdot d\mathbf{S}) \tag{4.12}$$

and

$$N_{a,z} = -\int\rho(xv_y - yv_x)(\mathbf{v}\cdot d\mathbf{S}), \tag{4.13}$$

which can change the $z-$component of the angular momentum L_z within the volume V.

As an example, we show in Fig. 5-6 the distributions of the magnetic and advective torques $N_{t,z}$ and $N_{a,z}$ for cubic boxes of different sizes that are centered at the origin, at the representative time $t \approx 39$ kyr for the $\lambda = 2$ case. As expected, the volume-integrated magnetic torque is negative for boxes of most sizes; it removes angular momentum from the material inside the boxes through magnetic braking. At the time shown, the braking torque is particularly large outside $\sim 10^{16}$ cm from the origin, reaching absolute values of order 10^{41} g cm^{2}s^{-2} or larger. To appreciate how large this torque is, we note that the orbital angular momentum of the protobinary in the hydro case is $\sim 4.4\times10^{52}$ g cm^{2}s^{-1} around the same time. This angular momentum would

be removed by the above magnetic torque on a time scale of 13 kyr, much shorter than the envelope collapse time. Given the magnitude of the magnetic torque, it is not surprising that the orbital angular momentum (and thus the separation) of the protobinary can be reduced significantly.

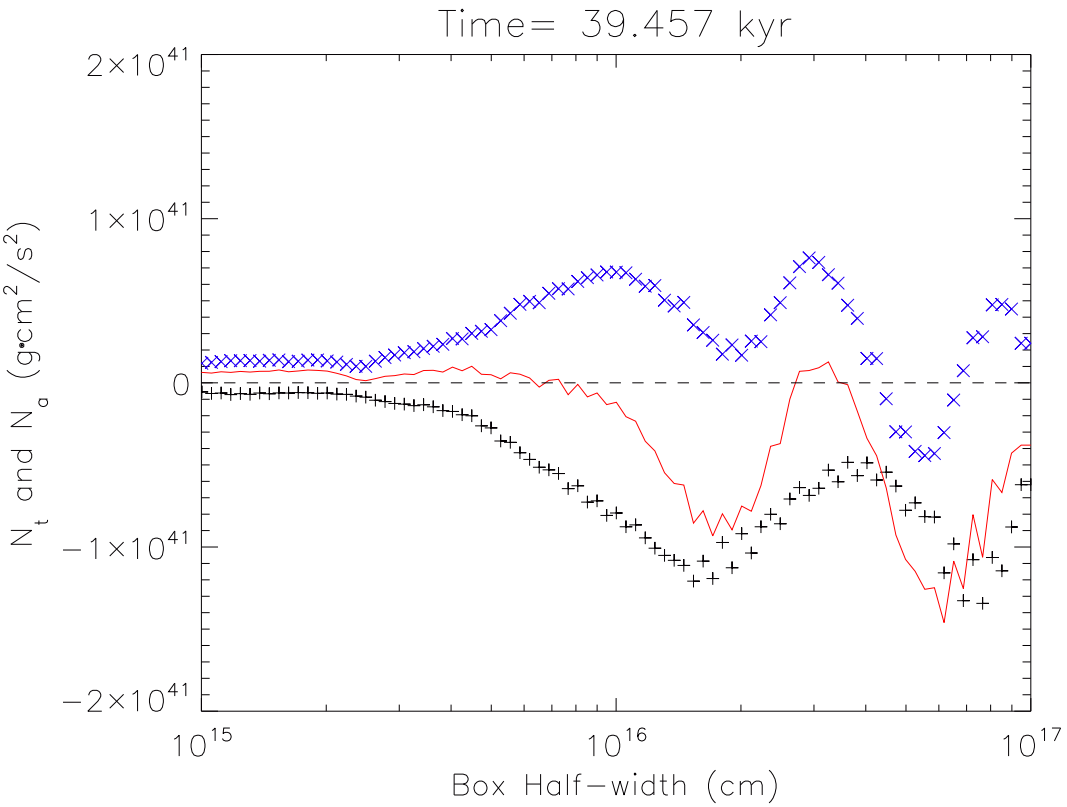

Fig. 4-5.— The magnetic (black '+') and advective (blue 'x') torque and the sum of the two (red) for cubic boxes of different half-width b for the $\lambda = 2$ case, at a representative time $t \approx 39$ kyr. A positive torque increases the angular momentum within a volume whereas a negative one decreases it.

The magnetic torque changes with time, however. At the time shown in Fig. 5-6, the magnetic torque overwhelms the advective torque for boxes of most sizes, leading to a net decrease of the angular momentum with time for the material in these boxes. This may not happen at other times. To evaluate the accumulative effects of the

magnetic and advective torque over time, we define for each box of half width b

$$L_{t,z}(b,t) = \int_0^t N_{t,z}(b,t')dt' \tag{4.14}$$

and

$$L_{a,z}(b,t) = \int_0^t N_{a,z}(b,t')dt' \tag{4.15}$$

which are the amount of the $z-$component of the angular momentum inside the box changed by the magnetic and convective torque, respectively, up to time t. These two quantities are to be compared with the actual change of the angular momentum inside each box between time t and $t = 0$,

$$\Delta L_z(b,t) = L_z(b,t) - L_z(b,t=0). \tag{4.16}$$

Barring a significant gravitational torque, one expects $\Delta L_z(b,t)$ to be close to $L_{a,z}(b,t)$ in the hydro case, because fluid advection should be the main channel for angular momentum change. This is indeed the case, as illustrated in panel (a) of Fig. 4-6, where both $\Delta L_z(b,t)$ and $L_{a,z}(b,t)$ are plotted as a function of the box size b at the representative time $t \approx 39$ kyr. The change in angular momentum $\Delta L_z(b,t)$ does follow closely the advected angular momentum for boxes of sizes larger than $\sim 10^{16}$ cm. For boxes of smaller sizes, there is significantly more angular momentum advected into a box than the actual angular momentum change in it, indicating that a good fraction of the angular momentum advected into the box is transported back out, presumably by the gravitational torques associated with the spiral arms that are visible in the left panel of Fig. 4-1. The gravitational torques may also be responsible for the small excess of $L_{a,z}(b,t)$ over $\Delta L_z(b,t)$ for the larger boxes.

The situation is very different in the presence of a relatively strong magnetic field, as shown in panel (b) of Fig. 4-6. Plotted are $L_{t,z}(b,t)$, $L_{a,z}(b,t)$, and $L_{t,z}(b,t) + L_{a,z}(b,t)$ together with $\Delta L_z(b,t)$ as a function of box size at $t \approx 39$ kyr for the $\lambda = 2$

case. The total change of the angular momentum due to the magnetic and advective torque acting on the boundary of a box, $L_{t,z}(b,t)+L_{a,z}(b,t)$, is very close to the actual change in angular momentum inside the box, $\Delta L_z(b,t)$, indicating that any additional torques (such as gravitational torques), if present, play a relatively minor role in angular momentum transport. This is not surprising, because the prominent spiral arms of the hydro case are disrupted by the magnetic field completely. More importantly, the sum $L_{t,z}(b,t)+L_{a,z}(b,t)$ has a magnitude much smaller than $|L_{t,z}(b,t)|$ and $|L_{a,z}(b,t)|$ individually, which means that most of the angular momentum advected into a box is removed by the magnetic braking, leaving little net angular momentum change in it. This is unequivocal evidence that the magnetic braking in the $\lambda = 2$ case controls the angular momentum evolution of the protostellar accretion flow, which in turn shapes the orbit of the protobinary.

The effect of magnetic braking is even stronger than indicated by panel (b) of Fig. 4-6. This is because $L_{a,z}(b,t)$ is the net angular momentum advected into a box, i.e., the sum of the positive angular momentum advected into the box $L^{+}_{a,z}(b,t)$ and the negative angular momentum advected out of the box $L^{-}_{a,z}(b,t)$. In the $\lambda = 2$ case, the magnetic braking drives an outflow, which produces a negative angular momentum $L^{-}_{a,z}(b,t)$ that is not much smaller in magnitude than $L^{+}_{a,z}(b,t)$. In other words, the angular momentum advected by infall into a box is larger than that shown in Fig. 4-6, and most of this larger angular momentum is removed by both the magnetic braking itself and the braking-induced outflow.

To illustrate the effect of magnetic braking more visually, we plot in Fig. 4-7 the distribution of specific angular momentum on the equatorial plane for the hydro and $\lambda = 2$ case at the representative time $t \approx 39$ kyr. It is clear that, for the hydro case, the specific angular momentum is roughly constant within a dimensionless radius of ~ 0.05 (or $\sim 2.5 \times 10^{16}$ cm), indicating that the collapsing material has a more or less conserved angular momentum before it is accreted by the protobinary. The relatively large specific angular momentum of the accreted material is what drives

the binary separation to increase. In the $\lambda = 2$ case, the specific angular momentum of the material to be accreted is much smaller; it is reduced by twisted field lines (see Fig. 4-4) as the material falls toward the binary. It is the accretion of the severely braked, low angular momentum material that drives the protobinary closer with time.

4.3.3 Circumstellar and Circumbinary Structures

We have already seen from Fig. 4-1 that a realistic magnetic field of $\lambda = 2$ changes the circumstellar and circumbinary structures of the HD case greatly: the prominent features of the HD case, two well-defined circumbinary disks and a circumbinary disk with two prominent spiral arms, are replaced by two low density lobes, which are filled with the magnetic flux decoupled from the matter that has been accreted onto the binary, i.e., the DEMS (Zhao et al. 2011; see also Seifried et al. 2011; Joos et al. 2012; Krasnopolsky et al. 2012). These strongly magnetized structures present an obstacle to mass accretion onto the protobinary. Although the DEMS tend to be less prominent for weaker magnetic fields, they still dominate the face-on view of the $\lambda = 4$ and 8 cases, especially at late times. An implication is that, for protostellar envelopes magnetized to a realistic level (with $\lambda \sim$ a few), the protobinary mass accretion does not follow the traditional path: from the envelope to a circumbinary disk to circumstellar disks to individual stars. Rather, the envelope material collapses directly close to the stars typically, and be accreted along azimuthal directions not occupied by the DEMS.

Another magnetic effect on the circumbinary environment is illustrated in Fig. 4-8, where we display both the edge-on and face-on view of the $\lambda = 2$ case at a relatively early time $t = 18$ kyr. The edge-on view shows that the protobinary is surrounded by two large, mostly expanding, regions (one each above and below the equator) that are absent in the HD case. Their dynamics are dominated by the rotationally twisted magnetic fields (see Fig. 4-4). It is in these regions that most of the angular

momentum extracted magnetically from the material that falls into the stars is stored. Such bipolar expanding regions are seen in many magnetized core collapse simulations (for an early example, see Tomisaka 1998). They block the protobinary accretion over most of the solid angle, and force the accretion to occur mainly through a flattened, equatorial structure — a circumbinary pseudodisk (Galli & Shu 1993).

The pseudodisk is also clearly visible in the face-on view of the system in the right panel of Fig. 4-8, as a nearly circular region of enhanced column density. Unlike the circumbinary disk in the HD case (see the left panel of Fig. 4-1), the pseudodisk is not rotationally supported. It falls supersonically inward, and the infall can be seen in the velocity fields shown in Fig. 4-8. Another difference is that the circumbinary pseudodisk does not have prominent spiral arms. This is not surprising, because the pseudodisk is strongly magnetized, which makes gas compression more difficult. The rapid infall also leaves little time for the spirals to develop. The lack of spiral arms is consistent with our earlier result that the angular momentum transport in the $\lambda = 2$ case is dominated by magnetic braking rather than gravitational torque.

4.3.4 Protobinary Mass Growth

Despite the differences in the morphology and dynamics of the circumbinary environment with and without a magnetic field, the stars grow at remarkably similar rates in all cases (of order $\sim 10^{-6}\,\mathrm{M}_\odot/\mathrm{yr}$). This is shown in Fig. 4-9, where the mass of each component of the protobinary is plotted as a function of time, for different degrees of magnetization. The reason for the similarity is that the mass accretion rate is determined mainly by the dynamics on the envelope scale: the material collapsing down from the envelope will find a way to the stars sooner or later, irrespective of the details of the circumbinary environment. In the HD or weakly magnetized cases, there is more material parked in the circumstellar and circumbinary disks, making the mass accreting rate onto the stars lower. However, this effect is smaller than that from the retardation of envelope collapse by magnetic tension in the stronger

field cases. As a result, the protostellar mass accretion rate is somewhat lower in the stronger field cases, although not by a large factor.

It is reassuring that the masses of the two initially equal-mass components stay nearly the same for all cases, despite the fact that the inner protobinary accretion flow can become rather disordered at times, especially for strongly magnetized cases. The magnetic field does not appear to change much the rate of mass accretion by one component relative to the other, although the situation is drastically different for initially unequal mass protobinaries, as we demonstrate next.

4.4 Magnetic Braking and Mass Ratio of Unequal-Mass Protobinaries

The vast majority of low (Sun-like) mass binaries are unequal-mass systems (Duquennoy & Mayor 1991; Raghavan et al. 2010). The mass ratio, defined as $q = M_2/M_1$ where M_1 and M_2 are the mass of the primary and secondary respectively, is one of the fundamental parameters that characterize the binaries. Its observed distribution provides important constraints on binary formation and evolution (see discussion in § 4.5).

The mass ratio q of protobinaries is expected to be affected by magnetic braking. This is because the change of q depends on the specific angular momentum of the circumbinary material to be accreted relative to that of the binary. It is well known that high angular momentum material tends to accrete preferentially onto the less-massive secondary, which has a higher specific angular momentum than the primary, driving the mass ratio toward unity (Bate & Bonnell 1997; Bate et al. 2002). As we have seen above, magnetic braking can remove the angular momentum of the circumbinary material efficiently. It is expected to weaken the tendency for preferential accretion onto the secondary. We show that it is indeed the case in Fig. 4-10.

Shown in Fig. 4-10 are the mass ratios as a function of time for three cases $\lambda = \infty$

(HD), 16 and 2. The initial conditions are the same as those for the equal-mass cases discussed in § 4.3, except that the mass and angular momentum inside the radius r_h of the power-law envelope are given to a binary system of mass ratio $q = 0.25$ rather than $q = 1$. The mass ratio increases with time in the HD case, in agreement with previous results. As expected, the magnetic field slows down the increase in q compared to the HD case. Even a rather weak magnetic field of $\lambda = 16$ has an appreciable effect on the mass ratio evolution. For the more realistic value of $\lambda = 2$, the primary accretes much faster than the secondary, by a factor of 3-4, so that the mass ratio remains roughly constant. The large contrast between the HD and $\lambda = 2$ case leaves little doubt that magnetic braking is an important factor to consider in understanding the mass ratio distribution of binaries. We will leave a comprehensive exploration of this issue to a future investigation.

4.5 Summary and Discussion

We have carried out a set of idealized numerical experiments to demonstrate the effects of the magnetic field on protobinary evolution during the mass accretion phase. The protostellar envelope was idealized as a rotating, magnetized singular isothermal sphere. Its collapse onto a pre-existing pair of binary seeds was followed using an MHD version of the ENZO AMR hydro code that includes a sink particle treatment. We found that a magnetic field of the observed strength (corresponding to a dimensionless mass-to-flux ratio of a few) can remove, through magnetic braking, most of the angular momentum of the material that reaches the protobinary. The reduction in the angular momentum of the protobinary accretion flow has two important consequences: compared to the non-magnetic case, (1) the protobinary orbit becomes much tighter, and (2) the mass-ratio does not increase as fast with time for initially unequal mass systems. In addition, the magnetic field drastically changes the morphology and dynamics of the structures that surround the protobinary. It

suppresses the formation of the familiar circumstellar and circumbinary disks in the non-magnetic case, as well as the spiral arms embedded in them. These structures are replaced by a bipolar magnetic-braking driven expanding regions, a dense, infalling, circumbinary pseudodisk in the equatorial region, and low-density, highly magnetized structures close to the protobinary that expand against the pseudodisk (the DEMS). We conclude that both the basic characteristics (such as mass ratio and separation) of the protobinaries and the environment in which binaries grow are strongly modified by a realistic magnetic field.

The magnetic braking-driven inward migration of protobinaries may have observable consequences. As mentioned in the introduction, the distribution of binary orbital separation during the earliest, Class 0 phase of star formation may be different from those at later times. In particular, there is tentative evidence for a "desert" free of Class 0 binaries with separation between $\sim 150 - 550$ AU (Maury et al. 2010; Enoch et al. 2011), which is not present in the Class I or later phases. If confirmed by future observations, this gap must be filled in by binaries from either outside the gap or interior to it. The magnetic braking is an efficient way of shrinking the protobinary orbit. It can in principle move some binaries born on wide orbits outside the gap into the gap. Indeed, Offner et al. (2009, 2010) found that most of the binaries in their cluster formation simulations were born with relatively wide separations, as a result of radiative feedback, which tends to suppress close binary formation through disk fragmentation; the orbits of such wide binaries could be tightened by magnetic braking[2]. A potential problem is that the braking may be so efficient during the protobinary mass accretion phase (when a massive, slowly rotating envelope is still present) that the binary separation would move quickly through the gap and pile up below the resolution of the current generation of millimeter/submillimeter interferom-

[2]Bate (2012) found that the binaries in his radiation hydro simulations of cluster formation have properties consistent with observations, indicating that magnetic effects are not needed. It would be interesting to quantify how a magnetic field of the observed strength modifies the properties of the binaries formed in a cluster environment.

eters ($\sim 50-100$ AU). If this is the case, one would expect to find an over-abundance of relatively close protobinaries with separation $\lesssim 100$ AU that may be uncovered by ALMA and JVLA. The same pileup at small separations would also occur if the binaries born on tight orbits interior to the gap are kept from expanding into the gap by magnetic braking.

The problem of potentially turning most wide binaries into close binaries is related to the magnetic braking catastrophe in disk formation (Galli et al. 2006). Both semi-analytic arguments and numerical simulations have shown that, in magnetized laminar dense cores of λ of a few, the formation of a rotationally supported disk is suppressed by magnetic braking in the ideal MHD limit (Allen et al. 2003; Galli et al. 2006; Price & Bate 2007; Mellon & Li 2008; Hennebelle & Fromang 2008; Seifried et al. 2011; Dapp & Basu 2011). The magnetic braking must be weakened somehow in order to form both large-scale disks and wide binaries. In the context of disk formation, there are several proposed mechanisms for weakening the magnetic braking, including the misalignment between the magnetic and rotation axes (Joos et al. 2012), turbulence (Santos-Lima et al. 2012; Seifried et al. 2012; Myers et al. 2012), and the depletion of the slowly rotating protostellar envelope that acts to brake the disk, either by outflow stripping (Mellon & Li 2008) or accretion (Machida et al. 2010). The last possibility is particularly intriguing, because it implies a rapid growth of the rotationally supported disk during the transition from the deeply embedded Class 0 phase to the more revealed Class I phase that can be observationally tested. Similarly, the depletion of the protobinary envelope and the associated weakening of magnetic braking may enable the separation of the protobinaries to grow quickly during the Class 0-Class I transition. If this is the case, the orbits of wide binaries may first shrink during the Class 0 phase due to efficient magnetic braking and then re-expand as the protobinary envelope depletes. This and other possibilities for protobinary migration should be testable with high-resolution millimeter/submillimeter interferometric observations, especially using ALMA and JVLA.

Our calculations demonstrated that magnetic braking is important for the evolution of not only the binary separation, but also the mass ratio q. Raghavan et al. (2010) found a roughly flat distribution for q between 0.2-0.95, with a valley below 0.2, and three spikes around 0.25, 0.35 and 1.0 (see the left panel of their Fig. 16). It is tempting to attribute the last spike at $q \sim 1$ to the preferential accretion of high specific angular momentum material onto the lower-mass component found in hydrodynamical simulations (Bate & Bonnell 1997; Bate et al. 2002). However, the spike around $q \sim 1$ is just one of the three spikes in Raghavan et al.'s data, and it does not show up in the sample of Duquennoy & Mayor (1991) at all (see their Fig. 10). In any case, there are many more systems with mass ratio q well below unity than close to unity. A mechanism must be found to prevent the majority of the low-mass ratio protobinaries from becoming equal-mass systems. The magnetic braking highlighted in this Chapter is one such mechanism. It is a key factor to consider in understanding binary formation and evolution in dense cores that are observed to be significantly magnetized.

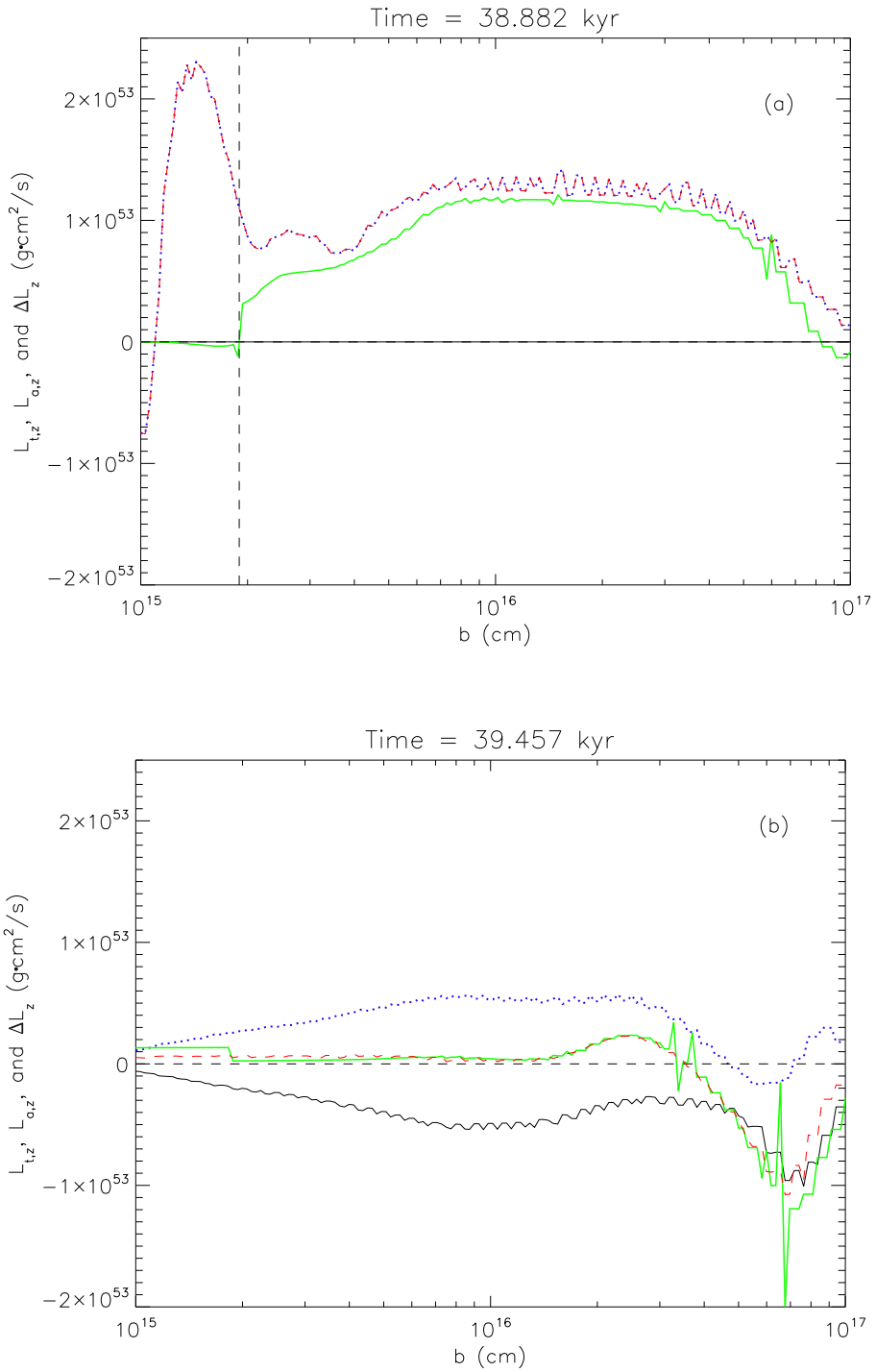

Fig. 4-6.— The integrated magnetic and advective torques $L_{t,z}$ (black solid), $L_{a,z}$ (blue dotted), and their sum $L_{t,z}+L_{a,z}$ (red dashed) together with the actual angular momentum change ΔL (green thick solid) for cubic boxes of different half-width b. The HD case is shown in panel (a) with zero $L_{t,z}$ and the $\lambda = 2$ case is shown in panel (b), both at a similar time $t \approx 39$ kyr. The vertical dashed line in panel (a) indicates the approximate position of the sink particles, whereas in panel (b) such particle position lies below 10^{15} cm.

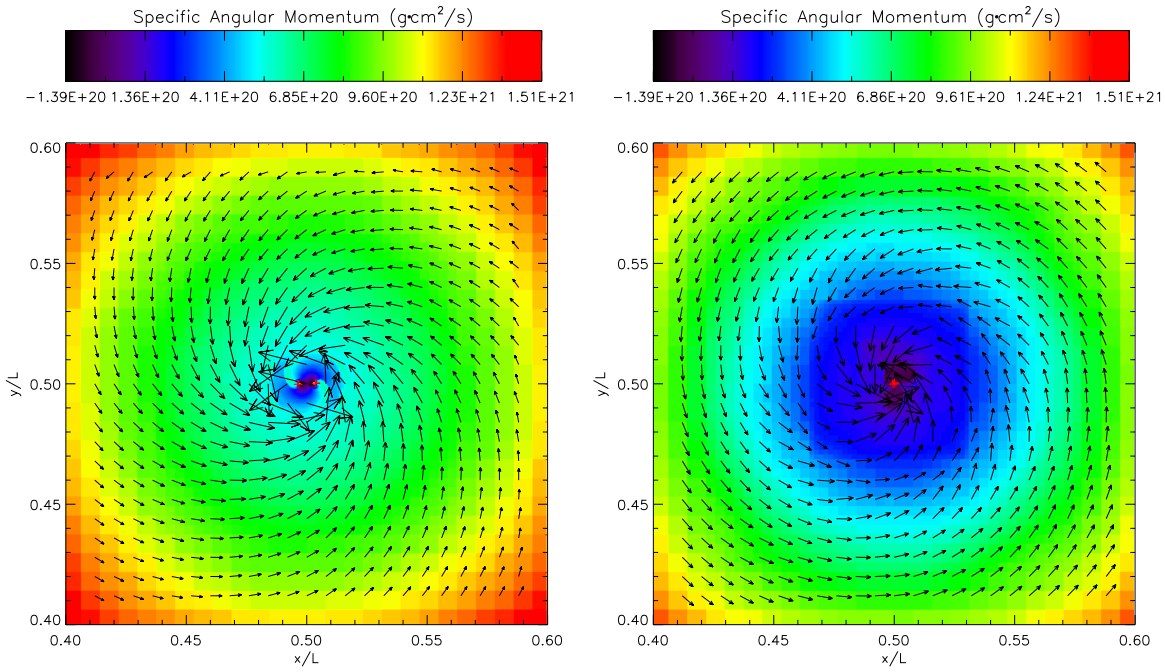

Fig. 4-7.— Snapshot of the gas specific angular momentum (in $g \cdot cm^2 \cdot s^{-1}$ with logarithm scale) on the equatorial plane of the inner accretion flow for the HD case (left panel) and the $\lambda = 2$ case (right panel) at $t \approx 39$ kyr, showing the strong braking of the material to be accreted by the protobinary in the magnetized case compared to the HD case. The arrows are velocity vectors, and the crosses mark stars. Only the central region of 10^{17} cm on each side is plotted.

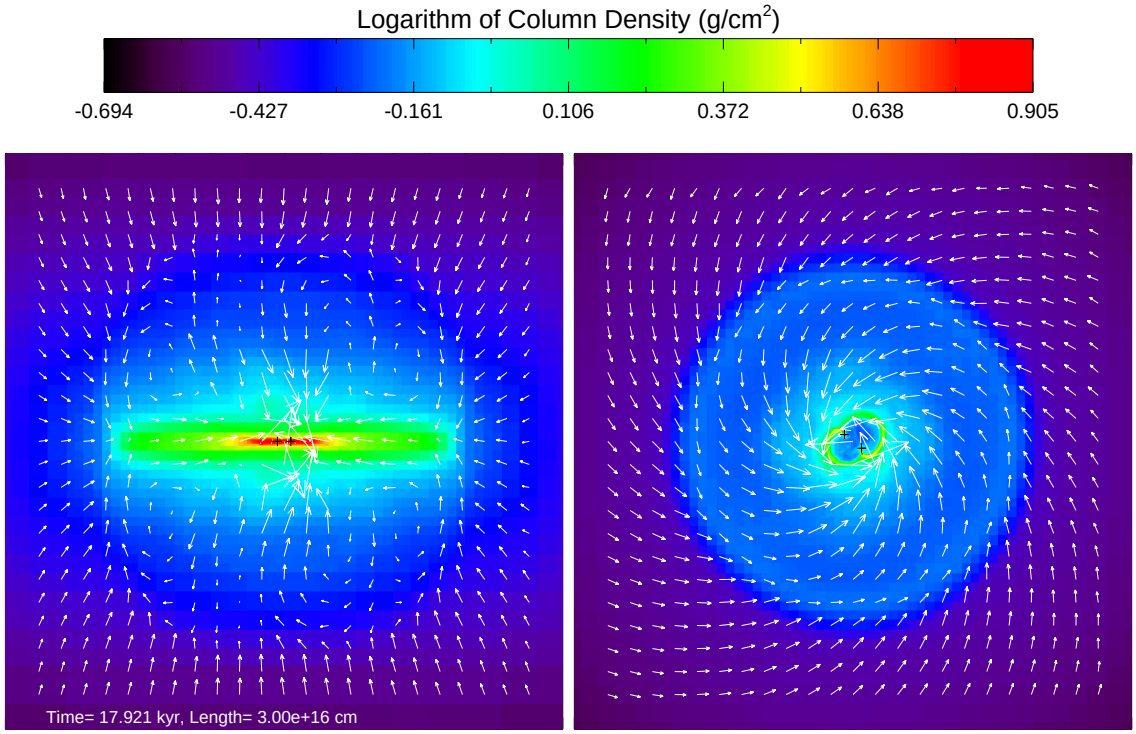

Fig. 4-8.— Left panel: edge-on view of the column density in the $\lambda = 2$ case at $t = 18$ kyr, showing two slowly expanding polar regions sandwiching an infalling, circumbinary pseudodisk in the equatorial region. Right panel: face-on view of the same structure, showing that the circumbinary pseudodisk is not rotationally supported; it collapses rapidly.

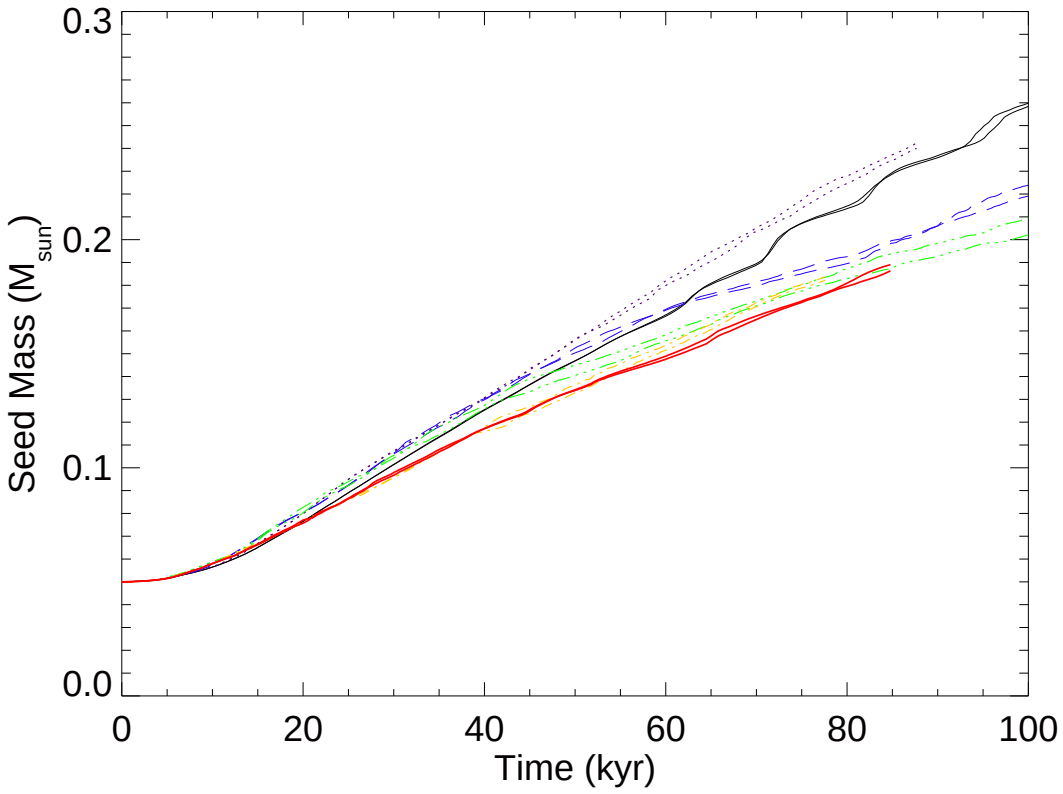

Fig. 4-9.— Stellar mass (in solar units) growth of the initially equal-mass binary system for HD (black solid), $\lambda = 32$ (purple dotted), $\lambda = 16$ (blue long-dashed), $\lambda = 8$ (green dash-dot-dot-dotted), $\lambda = 4$ (yellow dash-dotted), and $\lambda = 2$ (red thick solid) cases. Note that, in all cases, the two stars stay roughly equal-mass at all times.

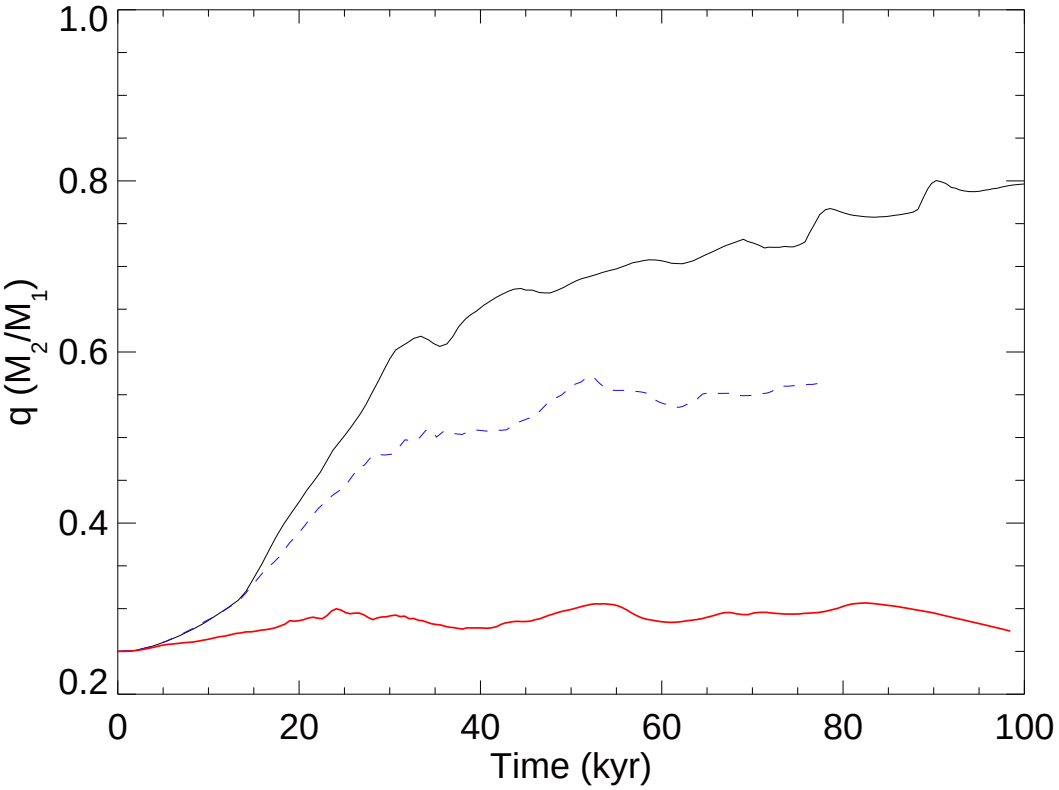

Fig. 4-10.— Evolution of the protobinary mass ratio q with time for envelopes that have different levels of magnetization, with $\lambda = \infty$ (HD, black solid), 16 (blue dashed), and 2 (red thick solid).

Chapter 5

Effect of Magnetic Misalignment on Protobinary Evolution

This chapter is based on a paper submitted to ApJ (Zhao, Li, & Kratter 2014).

5.1 Introduction

Stars form in dense cores that are often observed to be significantly magnetized (Troland & Crutcher 2008). The spin-up of infalling gas due to angular momentum conservation twists these magnetic field lines, at least in the ideal MHD limit. This twisting and the associated magnetically driven outflow transport angular momentum outward from the forming star. For realistic levels of magnetization, both analytical and numerical work has shown that this magnetic braking (in the ideal MHD limit) suppresses the formation of rotationally supported disks (Allen et al. 2003; Galli et al. 2006; Price & Bate 2007; Mellon & Li 2008; Hennebelle & Fromang 2008; Dapp & Basu 2010; Krasnopolsky et al. 2012). However, Keplerian disks are routinely observed around evolved Class II objects(e.g. Williams & Cieza 2011), and increasingly around Class I (Jørgensen et al. 2009; Enoch et al. 2009; Takakuwa et al. 2012), perhaps even Class 0 sources (Tobin et al. 2012).

The aforementioned studies have all assumed uniform rotation profiles aligned with a uniform magnetic field. Observed cores, however, have both turbulent velocity profiles (Goodman et al. 1993) and likely non-uniform, misaligned fields . Recent CARMA survey of low mass Class 0 protostars indicates that a number of sources have substantial misalignment between the magnetic field and bipolar outflow axis, which is often taken as a proxy for the rotation axis (Hull et al. 2013). More recent numerical simulations have shown that misalignment between the field and rotation axis allows for the formation of extended disk in moderately magnetized cores due to less efficient magnetic braking and weaker outflows (Joos et al. 2012; Li et al. 2013).

In this Chapter, we consider the influence of field alignment on the formation of binary stars. Since both the formation and orbital parameters of binaries are linked to the angular momentum evolution in the natal core (e.g., Hanawa et al. 2010), we expect the field geometry to strongly influence the configuration of young binaries. As discussed in Chapter 1, binary formation may be the dominant channel for star

formation. Both field stars and pre-main sequence stars show high binary fractions. For field stars of $\gtrsim 1M_{\odot}$, the binary fraction is $\gtrsim 50\%$ (Duquennoy & Mayor 1991; Raghavan et al. 2010; Janson et al. 2012). Young clusters show multiplicity fraction in excess of $60-70\%$ (Reipurth & Zinnecker 1993; Mathieu et al. 2000; Duchêne et al. 2004, 2007; Kraus et al. 2011). The high fraction of multiples at birth may indicate that the majority of stars are formed in multiple systems, especially binaries.

In Zhao & Li (2013) (hereafter ZL13; see also Chapter 4), we studied the influence of magnetic fields on the growth and orbital evolution of protobinary seeds embedded in a magnetized core. We found that for magnetic fields aligned with the core rotation axis, strong magnetic braking efficiently shrinks the binary separation on a timescale shorter than 10^5 yrs by removing angular momentum from the infalling gas. In contrast, similar simulations of binary formation in the hydrodynamic limit find that the binary separations typically increase after birth due to the accretion of high angular momentum material (Kratter et al. 2010). If most binaries form on wide ($\sim 500-1000$ AU) orbits in magnetized cores, it could provide an explanation for the non-detection of closer systems ($\sim 150-550$ AU) in the Class 0 phase, as claimed by Maury et al. (2010) and Enoch et al. (2011). Magnetic braking may shrink the orbits of some of these wide binaries, and perhaps contribute to the higher binary fraction for Class I sources (as high as $\sim 18\%$ in the same separation range (Connelley et al. 2008)).

In this Chapter, we extend our study of protobinaries to include cores with tilted magnetic fields. We compare the accretion history and orbital evolution of misaligned and aligned systems. We use the MHD version of ENZO AMR code described in Chapter 2 (see also Bryan & Norman 1997; O'Shea et al. 2004; Wang & Abel 2009; Wang et al. 2010) to run a series of simulations analogous to ZL13 but with misaligned fields. We show that the change in the efficiency of magnetic braking in the binary case is not entirely analogous to that effect in the single star case. In § 5.2, we discuss the initial setup for the binary seeds and the rotating magnetized gas envelope. Our

main results are presented in § 5.3, where we show that the field misalignment reduces, rather than increases, the binary separation compared to the case where the field and rotation axes are aligned. We demonstrate how this result is echoed by the changes in disk and outflow morphology in § 5.3.4. Finally, we discuss the implications of our results for observed systems in § 5.4.

5.2 Problem Setup

To facilitate comparison with ZL13, we mimic their initial conditions (see also Chapter 4). We begin with a pair of binary seeds at the center of the dense core, and vary both the strength and the orientation of the global magnetic field with respect to the rotation axis. For completeness, we briefly summarize the initial conditions, and describe the implementation of different magnetic field inclinations.

We initialize the protobinary envelope with a self-similar density profile (Shu 1977):

$$\rho(r) = \frac{Ac_s^2}{4\pi G r^2}, \tag{5.1}$$

where c_s is the isothermal sound speed, and A an over-density parameter. Employing self-similar initial conditions provides a powerful check on numerical solutions. We adopt an over-density parameter $A = 4$, corresponding to a ratio of thermal to gravitational energy of $\alpha = 3/(2A) = 0.375$. The mass enclosed within any radius r is

$$M(r) = \frac{Ac_s^2}{G} r. \tag{5.2}$$

As in ZL13, the total core gas mass is $M_{\rm tot} = 1.2\,{\rm M}_\odot$, with a core radius $R = 10^{17}$ cm and isothermal sound speed $c_s = 0.2$ km/s (corresponding to a temperature of $\sim$ 10 K). The rotation speed of the core is chosen as $v_\phi = v_0 \sin\theta$ (where θ is the polar angle measured from the rotation axis, and $v_0 = c_s$), which preserves the self-similar collapse. Such a rotation profile corresponds to a ratio of rotational and gravitational

energy $\beta = (v_0/c_s)^2/(3A) \approx 0.083$. Note that this is somewhat higher than used in other works (e.g. Machida et al. 2010), but is still within the range inferred by Goodman et al. 1993 from NH_3 observations of dense cores.

Unlike ZL13, we now allow the magnetic field to tilt by $\theta_0 = 45°$ and $90°$ relative to the axis of rotation. The strength of the uni-directional magnetic field has the same initial profile of

$$B_z(\varpi) = \frac{Ac_s^2}{\sqrt{G}\lambda}\frac{1}{\varpi + r_h}, \tag{5.3}$$

where the λ is the dimensionless mass-to-flux ratio of the envelope in units of the critical value for a magnetically supported core $(2\pi G^{1/2})^{-1}$, r_h is the softening parameter to avoid the singularity at the origin. Note that the field strength decreases away from the magnetic axis as $1/\varpi$ (where ϖ is the cylindrical radius relative to the magnetic axis), so that the mass-to-flux ratio is constant spatially. We perform 10 simulations: we have two tilt angles 45° and 90° for 5 levels of initial magnetization of $\lambda = 2$, 4, 8, 16, and 32. These are compared with the aligned cases (with $\theta_0 = 0°$) of ZL13.

The binary stars are modeled in the same way as in ZL13 using sink particles. The simulations are initialized with two sink particles separated by $a \approx 246$ AU at the center of the protostellar envelope (see Eq. 5 of ZL13). The seeds have a small initial mass of $0.05\,\mathrm{M}_\odot$ each and thus do not significantly modify the core potential. The sinks are allowed to accrete mass from the surroundings based on the modified Bondi-Hoyle formula (see Ruffert 1994).

5.3 Results

5.3.1 Protobinary Migration

We first investigate the effect of field misalignment on the evolution of the binary orbit. Varying the magnetic field strength affects the binary separation more than

varying the alignment. We show the influence of field strength on separation for the orthogonal case ($\theta_0 = 90°$) in Fig. 5-1. As in ZL13, the binary separation decreases with increasing magnetic field strength. Contrary to the expectation based on the single star case, weaker braking does not inhibit the shrinking of the binary orbit.

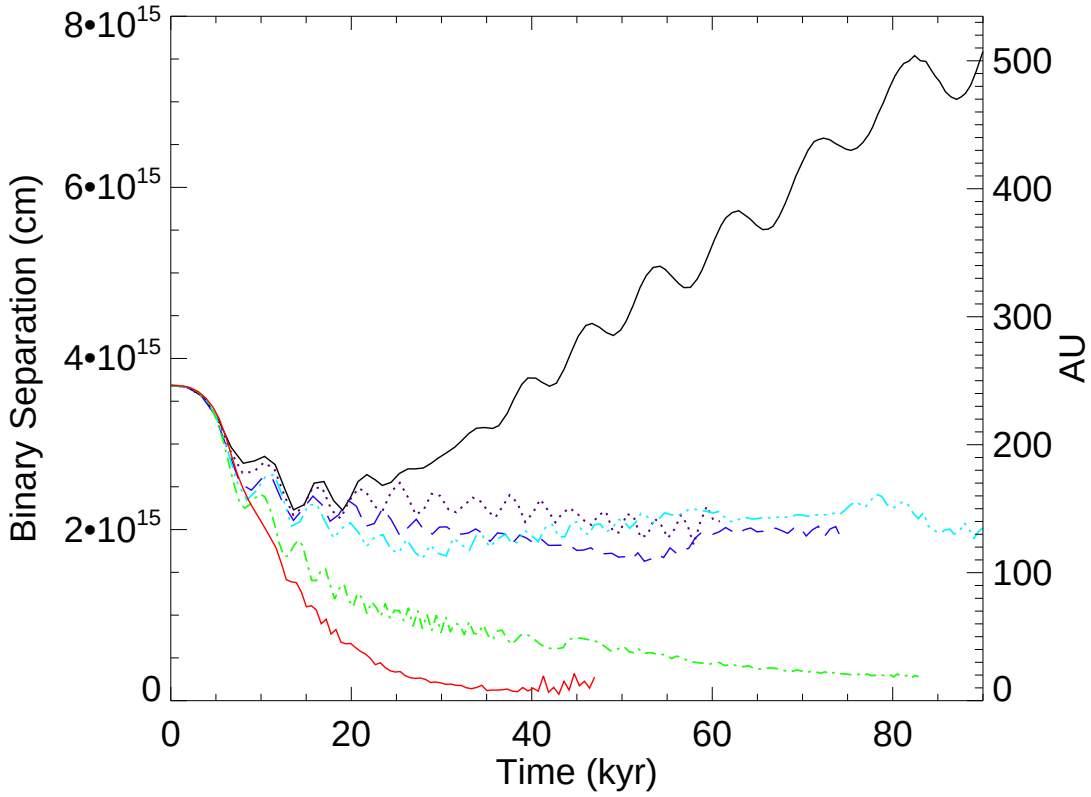

Fig. 5-1.— Evolution of binary separation with time for HD (black solid), $\lambda = 32$ (purple dotted), $\lambda = 16$ (blue long-dashed), $\lambda = 8$ (teal dash-dot-dot-dotted), $\lambda = 4$ (green dash-dotted), and $\lambda = 2$ (red thick solid) cases. All magnetic cases have tilt angle $\theta_0 = 90°$.

For the same level of magnetization, we find that the binary separation is smaller for larger tilt angles at any give time. This is illustrated in Fig. 5-2 for $\lambda = 4$[1]. The difference between the orthogonal case and the aligned case is modest. One might

[1]We mainly focus on the two extreme cases with $\theta_0 = 0°$ and $90°$. The intermediate case $\theta_0 = 45°$ largely lies in between.

naively assume that the tighter binary separation in the tilted case is due to stronger magnetic braking. However, this would contradict the results of Joos et al. (2012) and Li et al. (2013). To ascertain the cause of angular momentum removal from the binary we plot the evolution of orbital angular momentum for different tilt angles in Fig. 5-3.

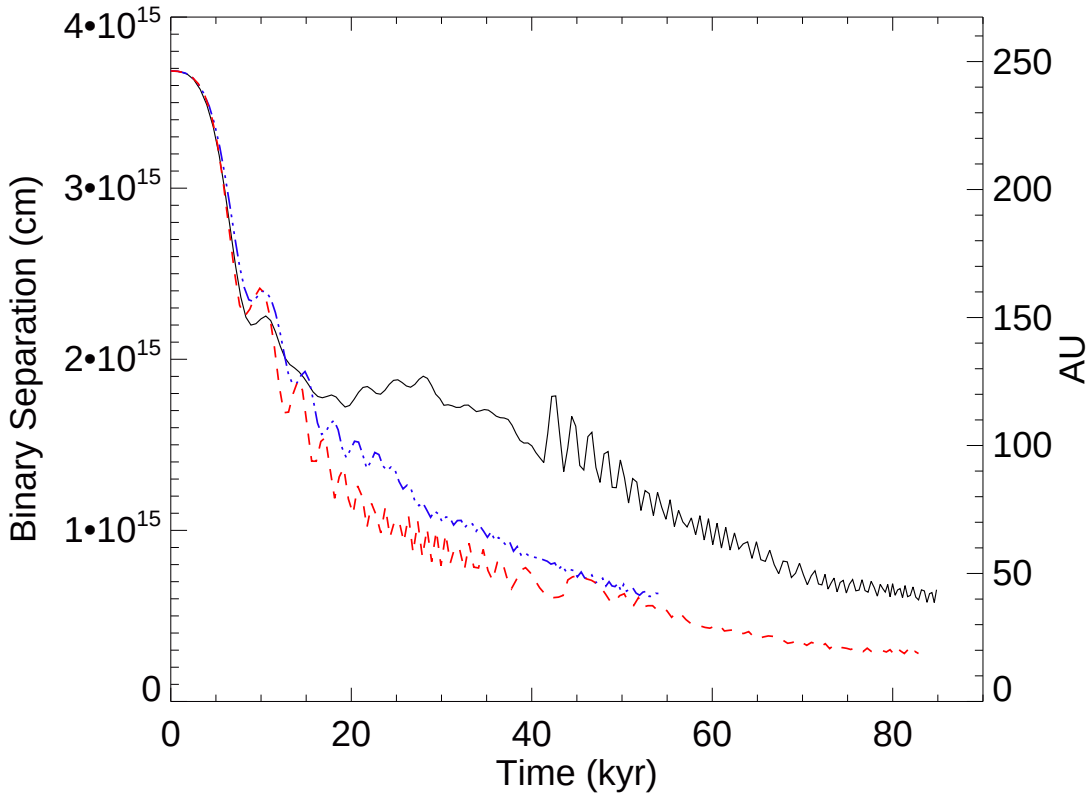

Fig. 5-2.— Evolution of binary separation with time for $\lambda = 4$ cases with different tilt angles: 0° (black solid), 45°(blue dash-dotted), and 90° (red dashed).

Fig. 5-3 shows that the orbital angular momentum is larger in the orthogonal case than in the aligned case, consistent with the result of Joos et al. (2012) and Li et al. (2013) for single star formation. However, the orbit is determined by the angular momentum per unit mass, therefore we need to account for the influence of the field misalignment on stellar accretion.

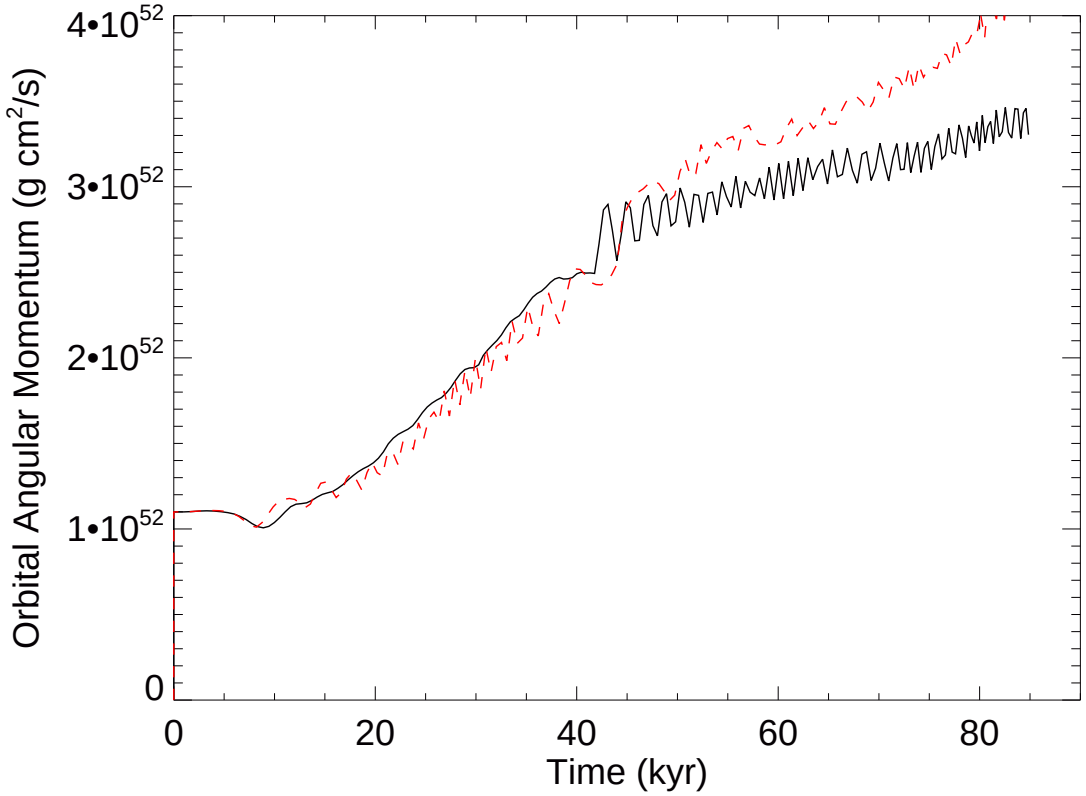

Fig. 5-3.— Evolution of binary orbital angular momentum with time for $\lambda = 4$ cases with different inclination angles: 0° (black solid) and 90° (red dashed).

We plot in Fig. 5-4 the stellar mass as a function of time for the $\lambda = 4$ case. It is clear that the binaries accrete faster in cases with a larger tilt angle. The difference is less than a factor of 2 for the two extremes ($\theta = 0°$ and 90°), but is sufficient to explain the smaller binary separation for the $\theta = 90°$ case compared to $\theta = 0°$ case shown in Fig. 5-2.

For a binary system on a circular orbit, the orbital angular momentum is given by

$$L_b = \frac{q}{(1+q)^2} G^{1/2} {M_b}^{3/2} {a_b}^{1/2}, \tag{5.4}$$

where L_b, M_b, and a_b are the orbital angular momentum, total mass and separation of the binary, respectively, and q is the mass ratio of the two stars. The binary

separation scales as $a_b \propto {L_b}^2 {M_b}^{-3}$. Thus an increase of binary mass by a factor of 1.5 yields a binary separation ~ 3 times smaller, given the same amount of available angular momentum. The reduction in orbital separation due to faster mass accretion is more than enough to offset the orbit widening due to the slightly larger orbital angular momentum in the orthogonal case (see Fig. 5-3). The change in accretion rate accounts for the factor of ~ 2 difference in the binary separation shown in Fig. 5-2 between the aligned and orthogonal case. It is largely consistent with the results of Joos et al. (2012) and Li et al. (2013). We now explore how field misalignment affects mass accretion onto the stars.

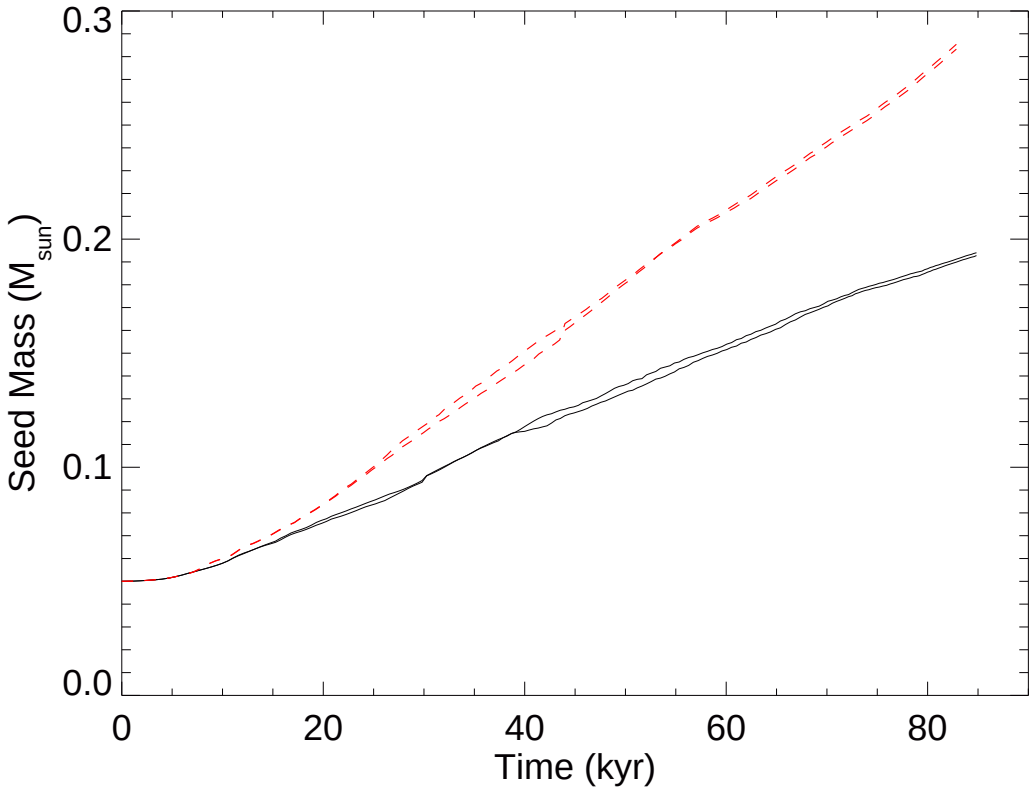

Fig. 5-4.— Stellar mass (in solar mass) growth with time for $\lambda = 4$ cases with different inclination angles of magnetic field: 0° (black solid) and 90° (red dashed). In all cases, each star is plotted separately.

5.3.2 Mass Accretion

We have shown that the variation in the mass accretion rate for different field geometries is key in understanding the orbital evolution. The accretion of more low specific angular momentum material in misaligned cases compensates for the weaker magnetic braking. We now investigate the difference in binary mass growth for different tilt angles by measuring the gas flow through different surfaces around the binary stars. Let us consider the mass flux through the surface S of a finite volume V, which can be expressed as,

$$\dot{M}_g = \int \rho \mathbf{v} \cdot d\mathbf{S} \tag{5.5}$$

Here positive mass flux represents inflow and negative represents outflow, e.g. fluid being advected inward or outward through the specified surface. As an example, we show in Fig. 5-5 the distribution of the mass flux $\dot{M}_g$ and its three Cartesian components for cubic boxes of different sizes that are centered at the origin[2]. As expected, the overall mass infall in the 90° case is almost 1.5 times as large as that in the 0° case in the region with box half-width between 2×10^{15} cm and 2×10^{16} cm ($\sim$ 1000 AU). The main driver for such difference is the z-component of the mass flux $\dot{M}_g$, whose value is almost the opposite in the two cases. In the aligned case, the magnetically-driven outflow dominates the gas dynamics within a distance of $\sim 4 \times 10^{15}$ cm to $\sim 2 \times 10^{16}$ cm from the center of mass. This outflow accounts for the bulk of the overall difference in total mass flux. In the orthogonal case where there is little toroidal field generated, and thus little or no outflow, the z-component of the mass flux is mostly positive. Both the x and y component of $\dot{M}_{\rm g}$ have similar sign and magnitude in the two cases, except for the innermost region close to the binary stars where the flows are becoming unstable (see section § 5.3.4).

The larger mass inflow may also be correlated with the topology of the magnetic field. In the aligned field case, the vertical toroidal field is severely pinched along the

[2]We use cubes rather than spheres for simplicity as these align with the AMR grid geometry, and thus require no interpolation between refinement levels.

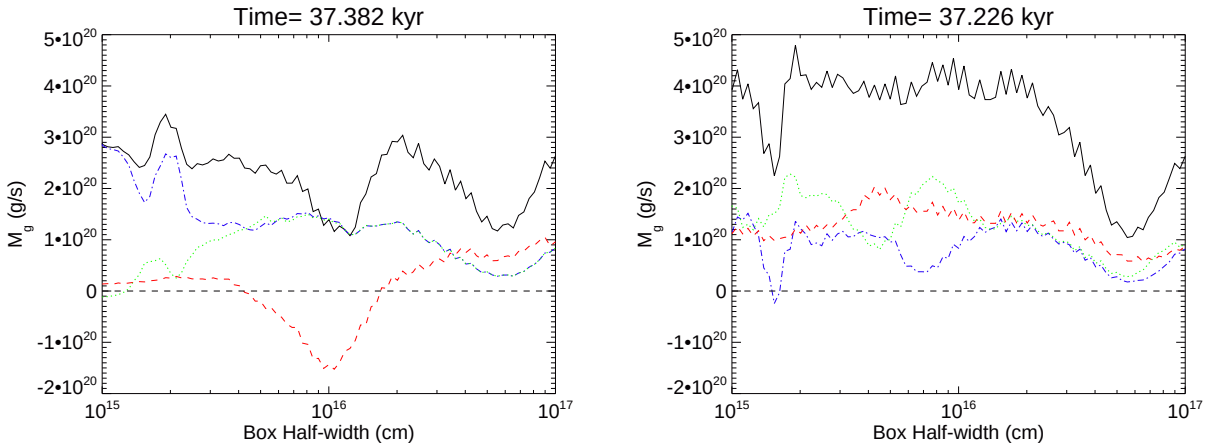

Fig. 5-5.— The total mass flux (black solid) and its three Cartesian components (blue dash-dotted: x-component; green dotted: y-component; red dashed: z-component) for cubic boxes of different half-width for the $\lambda = 4$, at a representative time $t \approx 37$ kyr. The left panel is the aligned case (0°) and the right panel is the orthogonal case (90°). A positive flux increases the mass within a volume (inflow) whereas a negative one decreases it (outflow).

equator as gas collapses towards the central objects. The resulting magnetic tension force impedes the gas infall, so that one would expect a lower accretion rate as time proceeds. On the contrary, in the orthogonal case, the magnetic tension force has limited influence on the gas accretion. Although the rotating gas winds the magnetic field around the binary seeds, the unwinding reaction by magnetic tension does not stop the gas from flowing along the field lines, which lead directly to the center of the system. Hence, the larger magnetic field inclination boosts the gas inflow around the binary.

5.3.3 Angular Momentum Transport

Mass flow in and around the binary not only delivers angular momentum directly, but also induces hydrodynamical torques (distinct from magnetic torque), which transport angular momentum. We use a similar approach as in § 5.3.2 to quantify the contributions from different torques to the angular momentum transport. For a finite

volume V with surface S, the total magnetic torque relative to the origin (from which a radius vector $\mathbf{r}$ is defined) is

$$\mathbf{N}_m = \frac{1}{4\pi}\int [\mathbf{r}\times((\nabla\times\mathbf{B})\times\mathbf{B})]\,dV, \tag{5.6}$$

where the integration is over the volume V. Typically, the magnetic torque comes mainly from magnetic tension rather than the magnetic pressure. The dominant magnetic tension term can be simplified to a surface integral (Matsumoto & Tomisaka 2004)

$$\mathbf{N}_t = \frac{1}{4\pi}\int (\mathbf{r}\times\mathbf{B})(\mathbf{B}\cdot d\mathbf{S}), \tag{5.7}$$

over the surface S of the volume. This volume-integrated magnetic torque is to be compared with the rate at which angular momentum is advected into and out of the volume through fluid motion,

$$\mathbf{N}_a = -\int \rho(\mathbf{r}\times\mathbf{v})(\mathbf{v}\cdot d\mathbf{S}), \tag{5.8}$$

which will be referred to as the advective torque below.

Since the initial angular momentum of the protobinary envelope is along the z-axis, we will be mainly concerned with the $z-$component of the magnetic and advective torque,

$$N_{t,z} = \frac{1}{4\pi}\int (xB_y - yB_x)(\mathbf{B}\cdot d\mathbf{S}), \tag{5.9}$$

and

$$N_{a,z} = -\int \rho(xv_y - yv_x)(\mathbf{v}\cdot d\mathbf{S}). \tag{5.10}$$

The advective torque can be separated into two components $N_{a,z}^{out}$ and $N_{a,z}^{in}$, for flow going out of and into the box, respectively.

In Fig. 5-6 we show the distributions of magnetic and advective torques $N_{t,z}$, $N_{a,z}$, and $N_{a_z}^{out}$ for cubic boxes of different sizes that are centered at the origin, again at the

time $t \approx 37$ kyr for both the 0° and 90° cases with the same initial $\lambda = 4$. The main difference is the strength of outflows, which are stronger in the aligned case than in the orthogonal case. This morphological difference is obvious from the column density map and velocity field shown in Fig. 5-9 in § 5.3.4 below.

The absence of prominent magnetically-driven outflows in the orthogonal case helps to maintain a bulk of mass along with their angular momentum to reside near the binaries, lifting the positive change of the angular momentum in the region between 2×10^{15} cm and 1×10^{16} cm. Recall that the similar region also yields a larger mass inflow in the 90° case.

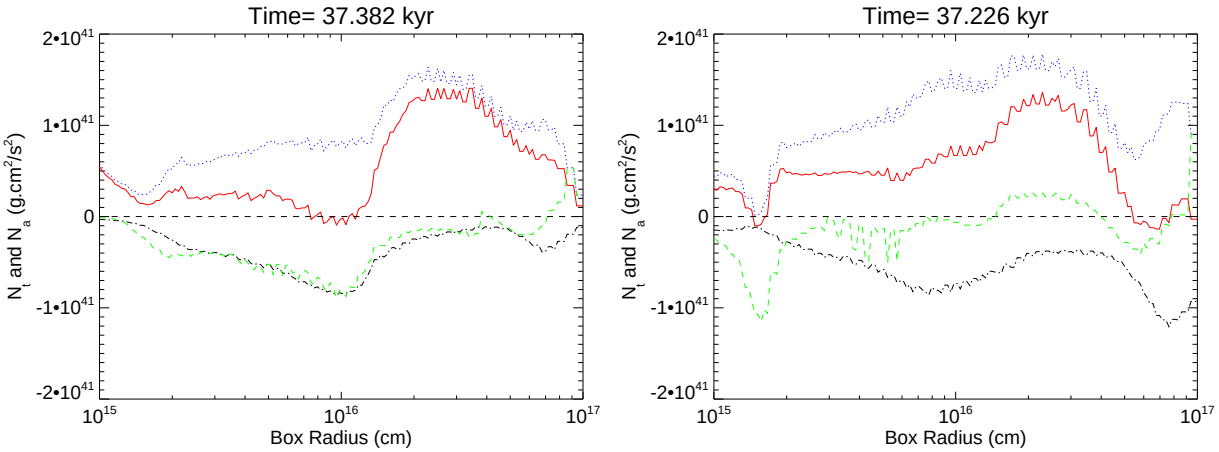

Fig. 5-6.— The magnetic (black dash-dotted) and advective (blue dotted) torque and the sum of the two (red) for cubic boxes of different half-width b for the $\lambda = 4$ case, at a representative time $t \approx 37$ kyr. The outflow component of the advective torque is shown in green dashed curve. Left panel is the aligned case (0°) and the right panel is the orthogonal case (90°). A positive torque increases the angular momentum within a volume whereas a negative one decreases it.

Interestingly, the magnetic torque is not smaller at all radii when the field is tilted 90°. At large radii ($\gtrsim 5 \times 10^{16}$ cm), the orthogonal rotator, produces a stronger magnetic torque (see Mouschovias & Paleologou 1979) than the one in the aligned rotator. The reverse is true as one moves to the inner region ranging from $\sim 1 \times 10^{16}$ cm to $\sim 5 \times 10^{16}$ cm (Mouschovias 1991). Moreover, the magnetic torque inside

the innermost $\sim 8 \times 10^{15}$ cm ≈ 600 AU region is comparable for both the aligned and orthogonal cases, which somewhat contradicts the results of Joos et al. (2012). In other words, the magnetic braking is more efficient in outer regions of the core, but weaker close in, for the larger misalignment cases. Therefore, as the gas makes its way onto the binary stars when the field misalignment is large, the gas first loses more angular momentum relative to the aligned case, and then loses less closer in, because of both weaker magnetic braking and lack of magnetically-driven outflow. This is also consistent with the distribution of gas specific angular momentum shown in Fig.5-7, where the orthogonal case is below the aligned case in the outer region, and yet the opposite is true in the inner region. These subtle competing mechanisms explain the broad similarity in the binary orbital angular momentum we present in Fig. 5-3.

5.3.4 Disk and Outflow

The misalignment between the magnetic field and the rotation axis has a noticeable effect on the disk morphology as well. In the aligned cases, ZL13 showed that strong magnetic braking produces non-Keplerian pseudo-disks in the circumbinary region (for λ less than about 8). In contrast, we find near-Keplerian circumbinary disks in cases with large field misalignment, even for mass-to-flux ratios as small as $\lambda \sim 4$. Fig. 5-8 plots the distribution of azimuthal velocity v_ϕ on the equator along the midline of the two seeds, where the orthogonal case shows a ~ 400 AU (6×10^{15} cm) size disk that follows the estimated Keplerian curve[3] in the circumbinary region. The same region is occupied by sub-Keplerian structures in the aligned case for the same level of magnetization ($\lambda = 4$). Note that the strength of magnetic torque does not differ much in both cases across 10^2 AU scale (see Fig. 5-6). However, the large DEMS (Decouple-Enabled Magnetic Structures, about $\lesssim 400$ AU in size at $t \sim 37$ kyr) destroys any rotationally-supported structure, which is an unavoidable

[3]Only the mass of the binary stars is used for calculating the Keplerian profile

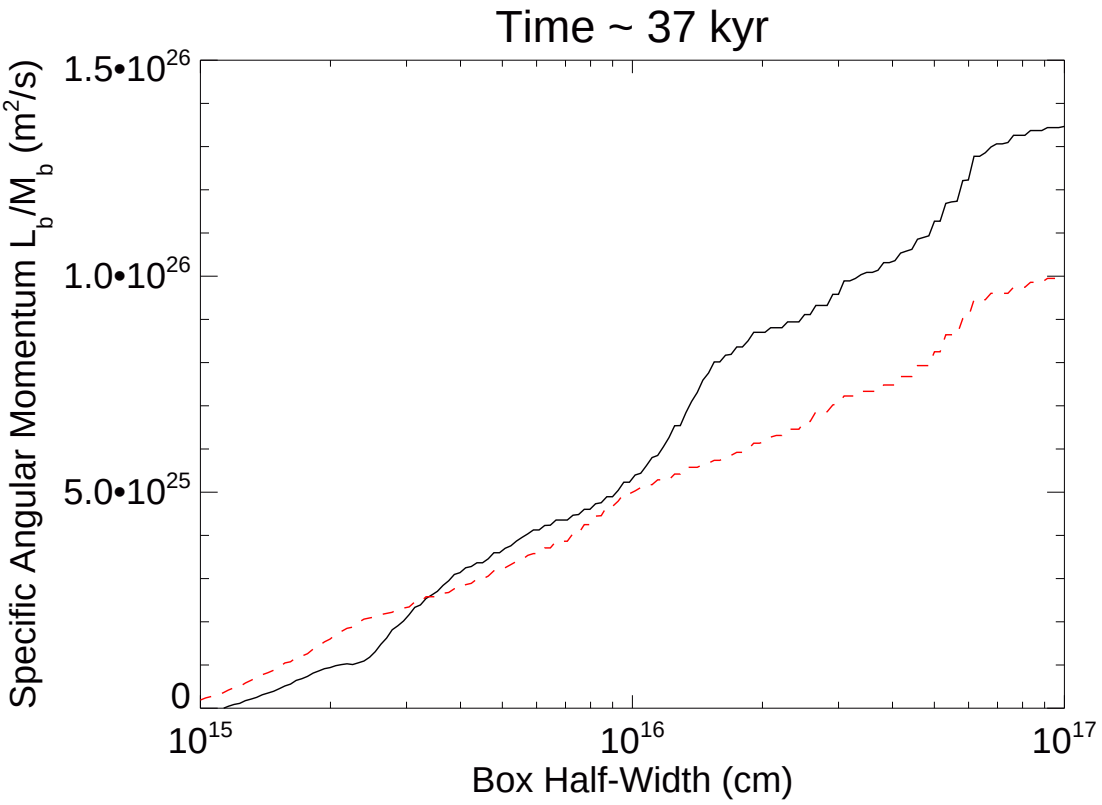

Fig. 5-7.— The integrated gas specific angular momentum. The aligned case is shown in black solid curve while the orthogonal case is in red dashed. Both are for $\lambda = 4$ case, at a representative time $t \approx 37$ kyr.

magnetically-dominated feature when field is aligned with the rotation axis (Zhao et al. 2011; Krasnopolsky et al. 2012).

The DEMS also account for the survival of circumstellar disks. In ZL13, we find that circumstellar disks are suppressed even for relatively weak magnetic field (λ less than about 16), as soon as DEMS dominate the inner region close to the binary stars. As we tilt the magnetic field, the DEMS become less prominent. Hence the circumstellar disks start to survive even for $\lambda = 8$ with tilt angle $\theta_0 = 45°$, and for the early time of $\lambda = 4$ with $\theta_0 = 90°$ when the magnetic tension force is relatively weak. The effect of field misalignment on the DEMS is also obvious by comparing the right column plots in Fig. 5-9. Our study shows that large misalignment between the mag-

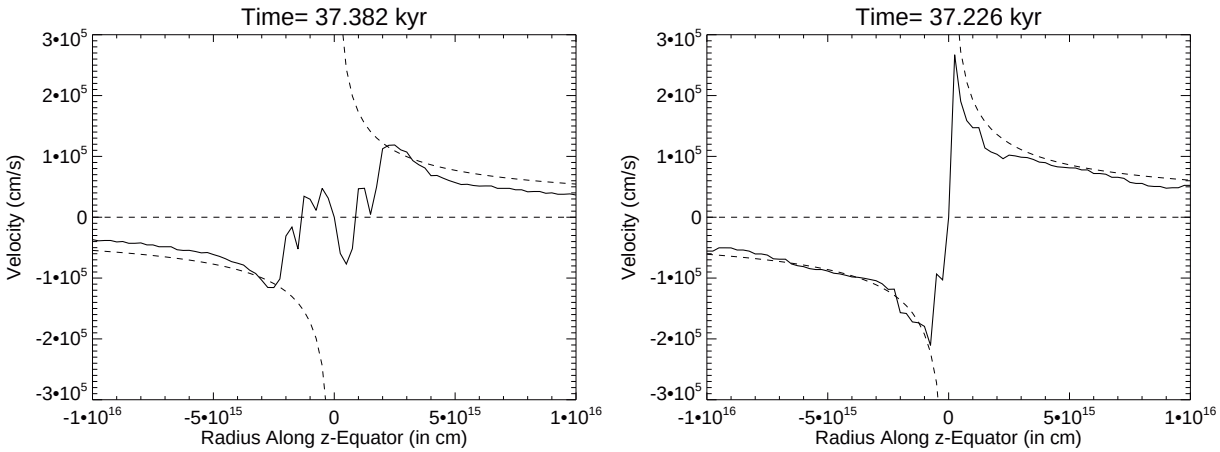

Fig. 5-8.— The distribution of azimuthal velocity on the equator along the midline of two binary seeds for the $\lambda = 4$ cases, at a representative time $t \approx 37$ kyr. Left panel is the aligned case and right being the orthogonal case. The estimated Keplerian profile is shown in dashed curve.

netic field and rotation axis can prevent the magnetic dominated structures (DEMS) from emerging in the central $\sim 10^2$ AU region - the cradle of infant protostellar and protobinary disks.

Fig. 5-9 (left column) also shows the effect of field misalignment on outflow structures, which is consistent with our discussion so far and Fig. 5-6. We do not observe any obvious outflow structure in the orthogonal cases. The aligned case has large magnetically-driven outflow launching regions both above and below the equator (see also ZL13). The same regions are dominated by gas infall for the orthogonal case. Interestingly, there are two prominent spirals in the face-on view (lower-right panel); in 3D, they are the snail-shell like structures discussed in Li et al. (2013).

5.3.5 Mass Ratio

Besides orbital separation, another fundamental quantity that characterizes a binary system is the mass ratio $q = M_2/M_1$ (M_1 and M_2 are the mass of the primary and secondary, respectively). We have previously shown that the mass ratio is strongly

affected by magnetic braking in the aligned case (ZL13). In particular, we found that the magnetic braking can slow down or even eliminate the increase of q (e.g. growth towards equal mass) with time for initially unequal mass binaries by weakening or suppressing the preferential mass accretion onto the secondary. We have carried out calculations similar to ZL13 for unequal binaries of initial $q = 0.25$ but with both $\theta_0 = 0^\circ$ and 90°. Fig. 5-10 compares the time evolution of mass ratio q for both the aligned and orthogonal cases for different values of mass-to-flux ratio λ. It is clear that tilting the magnetic field not only suppresses the accretion onto the secondary compared to the hydrodynamic case, but can also increase the accretion onto the primary compared to the aligned case. In the strongest field case of $\lambda = 2$, the mass ratio actually decreases with time, the opposite of what one may expect based on hydrodynamical simulations (Bate & Bonnell 1997; Kratter et al. 2010; ZL13). It therefore appears that magnetic misalignment makes it easier for highly uneven mass binaries to preserve their initial mass ratios during the protostellar mass accretion phase. Why this is the case is unclear; it deserves further investigation, which is beyond the scope of this Chapter.

5.4 Summary and Discussion

In this Chapter, we have investigated numerically the effect of misalignment between the magnetic field and rotation axis on protobinary evolution during the mass accretion phase, in direct comparison to our previous calculations with aligned magnetic field (Zhao & Li 2013 and Chapter 4). We have found that a misaligned magnetic field is more efficient than the aligned field at tightening the binary separation. The fundamental reason is that field misalignment suppresses the magnetically-driven outflows. This suppression has three consequences. First, the weaker gas outflow allows more of the infalling gas to accrete onto the binary stars, which increases the binary mass relative to the aligned field case. Secondly, the weaker magnetically-driven outflow

carries away less angular momentum from the infalling gas in the midplane. This second effect on its own would lead to wider binary orbits. However, there exists a competing mechanism where the same parcel of gas at larger radii has experienced stronger magnetic braking when field misalignment is greater. Thus the excess accreted gas provides only slightly bigger total angular momentum to the binary orbit. Thus the magnetic field misalignment allows faster mass accretion accompanied by a much smaller increase in angular momentum. Thus the binary separations in all misaligned runs are smaller than their counterparts in Zhao & Li (2013).

The efficient tightening of the binary orbit by magnetic field misalignment lowers the field strength required for the same degree of migration. As mentioned in the introduction, the distribution of binary orbital separations during the earliest Class 0 phase of star formation may differ from those at later times. In particular, there may exist a gap free of Class 0 binaries with separations between $150 - 550$ AU (Maury et al. 2010; Enoch et al. 2011), which is not present in the Class I or later phases[4]. We previously showed that magnetic braking is an efficient way of migrating protobinaries born on wider orbits into this apparent separation gap (Zhao & Li 2013). The results presented here indicate that to reach the same level of migration as in the aligned field cases, one may only require a magnetic field that is half as strong if it is misaligned with the rotation axis.

Our proposed mechanism of binary migration due to a tilted magnetic field may be favorable in the context of disk formation in magnetized prestellar cores. Recent numerical work has shown that rotationally supported disks may form under the combination of low magnetic field strengths and large field misalignment (Li et al. 2013; Joos et al. 2012; Krumholz et al. 2013). The CARMA sample of Hull et al. (2013) shows that the distribution of the angle between the magnetic field and jet/rotation axis is consistent with being random. This would indicate that in 50% of the sources the two axes are misaligned by a large angle ($\gtrsim 60^\circ$). If true, the large misalign-

[4]A recent SMA survey by Chen et al. (2013) finds more evidence for Class 0 binarity, but a few of the apparent multiple systems may not evolve into binaries based on their sensitivity and resolution.

ment would allow disk formation in moderately (λ greater than about 4) magnetized prestellar cores (Li et al. 2013). Therefore for cores that form binary systems, the misaligned and weaker magnetic field would enable efficient migration to fill the gap observed in Maury et al. (2010), while still allowing for the formation of 10^2-AU scale disks in the Class 0 phase. Furthermore, the survival of rotationally-supported circumbinary disks through tilting the magnetic field could explain some recent SMA and ALMA binary observations. Takakuwa et al. (2012) identify a circumbinary disk with possible spiral structures around protobinary system L1551 NE, which may arise from local perturbations due to magnetic field misalignment or supersonic turbulence. We will discuss the effects of turbulence in a future study.

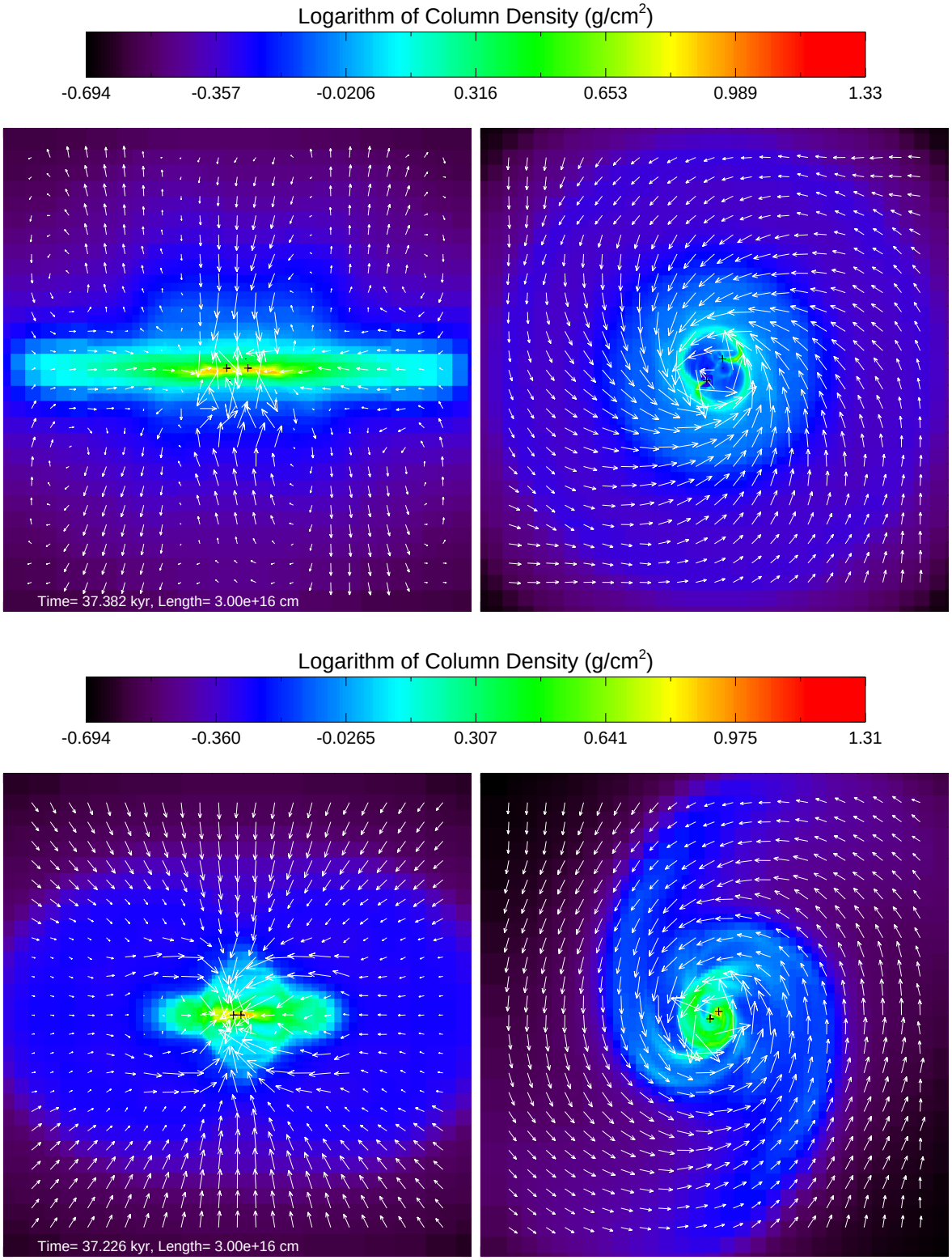

Fig. 5-9.— The column density and velocity field in both edge-on (left panels) and face-on (right) view for the $\lambda = 4$ cases, at a representative time $t \approx 37$ kyr. Upper panel is the aligned case and bottom being the orthogonal case. The length of region is 3×10^{16} cm.

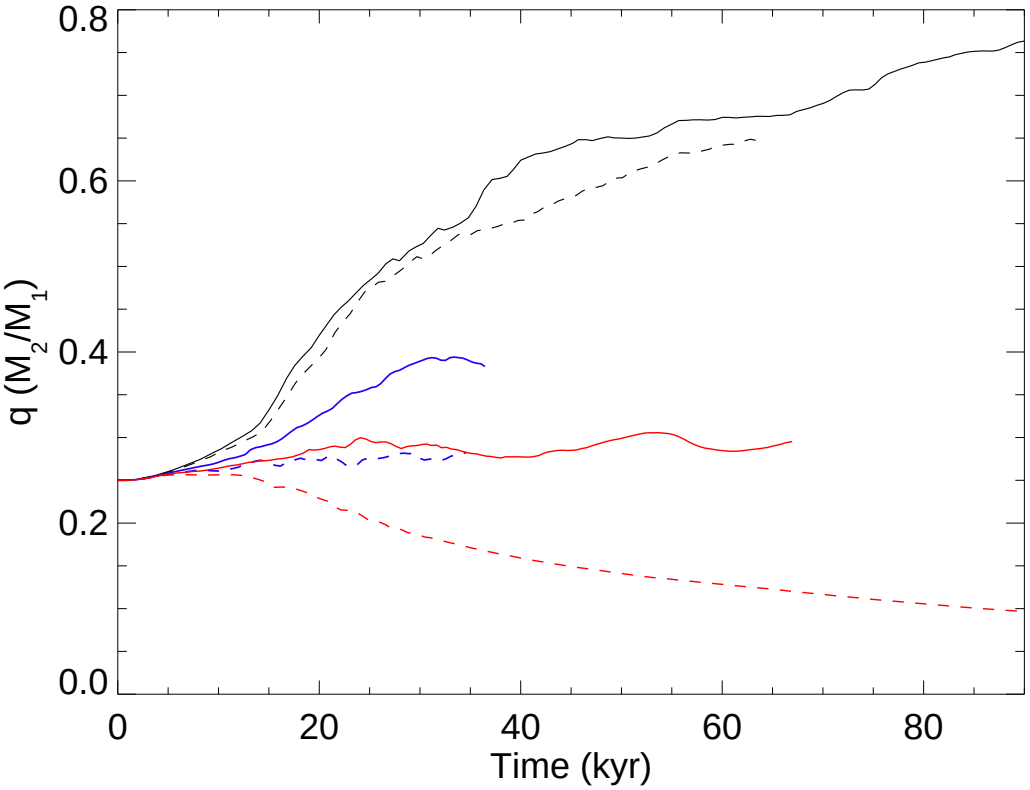

Fig. 5-10.— Evolution of mass ratio for an initially unequal mass binary of $q = 0.25$. Aligned cases are shown in solid lines and orthogonal cases are in dashed curves. The black, blue and red lines are for $\lambda = 32$, 4, and 2, respectively.

Chapter 6

Magnetized Binary Formation from Prestellar Core Collapse to Protobinary Evolution: Preliminary Results

6.1 Introduction

The formation of binaries and higher-order multiples is considered the dominant channel of star formation. As discussed in Chapter 1, at least half of all stars in the Galaxy reside in multiple systems (e.g., Duquennoy & Mayor 1991; Raghavan et al. 2010; Janson et al. 2012). The fraction is even higher for young stellar objects (e.g., Duchêne et al. 2007). Among all observed multiple systems, about three-quarters are binaries, which provides a strong motivation to study them. Despite the undisputed importance of binaries and multiples, the observed statistical properties of such stellar systems are not fully understood. Robust theory and computation are required to explain their origins.

The key properties that define a binary system are its orbital separation, mass ratio, and orbital eccentricity. The observed distribution of each property is rather broad and flat, which must be explained by a complete star formation theory.

The distribution of binary separation for main-sequence stars in the Galactic field is known to be extremely wide (0.01 AU $\lesssim r \lesssim 10^4$ AU), usually modeled as a log-normal with a mean at $\sim$ 45 AU (Goodwin et al. 2007; Duchêne & Kraus 2013). About one-third of these systems have separations less than about 1 AU. A similar distribution is also found for young stars in star-forming regions. For the more evolved T-Tauri stars, the distribution of orbital separation is consistent with both a broad log-normal distribution (e.g. Mathieu 1994; Kraus et al. 2011) and a slowly declining power-law distribution (e.g., King et al. 2012a). The maximum separation may vary with environments (e.g. dense clusters) and stellar mass (Kraus & Hillenbrand 2012). For Class I protostars that are still embedded in their envelope, the distribution of projected separation is consistent with Öpik's power law (Öpik 1924) out to 5000 AU. The Class 0 sources tend to show a deficit in binaries with separation from 50 to 1500 AU (Maury et al. 2010; Enoch et al. 2011), however the conclusion is not definitive because of the limited sample size.

The mass ratio, $q = M_{sec}/M_{prim} \leq 1$, can generally be derived from the observed flux ratio. Its distribution for solar-type binaries in the Galactic field is almost flat down to $q \approx 0.1$, although there is a marginally significant peak at $q \gtrsim 0.95$ according to Raghavan et al. (2010). However, the situation is more subtle because the mass ratio distribution depends on the primary's mass and the binary separation. Binaries with separations closer than the mean are characterized by a strong peak at $q \approx 1$, whereas the wider binaries have a single peak around $q \approx 0.3$. Surveys of pre-main-sequence stars show a more or less flat distribution of binary mass ratio. The deeply embedded Class 0 and Class I sources lack a well established distribution of binary mass ratio, because of observational limitations.

The binary orbital eccentricity is another important parameter to characterize the system. The expected distribution for a dynamically relaxed ("thermal") population is $f(e) = 2e$ (Ambartsumian 1937). However, the observed eccentricity distribution is essentially flat beyond a period of ~ 100 days. It can be modeled as a broad Gaussian distribution centered at $\bar{e} \approx 0.4$, because of somewhat fewer high-eccentricity systems (Stepinski & Black 2001). In any case, observations of binary eccentricity are inconsistent with the "thermal" distribution.

All three key properties that characterize a binary system have rather broad and flat statistical distributions, which is difficult to explain by existing theoretical studies. Intriguingly, Bate (2012) simulated the formation of a star cluster using a radiative SPH code, which produced binaries and multiple systems with statistic properties that are nearly indistinguishable from the observed systems. In particular, the simulated binaries have a wide range of separation (from 1 AU to 10^4 AU), even though all of them started out with initial separations of order 10 AU. The orbits of some of the binaries are tightened up through interaction with a circumbinary disk or decay of unstable multiple systems. It is tempting to conclude that the problem of binary formation is essentially solved.

The apparent agreement of Bate's results with observations may be fortuitous,

however. As stressed in the recent review of Clarke (2012), his simulation ignored the magnetic field, whose existence in star forming regions is undeniable (e.g. Ward-Thompson 2000; Girart et al. 2006). Theoretically, magnetic fields are dynamically important to binary formation through redistributing angular momentum and driving outflows; they strongly shape the property of binary systems formed in dense cores, as we demonstrated in Chapters 3, 4 and 5 (Zhao & Li 2013; Zhao et al. 2013). There have been several previous studies of the effects of the magnetic field on binary formation through core fragmentation. Most of them are, however, limited to the initial fragmentation phase leading to the formation of two seed protostars (Price & Bate 2007; Hennebelle & Teyssier 2008; Machida et al. 2008). The preliminary investigation presented in this Chapter aims at remedying this deficiency.

Core fragmentation simulations usually start with a $\sim 1\,\mathrm{M}_{\odot}$ dense core that has an $m = 2$ mode perturbation on the initial density distribution (similar to the set-up of Boss & Bodenheimer (1979)). If massive enough, the core can become Jeans unstable on two well-separated density peaks early in the isothermal collapse. Machida et al. (2008) showed that the initial separation of the binary seeds produced in magnetized cores is controlled mainly by the ratio of rotational and magnetic energies. If the magnetic field is strong enough, it can suppress the core fragmentation completely, leading to a potential "crisis" for binary formation (see also Price & Bate 2007, Hennebelle & Teyssier 2008). If the initial amplitude of density perturbation is large enough (of order 50%), binary seeds can be produced even for a realistic magnetic field (Troland & Crutcher 2008). However, these calculations either stop or become dominated by numerical artifacts before most of the protostellar accretion is complete. For example, in Hennebelle & Teyssier (2008), the computation timestep decreases dramatically soon after the binary seed formation, which prevents them from evolving the system further. Machida et al. (2008) has no sink particle treatment, and their central high density region is subject to strong artificial fragmentation. Price & Bate (2007) follows the binary orbital evolution much further, but the magnetic field is

treated incorrectly in their SPH code (using a formulation that precludes the twisting of field lines that is responsible for magnetic braking).

Despite recent progress, the theory of magnetized binary formation remains far from complete. In this Chapter, we revisit the classic problem of binary formation through core fragmentation, using the Enzo AMR MHD code described in Chapter 2. It enables us to follow both the initial fragmentation of the magnetized cores and the subsequent orbital evolution of formed protobinary systems.

6.2 Problem Setup

6.2.1 Initial and Boundary Conditions

We model the binary formation in a magnetized dense core embedded in a more diffuse ambient medium. The spherical core has a radius of $R = 1.0 \times 10^{17}$ cm (~ 0.032 pc) with an $m = 2$ perturbation on the otherwise uniform density distribution, i.e.,

$$\rho(\phi) = \rho_0(1 + A \cdot cos(m\phi)), \tag{6.1}$$

where $m = 2$ is adopted, $A = 0.5$ is the perturbation amplitude, ϕ is the azimuthal angle, and $\rho_0 = 1.25 \times 10^{-18}$g·cm^{-3}. The density profile determines the initial mass of the core ($M = 2.63\,\mathrm{M}_\odot$) and the free-fall time ($t_{ff} \approx 60$ kyrs). The dense core is embedded in a low density ambient medium ($\rho_{medium} = 1.25 \times 10^{-20}$g·cm^{-3}) that fills the rest of computational box. The gas is assumed to be isothermal initially with a temperature of $T \sim 10$K everywhere, in accordance with observations of star forming molecular clouds. Note that the box size is about 2.5 times the size of the core, which helps to reduce the influence of the periodic images that arise from the periodic boundary conditions used in the Fast-Fourier-Transformation (FFT) solver of self-gravity. These initial conditions are similar to those used by Machida et al. 2008.

To minimize numerical fragmentation in the isothermal gas, we adopt a barotropic equation of state (EOS), which mimics the isothermal EOS at low densities and the adiabatic EOS at high densities,

$$P = \rho c_s^2 \left[1 + (\frac{\rho}{\rho_{crit}})^{2/3}\right] \tag{6.2}$$

where $\rho_{crit} = 4 \times 10^{-13}$g·cm^{-3} is the transition density between the two regimes, and $c_s = 0.2$ km/s is the isothermal sound speed for $T \sim 10$ K gas. The sound speed yields a ratio of thermal to gravitational energy $\alpha \approx 0.29$ for the dense core.

The core is also initially rotating and magnetized. We impose a rigid body rotation on the core with an angular velocity of $\omega = 2.0 \times 10^{-13}$s^{-1}. This corresponds to a ratio of rotational to gravitational energy $\beta \approx 0.057$, which is within the observed range for dense cores. The initial magnetic field threading the core is uniform everywhere; its initial direction can either be parallel (0°) or perpendicular (90°) to the rotating axis. We also consider different strengths of the initial magnetic field $B_0 = 1.35 \times 10^{-4}$ G, 6.75×10^{-5} G, 3.375×10^{-5} G, and 1.6875×10^{-5} G, corresponding to a dimensionless mass-to-flux ratio (in units of the critical value $(2\pi G^{1/2})^{-1}$) of $\lambda = 2$, 4, 8, and 16 respectively. These values of λ bracket those inferred from observations, which are typically a few to several (Troland & Crutcher 2008; see Chapter 1). We should note that the above λ values are calculated for the core as a whole; the local mass-to-flux ratio near the central magnetic flux tube is somewhat larger, by a factor of 1.5. For comparison, we run a simulation without the magnetic field, denoted as the HD (hydrodynamics) case.

6.2.2 A New Solver for Sink Particle Gravity

For the purpose of this study, we developed a new gravity solver to replace the original solver in Enzo that sometimes leads to unphysical ejection of sink particles.

The original gravity solver in Enzo uses the so-called Cloud-In-Cell (CIC) method

for calculating the gravitational potential for both gas and particles. The central idea is to deposit the mass of a particle onto its surrounding eight cells prior to calculating the gravitational potential. The method works best for particles with mass that are not too large compared with the gas mass in the nearby cells. Otherwise, a sink particle of stellar mass can create a huge peak on the density field within the current computation domain. In this situation, the subsequent gravity solver can become very sensitive to numerical oscillations, which sometimes leads to unphysical values of gravitational potential and acceleration. Unfortunately, the stellar objects in our binary formation simulations can grow to large masses, creating density peaks that are not well treated by the CIC method.

To make the Enzo code more suitable for binary formation problems, we developed a new gravity solver that treats the gas and sink particles separately. In this method, we no longer deposit the particle mass onto the cells to solve for the combined gravity from the gas and sink particles. Instead, direct summation is implemented for particle-gas and particle-particle interactions. The algorithm can be expressed in terms of gravitational accelerations as follows,

$$\mathbf{a}_{gas}(\mathbf{x}) = \mathbf{a}_{field}(\mathbf{x}) + \sum_{particle\ i} \frac{GM_i(\mathbf{r}_i - \mathbf{x})}{|\mathbf{r_i} - \mathbf{x}|^3}, \tag{6.3}$$

$$\mathbf{a}_i = \mathbf{a}_{field}(\mathbf{r}_i) + \sum_{particle\ j \neq i} \frac{GM_j(\mathbf{r}_j - \mathbf{r}_i)}{|\mathbf{r}_j - \mathbf{r}_i|^3}, \tag{6.4}$$

where $\mathbf{a}_{gas}$ and $\mathbf{a}_i$ are the accelerations for gas cell at position $\mathbf{x}$ and the i-th sink particle at position $\mathbf{r}_i$ respectively; a_{field} denotes the acceleration field calculated from the multi-grid or FFT solver in previous steps, G is the gravitational constant, and M_i is the mass of the i-th sink particle; Thus, we first use the pure gas mass distribution to obtain the acceleration field a_{field} over the computational domain, and the sink particle contributions are added to derive the final accelerations for either particles or gas components. The numerical steps of this new method are summarized below,

```
EvolveLevel(level, ParentTime)
      SetBoundaryValues
      while (Time < ParentTime):
          dt = ComputeTimeStep(level)
          PrepareDensityField(dt, GasOnly)
          ComputePotentialFieldFFT(level=0)
          MultiGridSolverForPotential(level)
          ComputeAccelerations(level)
          {
             for every grid on this level
             ComputeAccelerationField(GasOnly)
             if GAS
                Accl_Gas = GasAccelerationField +
                           DirectSummationFromAllParticles
             if PARTICLE_i
                Accl_i=InterpolateAccelerationField_ParticleLocation +
                       DirectSummationOverParticles(j != i)
          }
          SolveHydroEquations(dt)
          SolveOtherEquations(dt)
          UpdateParticlePositions
          SinkParticleCreation+Accretion+Merging
          SetBoundaryValues
          CommunicationAllParticles
          EvolveLevel(level+1, Time)
          Time = Time + dt
          FluxCorrection
          Projection
```

```
RebuildHierarchy(level+1)
```

Currently, we are testing the new gravity solver in a variety of circumstances. We find that it is a good remedy for the unphysical star ejection that occasionally happens when using the original gravity solver. The method is not suitable, however, in the early phase of the simulations when the masses of the star particles are small. Part of the reason is that the self-gravity of the gas surrounding the (low-mass) sink particle can dominate that of the particle itself, which produces some inconsistency between the particle orbit and the location of local density peak. This inconsistency requires further investigation in the future. In the meantime, we have decided to use the original solver to follow the early collapse and fragmentation; when the unphysical star ejection occurs, we switch to the new gravity solver and continue the simulation.

6.3 Results

We carry out a total of nine simulations, varying the initial magnetic field strengths ($\lambda = 2, 4, 8, 16$) and orientations ($0°$ and $90°$ relative to the rotation axis). Table 6.1 summarizes our preliminary results.

Table 6.1: Models and Basic Results

λ	α	Binary Merged	Circumstellar Disk
2	$0°$	Yes	No
	$90°$	No	No
4	$0°$	Yes	No
	$90°$	No	No
8	$0°$	No	No
	$90°$	No	Yes
16	$0°$	No	Yes
	$90°$	No	Yes
HD	/	No	Yes

Note that the core fragmentation into binary seeds does occur in every case, because of the large perturbation amplitude $A = 0.5$ on the initial density distribution.

We have also tested the models with smaller amplitude $A = 0.2$, $A = 0.3$, and found that the fragmentation is inhibited in cases of strong magnetization ($\lambda \leq 4$). This result is in good agreement with previous studies (e.g. Hennebelle & Teyssier 2008).

6.3.1 Magnetic Braking and Initial Fragmentation

We first present the qualitative effects of the magnetic field on the protobinary properties based on our preliminary results. In Fig. 6-1, 6-2, 6-3, 6-4, and 6-5, we show the snapshots in the field-rotation aligned (0°) cases when the binary seeds reach their first close approach. Except for the HD and $\lambda = 16$ cases, the binary separation at the first close approach is well-below 100 AU. It is an order of magnitude smaller than the initial separation at the time of their formation, which is more than 2000 AU. Such a large decline in separation can be caused both by the much shorter free-fall timescale than the orbital timescale, and by the removal of binary orbital angular momentum. However, the former factor is only able to reduce the binary separation down to about 200 AU, as in the HD case. To reach down to the tens of AU range, additional mechanisms are required to reduce the binary orbital angular momentum.

The main mechanisms to efficiently transport angular momentum are the magnetic torque and gravitational torque. In the strongly magnetized cases, $\lambda = 2$ and 4, the circumbinary regions have very little density enhancement, which limits the effect of gravitational torques. On the other hand, magnetic torques can significantly affect the binary orbital angular momentum through magnetic braking. As discussed in our previous papers (Zhao & Li 2013; Zhao et al. 2013) and in previous Chapters, magnetic braking constantly removes the angular momentum of the rotating gas that would later be accreted onto the binary stars, leading to a binary system with a lower orbital angular momentum and tighter separation. The same mechanism operates in the early binary fragmentation phase as well. From birth to the first close approach, each binary seed keeps accreting at a rate as high as $\sim 10^{-5}\,\mathrm{M}_{\odot}/yr$ (see Fig. 6-7).

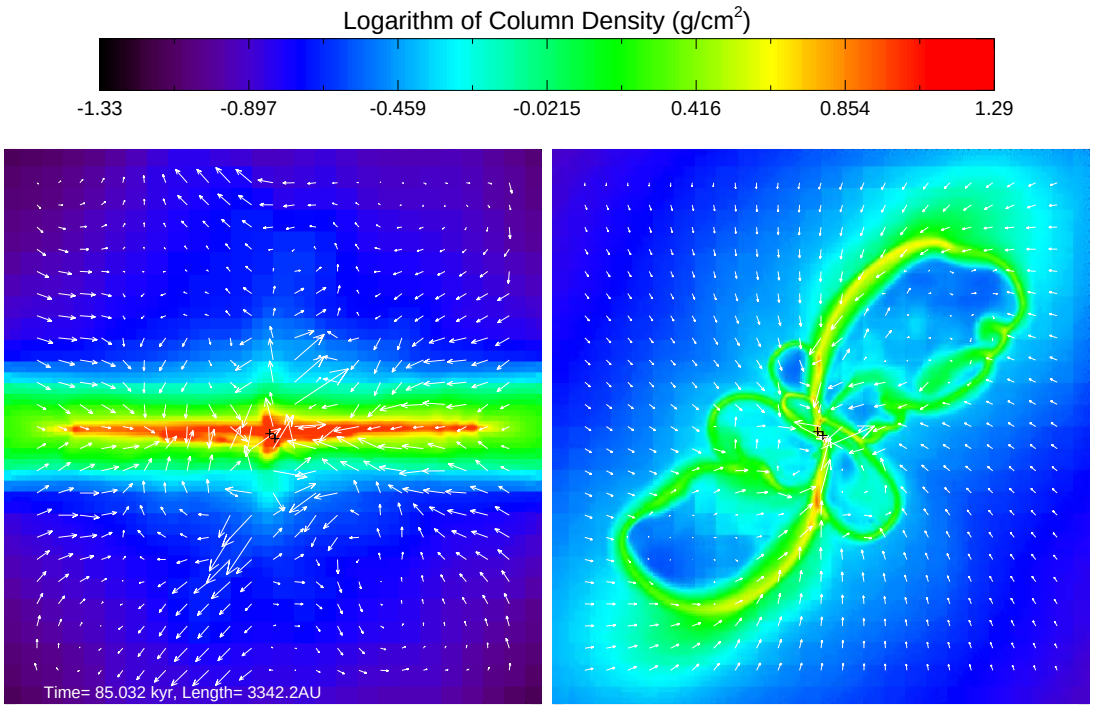

Fig. 6-1.— The logarithmic distribution of the column density Σ (in $g \cdot cm^{-2}$) for the aligned (0°) $\lambda = 2$ case at the first close approach of the binary stars. Left panel, edge-on view. Right panel, face-on view.

Hence, as the cloud collapse proceeds, the binaries continue to accrete gas whose angular momentum is reduced via magnetic braking. We tentatively conclude that magnetic braking is the main reason for the difference in binary separation at first close approach between the HD case and the strongly magnetized cases [1].

Note that after the first close approach, two runs (0°: $\lambda = 2$ and $\lambda = 4$ case) show a binary separation below ~ 10 AU; we cannot accurately follow their evolution further in time, because of a lack of resolution for the gravity solver. Such systems are "effectively" merged.

[1]The 90° cases have qualitatively similar results, except for the flow morphology such as outflow structures.

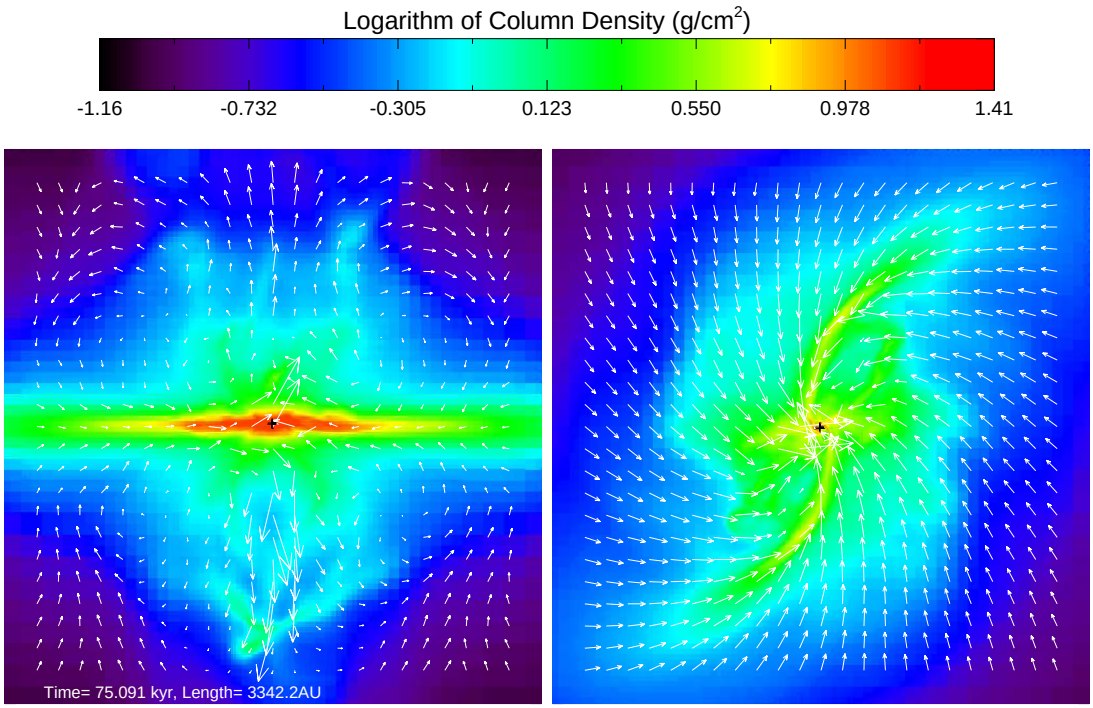

Fig. 6-2.— Same as Fig. 6-1, but for $\lambda = 4$, 0° case.

6.3.2 Orbital Evolution and Protobinary Properties

Our simulations have all run beyond one-free fall time. In some cases, the binary stars have revolved around each other several times during their main accretion phase. However, using the original gravity solver, the star particles occasionally get ejected in some random direction, as discussed in § 6.2.2. To get around this numerical problem, we use our newly-developed gravity solver for sink particles to restart the simulation right before the ejection. Fig. 6-6 shows that the star ejection no longer occurs after adopting the new gravity solver.

Currently, our analysis for the binary properties is limited by the number of output frames. We are waiting for more results from the restarted simulations with the new gravity solver. As a result, the following analysis of the evolution of basic binary quantities (including the binary mass, separation, and mass ratio) is preliminary.

Fig. 6-7 shows that the binary mass grows quickly even before the time of first

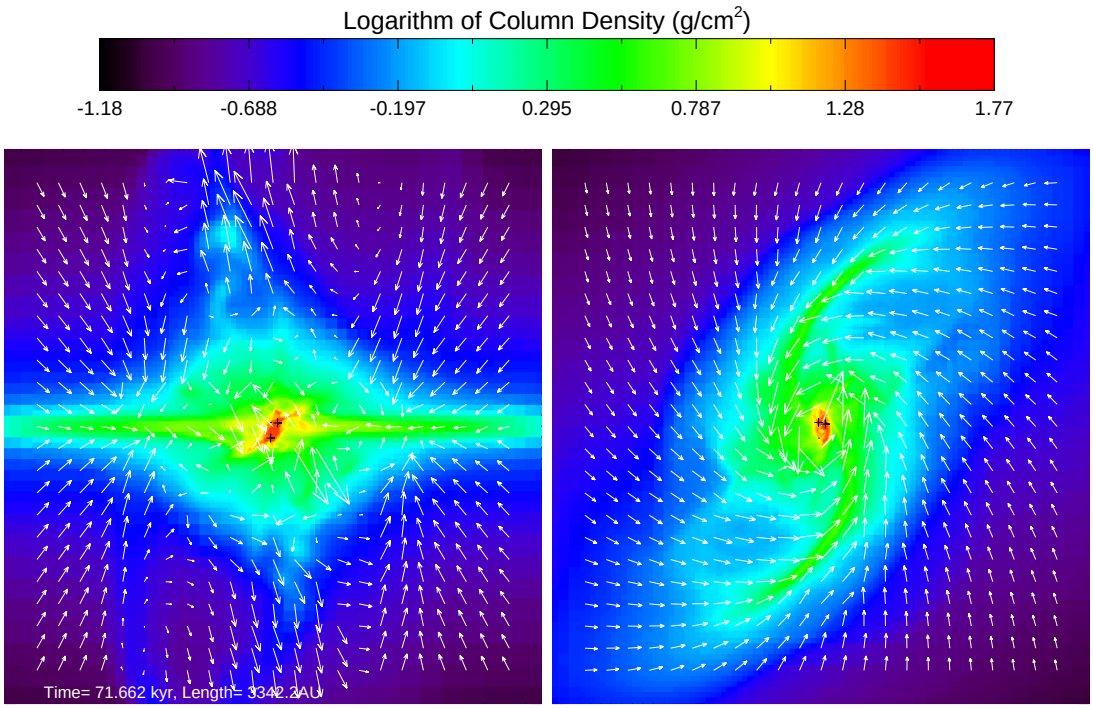

Fig. 6-3.— Same as Fig. 6-1, but for $\lambda = 8$, 0° case.

close approach. Two binary seeds are created relatively far apart right around $1t_{ff}$ with an initial mass $\lesssim 0.05\,M_\odot$ each. They then follow the collapse of the cloud inward, and grow with a rapid accretion rate of $\dot{M} \sim 10^{-5}\,M_\odot/yr$. The mass growth later flattens as the binaries move further inward ($\lesssim$ 1000 AU), possibly because of the pressure near the centrifugal barrier or the magnetic structures (e.g. DEMS) reduces the gas infall rate. The decrease in accretion rate is also seen in the single star case shown in Fig. 3-1. Fig. 6-7 also shows that strong magnetic fields can delay the collapse process in terms of the sink particle creation, which appears much later in the $\lambda = 2$ case. Note that in the 90° magnetic runs, the binary mass grows faster than that of the HD case and the 0° cases. This is consistent with the results presented in Chapter 5 (see also Zhao et al. 2013), where we show a large magnetic field misalignment helps suppress outflows and promote stellar mass growth.

Our result shows that the initial binary orbit is highly eccentric for all cases, and

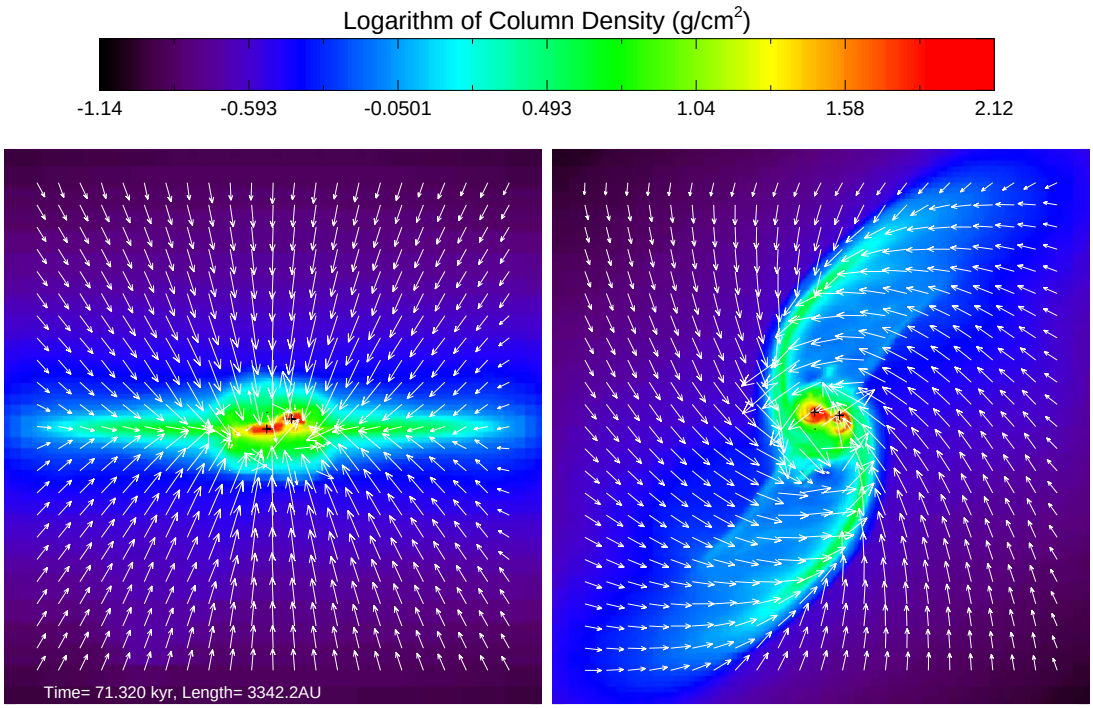

Fig. 6-4.— Same as Fig. 6-1, but for $\lambda = 16$, 0° case.

that the binary can survive the first close approach if the magnetic field is not too strong. Fig. 6-8, shows that the initial binary separation is about 2300 AU when the seeds are first created. The two stars then move rapidly closer with the free-fall collapse of the core; the initial rate of orbital shrinkage depends little on the magnetic field strength. In all cases, the initial binary orbit has an eccentricity close to 1. However, in aligned strongly magnetized cases (0°: $\lambda = 4$ and $\lambda = 2$ cases), the two stars are likely to merge at the first close approach. In all other cases, the binary survives and evolves with an eccentric orbit. Particularly, the case of $\lambda = 8$ and 90° has evolved twice as long as other cases, covering more than ten full orbits. The eccentric nature of the orbits shows up in the periodic wiggles on the curves. The effect of the magnetic field on the subsequent evolution of binary separation is consistent with the result of Zhao & Li 2013; that is, stronger magnetic fields tend to tighten the binary separations more.

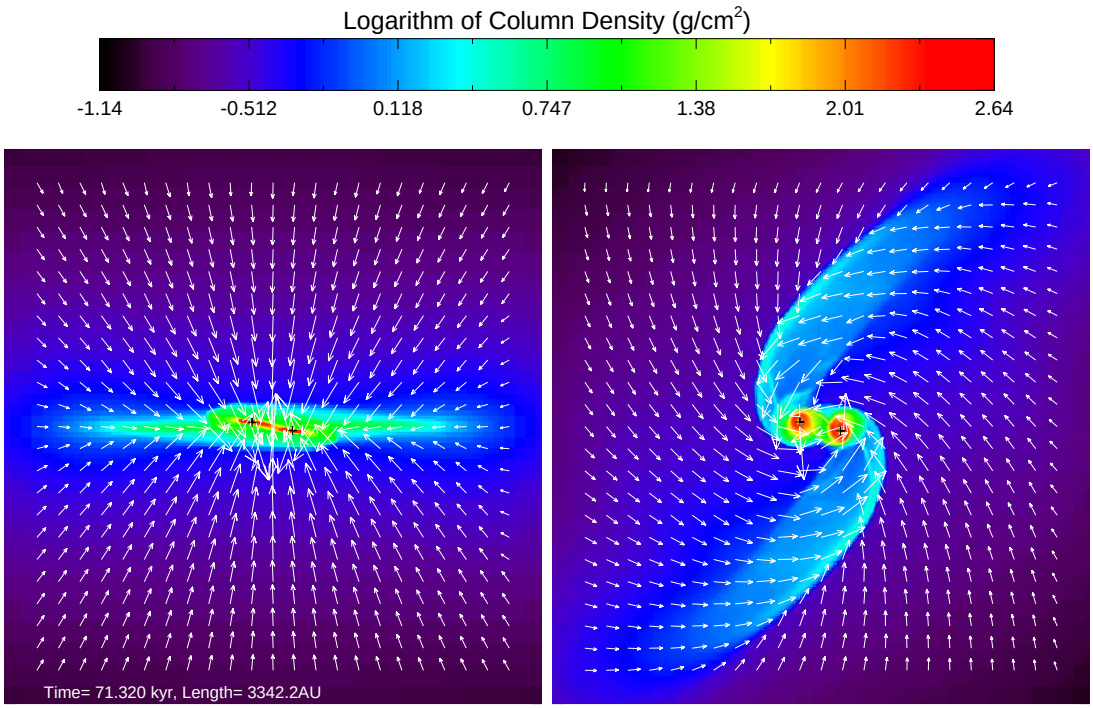

Fig. 6-5.— Same as Fig. 6-1, but for the non-magnetized HD case.

Finally, the mass ratio evolution (Fig. 6-9) shows that the binary components have roughly similar masses over time, with some variations across different degrees of magnetization. It is expected since the initial core fragmentation tends to produce two equal mass binary pairs to begin with; their mass should grow at a similar rate. We will leave more detailed analysis of the existing models and exploration of more complicated models to future studies.

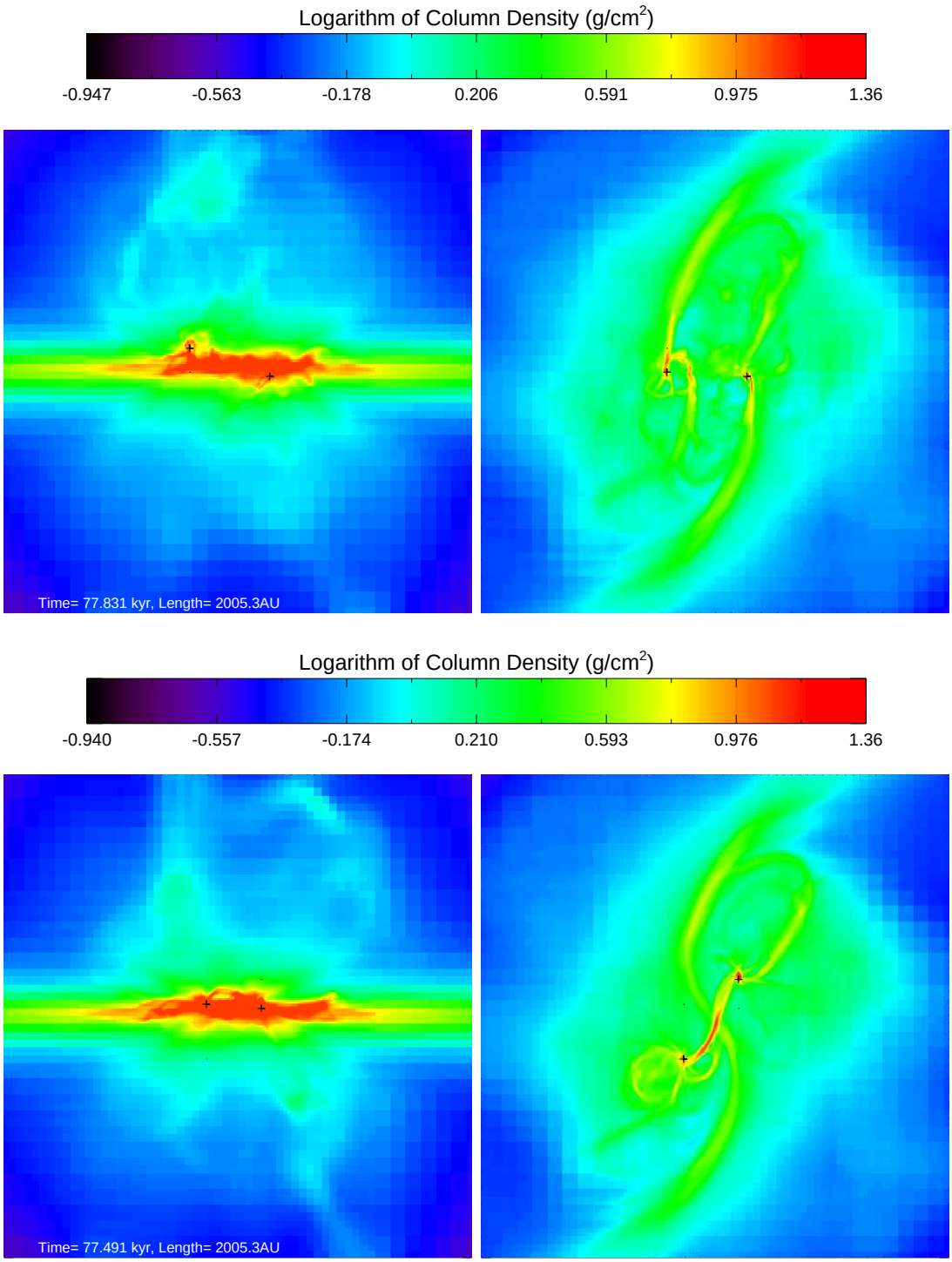

Fig. 6-6.— Compare two gravity solvers at similar time $t \approx 77.5kyr$. Upper panel: the star on the left starts to be ejected vertically using the original Enzo gravity solver. Lower panel: no star ejection occurs with the new gravity solver. Both figures show the logarithmic distribution of the column density Σ (in $g \cdot cm^{-2}$) for the aligned ($0°$) $\lambda = 4$ case with edge-on (left) and face-on views (right).

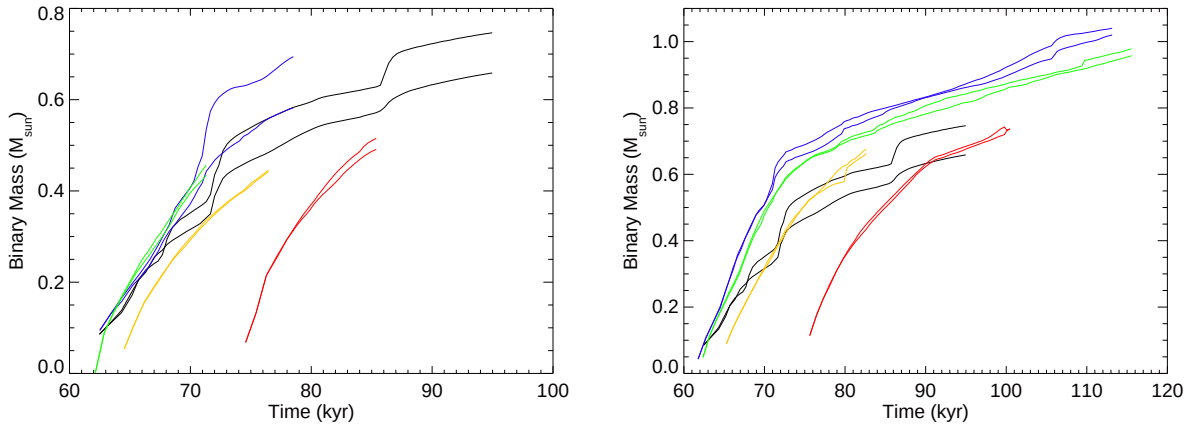

Fig. 6-7.— Stellar mass (in solar units) growth for HD (black), $\lambda = 16$ (blue), $\lambda = 8$ (green), $\lambda = 4$ (yellow), $\lambda = 2$ (red) cases. Left panel are 0° cases, and right 90° cases.

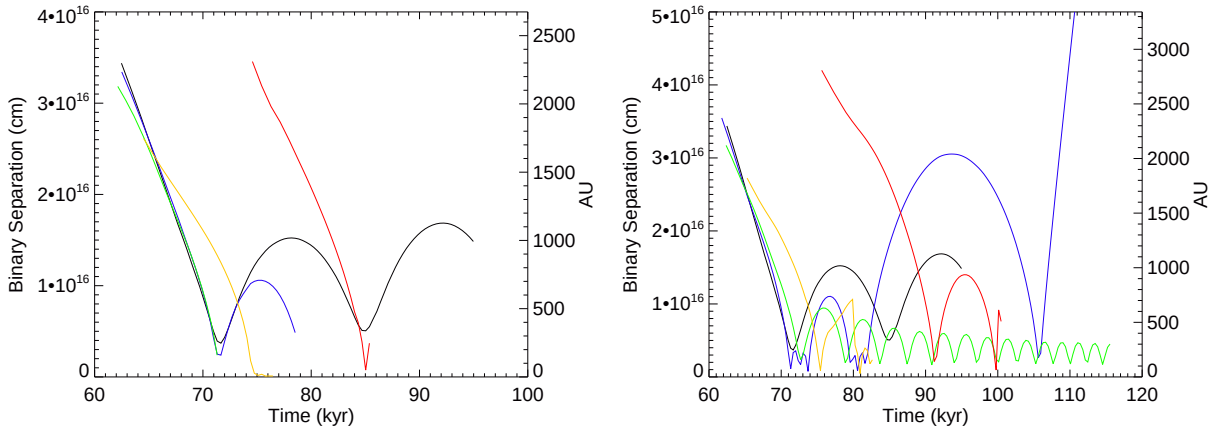

Fig. 6-8.— Evolution of binary separation with time for HD (black), $\lambda = 16$ (blue), $\lambda = 8$ (green), $\lambda = 4$ (yellow), $\lambda = 2$ (red) cases. Left panel are 0° cases, and right 90° cases.

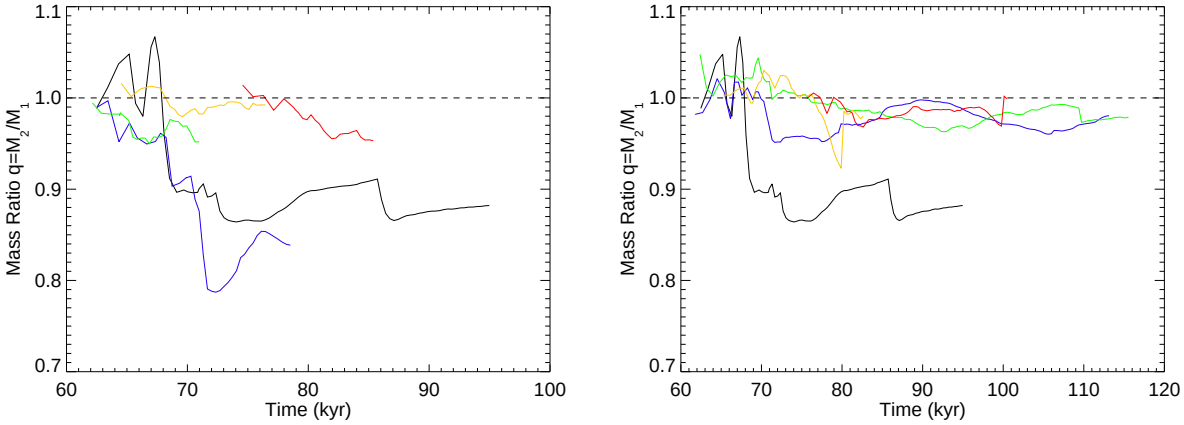

Fig. 6-9.— Evolution of the protobinary mass ratio q with time for HD (black), $\lambda = 16$ (blue), $\lambda = 8$ (green), $\lambda = 4$ (yellow), $\lambda = 2$ (red) cases. Left panel are 0° cases, and right 90° cases.

Chapter 7

Summary and Outlook

7.1 Summary

This thesis presents a systematic study of the formation of binary stars from dense cores of molecular cloud, with a particular focus on the effect of the magnetic field. We divide the formation of binaries into two conceptually distinct phases: the prestellar core evolution phase leading to the formation of two binary seeds and protostellar mass accretion phase. We first focus on the protostellar phase and investigate the effect of the magnetic effect on protobinary properties. The study covers a large parameter space, including a wide range of magnetic field strengths and orientations. We only show the preliminary results for the full problem of binary formation and leave a more comprehensive investigation to the future. Our main results are contained in Chapters 3-6.

In Chapter 3, to make sure that the sink particle treatment was done correctly, we carried out a calculation of the collapse of a simple core with an initially uniform density and magnetic field. We find that some strongly magnetized regions in the inner part of the accretion flow are expanding outward instead of collapsing. The expansion is driven by the magnetic flux that has been dragged in by the collapsing matter but is left behind as the matter accretes onto the stellar object. The magnetic pressure builds up near the protostar and releases along the directions of least resistance, driving the expansion observed in the simulations. We termed the expanding regions as the "decoupling-enabled magnetic structure" (DEMS). It is a form of magnetic interchange instability, and is a generic feature of magnetized protostellar accretion even in the presence of non-ideal MHD effects. The DEMS plays a crucial role in protostellar disk formation. These strongly magnetized regions prevent the rotating, collapsing accretion flow from completing a full orbit around the central stellar object.

In Chapter 4, we focus on the less studied protostellar accretion phase and investigate the magnetic effects on the evolution of protobinary orbital properties. We start with a pair of binary seeds embedded in a magnetized envelope, and follow the

mass and orbital evolution of the protobinary as it accretes mass and angular momentum from the envelope. We find that a magnetic field of the observed strength is capable of removing most of the angular momentum of the material that reaches the binary. The reduction in the angular momentum of the accretion flow has two important consequences, compared to the non-magnetic case: (1) the protobinary orbit becomes much tighter and (2) the mass ratio does not increase as fast with time for initially unequal mass systems. In addition, the magnetic field drastically changes the morphology and dynamics of the structures that surround the protobinaries. It suppresses the formation of circumstellar and circumbinary disks as well as spiral arms found in the non-magnetic simulations. These structures are replaced by a bipolar magnetic-braking-driven expanding regions, a dense circumbinary pseudodisk in the equatorial region, and low-density, highly magnetized structures close to the protobinaries that expand against the pseudodisk (the DEMS).

In Chapter 5, motivated by recent observations of misaligned magnetic field with respect to the rotation axis in star forming dense cores, we simulate the effect of such field misalignment on protobinary evolution. Our simulations show unexpectedly that the binary separation is smaller in the misaligned case than in the aligned case. The reason is that the field misalignment weakens the magnetically-driven outflow, which has two competing effects on the binary separation. First, the weaker outflow carries away less angular momentum from the infalling gas, which tends to increase the binary separation, a, because it increases with the binary angular momentum L_b as $a \propto {L_b}^2$. However, the weaker outflow also allows more infalling gas to be accreted onto the binaries, which is the reason for the smaller separation in the misaligned case, because the separation a depends more strongly on the binary mass M_b (as $a \propto {M_b}^{-3}$) than on the angular momentum. Therefore, misaligned magnetic fields are more efficient in shrinking the protobinary orbits.

Finally, in Chapter 6, we study the full problem of binary formation including both the prestellar and protostellar phases. The simulation starts with a magnetized

dense core that has an $m = 2$ mode perturbation on the initial density distribution (Boss & Bodenheimer 1979). The early pre-stellar phase of isothermal collapse and fragmentation shows a good agreement with previous work. In particular, we find that even fairly strongly magnetized cores can fragment into binary seeds if the initial density perturbation is large ($A = 0.5$). The resulting binary seeds are widely separated initially and on highly eccentric orbits. We were able to go beyond the previous work and follow the binary evolution into the protostellar phase. We find that the highly eccentric binary seeds can survive at least their initial closest approach, and retain their large eccentricity, if the magnetic field is not too strong. To resolve the issue of occasional particle ejection, we developed a new gravity solver for sink particles. However, the analysis is limited by the the relative short duration of the existing simulations. Only preliminary results are presented. They form the basis of future, more comprehensive investigations.

7.2 Future Work

The thesis has demonstrated in some detail the importance of the magnetic field in star formation in general and binary formation in particular. Many open questions remain unanswered, however. These include the effects of non-ideal MHD on binary formation, and the effects of the magnetic field and outflow feedback on the statistical properties of binary and multiple systems formed in a cluster environment. I hope to embark on these challenges in my future work.

First, we will finish the analysis of Chapter 6 to obtain a more complete picture of binary formation and evolution in magnetized dense cores. With the new gravity solver in place, we can continue to follow the protobinary evolution much longer until the binary stars have accreted most of the mass in their parent core. This should enable us to perform in-depth study of both the initial fragmentation phase and the protobinary orbital evolution phase. We will be in a position to determine the effects

ofthe magnetic field on the three key parameters of a binary system (separation, mass ratio, and eccentricity) for the entire process of binary formation and evolution.

The work described in this thesis was performed in the ideal MHD limit. However, three non-ideal MHD effects (ambipolar diffusion, Ohmic dissipation, and Hall effect) have long been recognized to play important roles in disk formation. Because of their ability to diffuse the magnetic field at different density regimes, the non-ideal effects could in principle weaken the magnetic braking to various degrees. For example, the role of Ohmic dissipation in core fragmentation has been investigated by Machida et al. (2008), who showed that fragmentation can take place in the central high density regions where the magnetic field strength is greatly reduced by Ohmic dissipation. However, ambipolar diffusion may greatly reduce the field strength and enable fragmentation at a much lower density than that required for Ohmic dissipation. Thus, binary fragments may be produced with a larger initial separation if we include ambipolar diffusion. We believe future studies of binary formation with these non-ideal MHD effects will be important and fruitful.

Finally, to reproduce the observed distributions of binary properties, large scale star cluster formation simulation will be needed, since most stars are thought to form in clusters rather than in isolation (Lada & Lada 2003). Existing numerical studies along this line are rare and mainly account for pure hydrodynamic effects (Bate 2012). However, the magnetic field and outflow feedback are observed to be dynamically important in star cluster forming regions; they deserve a careful investigation. We plan to use high resolution MHD simulations to understand the effects of the magnetic field and outflow feedback on the statistical properties of binary and multiple systems formed in star clusters. This line of research is timely, because more data and better statistics of protostellar systems will soon become available from the new generation of interferometers such as ALMA and JVLA.

Bibliography

Adams, F. C., Ruden, S. P., & Shu, F. H. 1989, ApJ, 347, 959

Allen, A., Li, Z. -Y., & Shu, F. H. 2003, ApJ, 599, 363

Ambartsumian, V. 1937, Astron. Zh., 14, 207

André, P., Ward-Thompson, D., & Barsony, M. 1993, ApJ, 406, 122

Andrews, S. M., & Williams, J. P. 2005, ApJ, 631, 1134

Artymowicz P. 1983, Acta Astron, 33, 223

Basu, S., & Mouschovias, T. C. 1994, ApJ, 432, 720

Bate, M. R. 2000, MNRAS, 314, 33

Bate, M. R., Bonnell, I. A., & Bromm, V. 2002, MNRAS, 336, 705

Bate, M. R. 2009a, MNRAS, 392, 590

Bate, M. R. 2009b, MNRAS, 392, 1363

Bate, M. R. 2012, MNRAS, 419, 3115

Bate, M. R., & Bonnell, I. A. 1997, MNRAS, 285, 33

Batten, A. H. 1973, Binary and Multiple Star Systems, Pergamon Press, Oxford

Berger, M. J., & Colella, P. 1989, J. Comput. Phys., 82, 64

Bergin, E. A., & Tafalla, M. 2007, ARA&A, 45, 339

Boffin, H. M. J., Watkins, S. J., Bhattal, A. S., Francis, N., & Whitworth, A. P. 1998, MNRAS, 300, 1189

Bodenheimer, P. 1995, ARA&A, 33, 199

Bonnell, I. A. 1994, MNRAS, 269, 837

Bonnell, I. A., & Bate, M. R. 1994a, MNRAS, 269, 45

Bonnell, I. A., & Bate, M. R. 1994b, MNRAS, 271, 999

Boss, A. P. 1986, ApJS, 62, 519

Boss, A. P. 1989b, ApJ, 346, 336

Boss, A. P. 2002, ApJ, 568, 743

Boss, A., & Bodenheimer, P. 1979, ApJ, 234, 289

Bryan, G. L., & Norman, M. L. 1997, astro-ph/9710187

Bürzle, F., Clark, P. C., Stasyszyn, F., Greif, T., Dolag, K., Klessen, R. S., & Nielaba, P. 2011, MNRAS, 412, 171

Ciolek, G. E., & Königl, A. 1998, ApJ, 504, 257

Chen, X., Launhardt, R., Bourke, T. L., Henning, T., & Barnes, P. J. 2008, ApJ, 683, 862

Chen, X., Launhardt, R., & Henning, T. 2009, ApJ, 691, 1729

Clarke, C. J. 1992, ASPC, 32, 176

Clarke, C. J. 2012, IAUS, 282, 409

Clarke, C. J., & Pringle, J. E. 1993, MNRAS, 261, 190

Colella, P. & Woodward, P. R. 1984, J. Comput. Phys., 54, 174

Connelley, M. S., Reipurth, B., & Tokunaga, A. T. 2008, AJ, 135, 2526

Connelley, M. S., Reipurth B., & Tokunaga, A. T. 2009. AJ, 138, 1193

Courant, R., Friedrichs, K., & Lewy, H. 1928, IBM Journal of Research and Development, 11, 215

Chen, X., Arce, H. G., & Zhang, Q., et al. 2013, ApJ, 768, 110

Dapp, W. B., & Basu, S. 2010, A&A, 521, 56

Dapp, W. B., & Basu, S. 2011, A&A, 532, 2

Davis, M., Efstathiou, G., Frenk, C. S., & White, S. D. M. 1985, ApJ, 292, 371

Dedner, A., Kemm, F. Kröner, D., Munz, C. -D., Schnitzer, T., & Wesenberg, M. 2002, Journal of Computational Physics, 175, 645

Duchêne, G., Bouvier, J., Bontemps, S., André, P., & Motte, F. 2004, A&A, 427, 651

Duchêne, G., Bontemps, S., Bouvier, J., André, P., Djupvik, A. A., & Ghez, A. M. 2007, A&A, 476, 229

Duchêne, G, & Kraus, A. 2013, ARA&A, 51, 269

Duquennoy, A., & Mayor, M. 1991, A&A, 248, 485

Durisen, R. H., & Tohline, J. E. 1985, prpl.conf, 534

Dyck, H. M., Simon, T., & Zuckerman, B. 1982, ApJ, 255, 103

Enoch, M. L., Corder, S., Dunham, M. M., & Duchêne, G. 2009, ApJ, 707, 103

Enoch, M. L., Corder, S., Duchêne, G., Bock, D. C., Bolatto, A. D., Culverhouse, T. L., Kwon, W., Lamb, J. W., Leitch, E. M., Marrone, D. P., Muchovej, S. J., Pérez, L. M., Scott, S. L., Teuben, P. J., Wright, M. C. H., & Zauderer, B. A. 2011, ApJS, 195, 21

Evans, C. R., & Hawley, J. F. 1988, ApJ, 332, 659

Federrath, C., Banerjee, R., Clark, P. C., & Klessen, R. S. 2010, ApJ, 713, 269

Fischer, D. & Marcy, G. 1992, ApJ, 396, 178

Galli, D., Lizano, S., Shu, F. H., & Allen, A. 2006, ApJ, 647, 374

Galli, D., & Shu, F. H. 1993, ApJ, 417, 243

Ghez, A. M., McCarthy, D. W., Patience, J. L., & Beck, T. L. 1997, ApJ, 481, 378

Girart, J. M., Rao, R., & Marrone, D. P., Science, 313, 812

Godunov, S. K. 1959, Math. Sbornik, 47, 271-306

Goodman, A. A., Benson, P., Fuller, G. A., & Myers, P. C. 1993, ApJ, 406, 528

Goodwin, S. P., Whitworth, A. P., & Ward-Thompson, D. 2004a, A&A, 414, 633

Goodwin, S. P., Whitworth, A. P., & Ward-Thompson, D. 2004b, A&A, 423, 169

Goodwin, S. P., & Kroupa, P. 2005, A&A, 439, 565

Goodwin, S. P., Kroupa, P., Goodman, A., & Burkert, A. 2007, in Protostars and Planets V, ed. B. Reipurth, D. Jewitt, & K. Keil, 133

Hanawa, T., Ochi, Y. & Ando, K. 2010, ApJ, 708, 485

Harten, A., Lax, P. D. & van Leer, B. 1983, SIAM Rev., 25, 35

Heller, C. H. 1991, PhDT, 9

Hennebelle, P.,& Fromang, S. 2008, A&A, 477, 9

Hennebelle, P., & Teyssier, R. 2008, A&A, 477, 25

Herbig, G. H. 1962, Adv. Astron. Astrophys., 1, 47

Hill, J. G., & Day, C. A. 1976, ApJ, 17, 87

Hoyle, F. 1953, ApJ, 118, 513

Hull C. L. H., Plambeck, R. L., Bolatoo, A. D., et al. 2013, ApJ, 768, 159

Janson, M., Hormuth, F., Bergfors, C., Brandner, W., Hippler, S., Daemgen, S., Kudryavtseva, N., Schmalzl, E., Schnupp, C., & Henning, T. 2012, arXiv:1205.4718

Jeans, Sir. J. 1929, Astronomy and Cosmology (Cambridge: Cambridge University Press)

Johns-Krull, C. M. 2009, IAUS, 259, 345

Joos, M., Hennebelle, P., & Ciardi, A., A&A, 543, 128

Jørgensen, J. K., van Dishoeck, E. F., Visser, R., et al. 2009, A&A, 507, 861

Joy, A. H., van Briesbroeck G. 1944, Publ. Astron. Soc. Pac., 56, 123

King, R. R., Goodwin, S. P., Parker, R. J., & Patience. J. 2012a, MNRAS, 427, 2636

Kowal, G., Lazarian, A., Vishniac, E. T., & Otmianowska-Mazur, K. 2009, ApJ, 700, 63

Krasnopolsky, R., Königl, A. 2002, ApJ, 580, 987

Krasnopolsky, R., Li, Z. -Y. & Shang, H. 2011, ApJ, 733, 54

Krasnopolsky, R., Li, Z.-Y., Shang, H. & Zhao, B. 2012, ApJ, 757, 77

Kratter, K. M. 2011, ASPC, 477, 47

Kratter, K. M., Matzner, C. D., Krumholz, M. R., & Klein, R. ApJ, 708, 1585

Kraus, A. L., & Hillenbrand, L. A. 2012, ApJ, 757, 141

Kraus, A. L., Ireland, M. J., Martinache, F., & Hillenbrand, L. A. 2011, ApJ, 731, 8

Kraus, A. L., Ireland, M. J., Hillenbrand, L. A., & Martinache, F. 2012, ApJ, 745, 9

Krumholz, M. R., McKee, C. F., & Klein, R. I. 2004, ApJ, 611, 399

Krumholz, M. R., Matzner, C. D., McKee, C. F. 2006, ApJ, 653, 361

Krumholz, M. R., Klein, R. I., McKee, C. F., Offner, S. S. R., & Cunningham, A. J. 2009, Science, 323, 754

Krumholz, M. R., Crutcher, R. M., & Hull, C. L. H. 2013, ApJ, 767, 11

Kuiper, G. P. 1935a, Publ. Astron. Soc. Pac., 47, 15

Kunz, M. W., & Mouschovias, T. C. 2010, MNRAS, 408, 322

Kurganov, A. & Tadmor, E. 2000, J. Comp. Phys., 160, 214

Lada, C. J., & Lada, E. A. 2003, ARA&A, 41, 57

Larson, R. B. 1969, MNRAS, 145, 271

Larson, R. B. 1981, MNRAS, 194, 809

LeVeque, R. J. 2002, Finite Volume Methods for Hyperbolic Problems (Cambridge University Press)

Li, Z. -Y., & Krasnopolsky, R., & Shang, H. 2011, ApJ, 738, 180

Li, Z.-Y., Krasnopolsky, R., Shang, H. 2013, ApJ, 774, 82

Li, Z. -Y., & McKee, C. F. 1996, ApJ, 464, 373

Lizano, S., & Shu, F. H. 1989, ApJ, 342, 834

Looney, Leslie W., Mundy, L. G., & Welch, W. J. 2000, ApJ, 529, 477

Lyttleton, R. 1953, The Stability of Rotating Liquid Masses (Cambridge: Cambridge University Press)

Mason, B. D., Henry, T. J., Hartkopf, W. I., ten Brummelaar, T., & Soderblom, D. R. 1998, AJ, 116, 2975

Machida, M. N., Tomisaka, K., Matsumoto, T., & Inutsuka, S. 2008, ApJ, 677, 327

Machida, M. N., Inutsuka, S., & Matsumoto, T. 2010, ApJ, 724, 1006

Mathieu, R. D. 1994, ARA&A, 32, 465

Mathieu, R. D., Ghez, A. M., Jensen, E. L. N., & Simon, M. 2000, prpl.conf, 703

Matsumoto, T., & Tomisaka, K. 2004, ApJ, 616, 266

Maury, A. J., André, P., Hennebelle, P., Motte, F., Stamatellos, D., Bate, M., Belloche, A., Duchêne, G., & Whitworth, A. 2010, A&A, 512, 40

Mellon, R. R., & Li, Z. -Y. 2008, ApJ, 681, 1356

Mellon, R. R., & Li, Z. -Y. 2009, ApJ, 698, 922

Miyama, S. M., Hayashi, C., & Narita, S. 1984, ApJ, 279, 621

Mouschovias, T. C. 1991, in NATO ASIC Proc. 342: The Physics of Star Formation and Early Stellar Evolution, ed. C. J. Lada & N. D. Kylafis, 61

Mouschovias, T. C. & Paleologou, E. V. 1979, ApJ, 230, 204

Myers, A. T., McKee, C. F., Cunningham, A. J., Klein, R. I., & Krumholz, M. R. 2012, arXiv:1211.3467

Nakano, T. 1984, Fundamentals of Cosmic Physics, vol. 9, 139

Nakano, T., Nishi, R., & Umebayashi, T. 2002, ApJ, 573, 199

Nakamura, F., & Li, Z. -Y. 2005, ApJ, 631, 411

Nakano, T., & Nakamura, T. 1978, PASJ, 30, 671

Offner, S. S. R., Klein, R. I., McKee, C. F., & Krumholz, M. R. 2009, ApJ, 703, 131

Offner, S. S. R., Kratter, K. M., Matzner, C. D., Krumholz, M. R. & Klein, R. I. 2010, ApJ, 725, 1485

Öpik, E. 1924, Publ. Obs. Astron. Univ. Tartu, 25, 6

O'Shea, B. W., Bryan, G., Bordner, J., Norman, M. L., Abel, T., Harkness, R., & Kritsuk, A. 2004, astro-ph/0403044

Ostriker, E. C. 1994, ApJ, 424, 292O

Ostriker, J. P., & Bodenheimer, P. 1973, ApJ, 180, 171

Padoan, P., & Nordlund, Å. 2011, ApJ, 730, 40

Portegies Zwart, S. F., Hut, P., McMillan, S. L. W., & Verbunt, F. 1997, A&A, 328, 143

Press, W. H., & Teukolsky, S. A. 1977, ApJ, 213, 183

Price, D. J., & Bate, M. R. 2007, MNRAS, 377, 77

Raghavan, D., McAlister, H. A., Henry, T. J., Latham, D. W., Marcy, G. W., Mason, B. D., Gies, D. R., White, R. J., & ten Brummelaar, T. A. 2010, ApJS, 190, 1

Reipurth, B., & Zinnecker, H. 1993, A&A, 278, 81

Roe, P. 1981, J. Comput. Phys., 43, 357

Ruffert, M. 1994, ApJ, 427, 324

Santos-Lima, R., de Gouveia Dal Pino, E. M., & Lazarian, A. 2012, ApJ, 747, 21

Seifried, D., Banerjee, R., Klessen, R. S., Duffin, D., & Pudritz, R. E. 2011, MNRAS, 417, 1054

Seifried, D., Banerjee, R., Pudritz, R. E., & Klessen, R. S. 2012, MNRAS, 423, 40

Shatsky, N., & Tokovinin, A. 2002, A&A, 382, 92

Shen, S., Wadsley, J., Hayfield, T., & Ellens, N. 2010, MNRAS, 401, 727

Shu, F. H. 1977, ApJ, 214, 488

Stepinski, T. F., & Black, D. C. 2001, A&A, 371, 250

Takakuwa, S., Saito, M., Lim, J., et al. 2012, ApJ, 754, 52

Tassis, K. & Mouschovias T. Ch. 2007, ApJ, 660, 388

Thies, I., Kroupa, P., Goodwin, S. P., Stamatellos, D., & Whitworth, A. P. 2010, ApJ, 717, 577

Tobin, J. J., Hartmann, L., Looney, L. W., & Chiang, H.-F. 2010, ApJ, 712, 1010

Tobin, J. J., Hartmann, L., Chiang, H.-F., et al. 2012, Nature, 492, 83

Tobin, J. J., Chandler, C. J., Wilner, D. J., Looney, L. W., Loinard, L., Chiang, H.-F., Hartmann, L., Calvet, N., D'Alessio, P., Bourke, T. L., & Kwon, W. 2013, ApJ, 779, 93

Tohline, J. E. 1982, Fund. of Cos. Phys., 8, 1

Tohline, J. E. 2002, ARA&A, 40, 349

Tokovinin A. A., & Smekhov, M. G. 2002, A&A, 382, 118

Tomisaka, K. 1998, ApJ, 502. 163

Toro, E.F. 1999, Riemann Solvers and Numerical Methods for Fluid Dynamics, Springer-Verlag, 2nd Edition

Troland, T. H., & Crutcher, R. M. 2008, ApJ, 680, 457

Truelove, J. K., Klein, R. I., McKee, C. F., Holliman, J. H. II, Howell, L. H., & Greenough, J. A. 1997, ApJ, 489, 179

Truelove, J. K., Klein, R. I., McKee, C. F., Holliman, J. H. II, Howell, L. H., Greenough, J. A., & Woods, D. T. 1998, ApJ, 495, 821

Tsuribe, T., & Inutsuka, S.-i. 1999, ApJ, 523, 155

Van Leer, B. 1979, J. Comput. Phys., 32, 101

Watkins, S. J., Bhattal, A. S., Boffin, H. M. J., Francis, N., & Whitworth, A. P. 1998b, MNRAS, 300, 1205

Watkins, S. J., Bhattal, A. S., Boffin, H. M. J., Francis, N., & Whitworth, A. P. 1998c, MNRAS, 300, 1214

Williams, H. A., & Tohline, J. E. 1988, ApJ, 334, 449

Wang, P., & Abel, T. 2009, ApJ, 696, 96

Wang, P., Li, Z. -Y., Abel, T., & Nakamura, F. 2010, ApJ, 709, 27

Ward-Thompson, D., Kirk, J. M., Crutcher, R. M., Greaves, J. S., Holland, W. S., & Andr, P. 2000, ApJ, 537, 135

Williams, J. P., & Cieza, L. A. 2011, ARAA, 49, 67

Zhao, B., Li, Z. -Y., Nakamura, F., Krasnopolsky, R., & Shang, H. 2011, ApJ, 742, 10

Zhao, B., Li, Z. -Y. 2013, ApJ, 763, 7

Zhao, B., Li, Z. -Y. & Kratter, K. M. 2013, arXiv:1308.0830

Zinnecker, H. 1984, Astrophys. Space Sci., 99, 41